POLARIZED XENON FOR MEDICAL APPLICATIONS

A Doctoral Dissertation
by

Anna Wojna-Pelczar

Academic Advisor

Prof. dr hab. Tomasz Dohnalik

Secondary Academic Advisor

Dr Tadeusz Pałasz

M. Smoluchowski Institute of Physics
Faculty of Physics, Astronomy
and Applied Computer Science
Jagiellonian University

Kraków 2015

Acknowledgements

I owe a debt of gratitude to all those people, who have made this dissertation possible and because of whom my graduate experience has been one that I will keep forever.

I would like to express my acknowledgement for doctoral supervisor, Prof. Tomasz Dohnalik, who gave me the possibility to be introduced to the hyperpolarized noble gas physics, and as an advisor he gave me the freedom to explore on my own and, at the same time, guided me to recover when my steps faltered.

I am deeply grateful for having a possibility to work with my co-supervisor Dr Tadeusz Pałasz, to whom I owe my recognition for working in really pleasant environment and who is responsible for broadening my interests in lasers and optics, showing me the most creative ways to build something from nothing. I will also carry memories of countless inspiring discussions on all interdisciplinary matters.

I am also thankful to Dr Zbigniew Olejniczak for his time in both insightful comments and constructive criticism at different stages of my research. I am deeply grateful for correcting my writing and for carefully reading and commenting on countless revisions of the PhD thesis.

This work could not be done without the help of electronics engineers from Atomic Optics Department: Stanisław Pajka, Janusz Kuźma and the former member Józef Flaga. The technical support was provided by the Mechanical Workshop where I must thank Eng. Andrzej Biesiada and Eng. Michał Jabłoński for their help and guidance and the Mechanical Workshop employees for their work always on time. I want to thank the former members Piotr Klocek and Jerzy Olejniczak for their support in the early stages of my work. I would also like to thank Jan Pieprzyk for his professionalism, precision and knowledge on glass work and providing me with precise glass instalments even at the last-minute order - this work would not be possible without him.

I owe a great support from Dr Guilhem Collier and Dr Anna Nikiel-Osluchowska who were the first supervisors of my daily work in laboratory just when I joined the group. I also want to thank Dr Mateusz Suchanek for help on helium experiments and his kindness.

I would like to acknowledge Danuta Myrek who provided me with her daily support in all kinds of ways, from handing my administrative problems in the most impossible and quickest ways to being just a good listener and friend.

My gratefulness is also directed to Dr Grzegorz Zuzel for providing me with electronic and vacuum equipment during my experiment.

Finally, I appreciate the financial support from National Laboratory of Quantum Technologies (POIG.02.02.00-00-003/08) and Faculty of Physics (DCS/000686/2012 and DCS2014).

This work would not be possible without support of my family, who helped me during ups and downs. Especially, I would like to thank my husband Krzysztof who believed in me and supported my decisions.

Abstract

The hyperpolarized noble gases (xenon ^{129}Xe and helium ^{3}He) delivered a great tool for the growing number of applications, spanning nuclear physics, Medical Resonance Imaging (MRI) and Nuclear Magnetic Resonance (NMR) spectroscopy studies. Hyperpolarization may be achieved via the Spin Exchange Optical Pumping (SEOP, for ^{129}Xe or ^{3}He) or the Metastability Exchange Optical Pumping (MEOP, ^{3}He).

The main aim of this thesis is to present the design of a novel large scale SEOP polarizer, built in the frame of the PhD thesis, for producing hyperpolarized ^{129}Xe for further medical imaging of lungs. Increasing requirements for large volumes of hyperpolarized gases could be realized by efficient polarizers, such as the novel polarizer presented here.

The thesis characterizes the optimum operating parameters of the polarizer. The polarizer works basing on the SEOP method, resulting in a high-yield of the polarized gas. The main parts of the unit are presented: the coil system producing magnetic field, the gas (^{129}Xe and buffer gases: N_2, ^{4}He) and rubidium distribution system, the high-power laser diode system spectrally narrowed with Volume Bragg Gratings for rubidium optical pumpin and the high-volume SEOP cell. The SEOP polarizer was designed to work at the pressure close to the atmospheric pressure with a low content of the ^{129}Xe gas in the SEOP mixture, contained in a large SEOP cell (about 6 L inner volume). This is unique comparing to majority of other SEOP designs, which use the high-pressure and small-volume cells. The motivation, a brief overview of the state of the art in the hyper-polarized gases techniques, the current status of the SEOP polarizer project and the future research plans are also part of this work.

Contents

List of Figures

List of Tables

1

Introduction

1.1 Motivation

> *"Science begins with counting. To understand a phenomenon, a scientist must first describe it; to describe it objectively, he must first measure it. If cancer medicine was to be transformed into a rigorous science, then cancer would need to be counted somehow – measured in some reliable, reproducible way."*
>
> – *The Emperor of All Maladies: A Biography of Cancer*
> by Siddhartha Mukherjee

> *"Scientist in his laboratory is not a mere technician: he is also a child confronting natural phenomena that impress him as though they were fairy tales."*
>
> – Marie Skłodowska-Curie, *A Biography* by Eve Curie Labouisse

Pulmonary diseases are, after the heart diseases and stroke, the most frequent causes of death. It is also known that the lung cancer is more common death cause in women than the breast cancer. Pulmonary diseases such as chronic obstructive pulmonary disease (COPD), asthma, cystic fibrosis, emphysema, and cancer are the leading causes of morbidity and mortality globally and are characterized by a progressive and irreversible airflow limitation.

The severity of any airflow disease changes in a wide range and it is still an open question how to determine its degree. The most common methods that are used in the diagnosis of pulmonary diseases are rather nonspecific [1]. The multi detect computer tomography (MDCT), positron emission n tomography (PET), and single photon emission computed tomography (SPECT) direct imaging methods provide some information, but they cannot image regional ventilation or perfusion, have limits of resolution, and expose the patient to ionizing radiation [1].

For instance, we distinguish two main effects in COPD, obstructive bronchiolitis, meaning anomalous inflammatory responses in the small airways, and emphysema, which is a parenchymal destruction. Potential COPD clinical trials have been carried out to develop an effective therapy, but they are usually based on spirometry, a method which cannot be a main diagnostic tool due to its limited scope. Quantitative metrics must be implemented

to better classify COPD phenotypes, as well as quantify illness progression and evaluate therapeutic responses. This is the case for other lung diseases as well. Moreover, the need for the continuous treatment evaluation calls for the development of a non-invasive diagnostic procedure [2].For example, cystic fibrosis and cancer require constant monitoring of the treatment progress.

The hyperpolarized (HP) ^{3}He and ^{129}Xe noble gases have become a great tool in a growing number of non-medical applications such as neutron filters [3] or nuclear magnetic resonance (NMR) spectroscopy studies of porous materials [4]. This fundamental breakthrough would not possible without A. Kastlers work on *optical pumping*, which earned him the Nobel Prize [5]. A. Kastler showed that by illuminating alkali vapors with circularly polarized light one can obtain non-thermal equilibrium populations in the spin angular momentum sublevels. His theory was tested shortly afterwards by J. Brossel et al. on sodium nuclei [6]. A comprehensive introduction to optical pumping was presented in a well-known paper by W. Happer [7].

Hyperpolarized ^{3}He or ^{129}Xe are produced by the *the spin exchange optical pumping* (SEOP) method. The angular momentum from the resonant, circularly-polarized light is transferred to the electronic spins of an alkali-metal, and is subsequently transferred to the helium or xenon nuclei by the gas-phase collisions.

Hyperpolarization of ^{3}He can be also obtained with another method, *the metastability exchange optical pumping* (MEOP)[1]. First, using the radiofrequency discharge, a long-lived energy level, *the metastability state*,is populated. Next, the optical pumping is performed with circularly-polarized laser light to produce polarization of metastable atoms. Finally, the metastability is transferred to helium nuclei via collisions with un-polarized helium atoms at the ground energy level.

An important breakthrough was the application of HP noble gases as unique contrast agents in the magnetic resonance imaging (MRI) of human lungs. Without exposing the patient to ionizing radiation, MRI provides three-dimensional images characterized by good spatial resolution and high signal-to-noise ratio (SNR). However, due to low water concentration in the lungs, the use of hyperpolarized contrast agent is necessary. Several mapping techniques (T_1, T_2, diffusion imaging etc.) give an opportunity to diagnose the regional heterogeneity of the lungs, evaluate ventilation and perfusion. Videos illustrating the dynamics of the gas propagation along the airways can be also obtained. In presented doctoral thesis the focus is on ^{129}Xe. The specific properties of xenon, mostly arising from the large polarisability of its electron cloud, make this noble gas not only a good contrast agent in the MRI medical diagnosis, but also a sensitive NMR probe for biological systems [8]. For instance, xenon interacts with liquids, protein solutions and biological membranes, giving information about their internal structure.

The lung imaging was always a challenge, and this new method of obtaining not only morphology, but also information about lung functionality is very promising. The difference in the NMR spectrum of about 200 ppm between gaseous and dissolved ^{129}Xe inside the lungs [9, 10] gives quantitative information about variations in the lung structure and ventilation that are caused by a spreading disease [11]. The information about the diffusion in alveolar spaces and perfusion dynamics, which is not available with any other methods, can be also obtained. Therefore this diagnostic method becomes the most novel technique in pulmonary studies, along with its safety, non-invasiveness, and the usefulness for a number of lung diseases. So far, after some promising results in the animal models studies [12, 13], the

[1] A detailed description of the metastability exchange optical pumping (MEOP) method for obtaining hyperpolarized ^{3}He is presented in the *Appendix B*.

method was proposed to diagnose the following diseases: COPD, cystic fibrosis, and cancer in the pre-clinical trials [14, 15, 16].

A wide spectrum of possible MRI and NMR studies using HP ^{129}Xe as a contrast agent calls for the steady source of polarized gas. Rising requirements for large volumes of HP gas could be met only by the development of SEOP polarizers. A novel, large volume and normal pressure oriented, SEOP polarizer was built, tested and optimized in order to supply HP ^{129}Xe gas for all kinds of experiments. It will be characterized in this Thesis.

1.2 Thesis summary

In the chapters that follow, I describe the theory of hyperpolarization of ^{129}Xe and the implementation of ^{129}Xe polarizer. This experimental work I have undertaken during my PhD studies.

In particular, *Chapter 2* presents the basics of nuclear polarization definition, its non-equilibrium value that is achieved by the SEOP method and principles of mechanisms present during this process - polarization build-up and relaxation.

In *Chapter 4* I describe the assembly of the ^{129}Xe SEOP polarizer that was designed and built. The main components of the polarizer are presented: a set of coils generating a homogenous magnetic field, the laser system and optics, the SEOP cell, and the gas distribution unit. The polarizer was built from scratch and the majority of parts were first modeled and then home-built with the help of the mechanical workshop.

Chapter 5 shows the results of the ^{129}Xe SEOP. The step by step experimental procedure was described in detail. The initial NMR signal from the polarized gas was measured and calibrated.

The discussion of the polarizer construction and obtained results is presented in *Chapter 6*. A careful analysis of pros and cons of undertaken steps is made. The thesis concludes with *Chapter 7*, which gives the perspectives of the polarizer role in future applications in medicine and material science that are planned.

During this time several modifications were introduced to the initial design , the major being the upgrade of the laser system that allowed for a better polarizer performance. The old laser system, which was used to perform first tests with measuring the signal from the HP ^{129}Xe is described in the *Appendix A.* .

During my PhD I contributed to the implementation of two ^{3}He MEOP polarizers, took part in the experimental work concerning the metastability exchange optical pumping technique, and in the application of HP ^{3}He in medical imaging. This was my introduction to the noble gases polarization techniques, and it is summarized in the *Appendix B.* . The first human lung scan obtained with this unique technique in Poland is presented.

2

Theory

2.1 Optical pumping and hyperpolarization

Let us consider a population of N_{total} of nuclei with spin one-half ($I = 1/2$) placed in a static magnetic field B_0. In thermal equilibrium, the populations $N_\downarrow$ and $N_\uparrow$ of two magnetic sublevels corresponding to the magnetic quantum number $m = \pm 1/2$ are described by the Boltzmann law:

$$\frac{N_\downarrow}{N_\uparrow} = exp\left(-\frac{\gamma\hbar B_0}{k_B T}\right), \tag{2.1}$$

where γ is the gyromagnetic ratio, $\hbar$ the Planck constant, k_B the Boltzmann constant and T is the temperature. The $N_\uparrow$ ($N_\downarrow$) refer to spins aligned along (opposite to) the direction of the main magnetic field B_0.

In a classical picture, the magnetic moment precesses about the direction of $\vec{B_0}$ with the angular frequency ω_0:

$$\omega_0 = -\gamma B_0, \tag{2.2}$$

where ω_0 is known as the Larmour frequency. In the quantum mechanical picture, the Zeeman interaction of nuclear spins with magnetic field causes the hyperfine splitting of energy levels. The difference in energy between the two sublevels in the presence of magnetic field is equal to:

$$\Delta E = E_\downarrow - E_\uparrow = -\gamma\hbar B_0 = \hbar\omega_0 \tag{2.3}$$

The polarization P of the system is defined as:

$$P = \frac{N_\uparrow - N_\downarrow}{N_{total}} \tag{2.4}$$

The bulk magnetization M_0, which is defined as the polarization per unit volume, will be proportional to P and the density of nuclear spins. In thermal equilibrium, in the external magnetic field B_0 and at temperature T we have:

$$P = tanh\left(\frac{\gamma\hbar B_0}{2kT}\right). \tag{2.5}$$

In typical experimental conditions $\gamma\hbar B_0/kT \ll 1$, so we get:

$$P \approx \frac{\gamma\hbar B_0}{2kT} \tag{2.6}$$

For medical MRI scanners operating at 1.5 T magnetic field and room temperature, the polarization is of the order of $10^{-5} - 10^{-6}$. In the proton MRI experiments, a high density of protons in the human body compensates low polarization. The exception are the lungs, in which the density of protons in the form of water vapor is three orders of magnitude lower. Therefore the MRI imaging of human lungs becomes only feasible with the use of noble gases such as ^{3}He or ^{129}Xe, because their polarization can be greatly enhanced via *optical pumping* [7, 17].

In optical pumping, basically an angular momentum is transferred from the laser photons to electronic and then to nuclear spins, thereby increasing the nuclear spin polarization in the system (see Fig. 2.1). The non-equilibrium polarization can be about five orders of magnitude higher than the thermal equilibrium polarization and that is the reason for calling this phenomenon a *hyperpolarization*. The model of optical pumping will be presented in the next chapter on Figure 3.3. For a given circular polarization of the laser light, $\sigma+$ or $\sigma-$, the selection rules define which sublevels are populated.

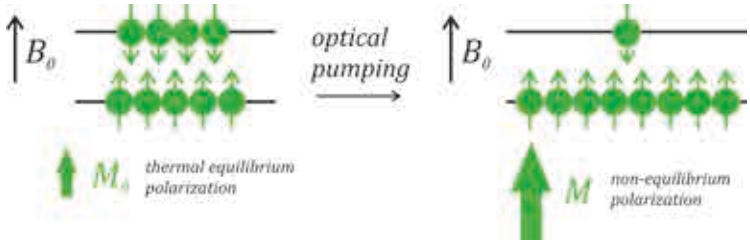

Figure 2.1: Schematic difference between thermal equilibrium and non-equilibrium polarization before and after optical pumping in gases.

It has been already mentioned that there are two methods for transferring the angular momentum to the nucleus – metastability exchange optical pumping and spin exchange optical pumping. The first is used for polarizing ^{3}He atoms, while SEOP is used for both ^{3}He or ^{129}Xe. A careful handling of the experimental setup is required to obtain and maintain the hyperpolarized ^{129}Xe or ^{3}He gas for long periods of time. Details of the MEOP method, ^{3}He polarizers, and their implementation in medical studies are presented in *Appendix B*. The SEOP method is the main subject of this thesis.

2.2 Atomic collisions

A proper operation of the SEOP technique requires the optical pumping cell to contain various gases. The interactions between the gaseous atoms, especially these that posses nuclear spins, can lead to spin exchange or spin destruction. Two types of interactions can be distinguished, depending on the interaction time: the sudden binary collisions, and the formation of long-lived van der Waals molecules (Fig. 2.2.). The former is typical for all atomiccollisions occurring in the SEOP and takes place at high pressure regime. The latter characterizes the alkali-metal-atom-^{129}Xe interactions and appears at low pressure. Here, we focus on Rb-^{129}Xe collisions:

Binary collisions are dominant in the high pressure regime. Symbolically, for Rb-^{129}Xe we can write:

$$Rb(\uparrow) + Xe \rightarrow Rb + Xe(\uparrow). \tag{2.7}$$

Binary collisions are characterized by two cross-sections: one describing the Rb-Xe spin-rotation σ_{SR} and the second describing the Rb-Xe spin-exchange σ_{SE}. Binary collisions have a short interaction time od 10^{-12} s. In the case of the SEOP experiments with the Rb-Xe mixture, the spin-exchange due to binary collision is less efficient than the spin-rotation, as the spin-exchange and spin-destruction rates are: $\kappa_{SE}^{Rb-Xe} = 2.10 \times 10^{-16}$ cm$^{-1}s^{-1}$ [18, 19] and $\kappa_{SD}^{Rb-Xe} = 9.07 \times 10^{-16}$ cm$^{-1}s^{-1}$ [20], respectively. So the difference must be caused by the spin-rotation interaction. Typical values of spin-exchange and destruction rates due to binary collisions were given in [18]. Binary collisions between two Rb atoms lead to the spin-temperature distributionamong Rb.

Van der Waals (vdW) molecule complex is formed during 3-body collisions as is shown here:

$$Rb + Xe + Y \rightarrow RbXe + Y. \tag{2.8}$$

In the SEOP experiment the Rb and ^{129}Xe atoms require a third body Y, needed for energy conservation, which often includes the heaviest atoms or molecules in the mixture, N_2 or ^{129}Xe. The interaction time during collision is rather long, of the order of 10^{-7} – 10^{-9} s. The van der Waals molecule formation happens rather at low pressure and this is the main reason why the presented polarizer operates in such conditions. The Fermi contact interaction time is longer by three orders of magnitude, which causes remarkably more effective polarization transfer than during the fast two-body binary collisions. . Nevertheless, the spin-destruction and spin-exchange rates are more significant. The vdW molecule formation leads to the asymmetry of the Rb absorption line and the appearance of satellite absorption lines.

Nelson showed that the Rb spin loss rate is nearly entirely due to the binary Rb-^{129}Xe type of collisions, whereas the spin-exchange rate is dominated by the spin-exchange that occurs during the lifetime of the Rb-^{129}Xe van der Waals molecules [20].

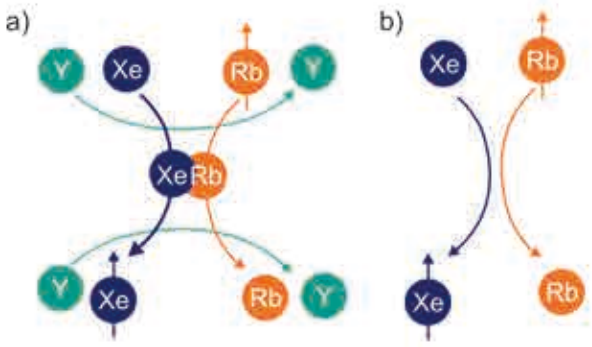

Figure 2.2: Schematic representation of a) three-body van der Waals molecule formation and b) two-body binary collisions between ^{129}Xe and Rb. Y is the third body: N_2, ^{129}Xe or rarely ^{4}He.

2.3 The formation of the van der Waals molecule

The first work by Bouchiat et al. [21] confirmed experimentally the key role of creating van der Waals molecules by Rb and heavy noble gases. The spin transfer occurs mostly via the vdW molecule creation. Therefore the SEOP process applied to heavy noble gases becomes more complex and the simple spin-exchange cross section model is insufficient.

The process hasthree main steps: the formation of the molecule in a three-body collision, the evolution of the spins during the lifetime of the molecule, and the collisional break-up (in which a buffer gas or another ^{129}Xe atom is involved), as is schematically depicted on Figure 2.2. The vdW molecule is weakly bound and nearly every collision separates them into atoms again.

According to [22], the Hamiltonian of such interaction can be defined as follows:

$$H = A\mathbf{I}\cdot\mathbf{S} + \chi\mathbf{N}\cdot\mathbf{S} + \alpha\mathbf{K}\cdot\mathbf{S} + g_S\mu_B\mathbf{B}\cdot\mathbf{S} + g_K\mu_B\mathbf{B}\cdot\mathbf{K} + ... \tag{2.9}$$

The first term describes the the magnetic dipolar interaction between nuclear spin $\mathbf{I}$ and electronic spin $\mathbf{S}$ of alkali-metal. The fourth and fifth terms s represent the interaction of electronic and nuclear spin of alkali-metal atom with the magnetic field $\mathbf{B}$, respectively.

Collision with van der Waals molecule creation is described with *the spin-rotation (SR) interaction* $\chi\mathbf{N}\cdot\mathbf{S}$, where $\mathbf{N}$ is the angular momentum of the pair of atoms about their center of mass. This process causes only Rb relaxation without any infuence on the ^{129}Xe nuclear polarization.

The hyperfine interaction $\alpha\mathbf{K}\cdot\mathbf{S}$ between the nuclear spin $\mathbf{K}$ of the noble-gas atom and the electron spin of the alkali-metal atom $\mathbf{S}$ is responsible for transferring some fraction of the alkali electron spin polarization to nuclear spins. This interaction is responsible for the spin-exchange that occurs both within the van der Waals molecules, and during binary collisions.

The A, α, and χ are the coupling coefficients. They all depend on the internuclear separation R between the alkali-metal atom and the ^{129}Xe atom ($A = A(R)$, $\chi = \chi(R)$, $\alpha = \alpha(R)$) [24].

The spin-rotation interaction originates from the electron spin movement in the presence of the magnetic field that is generated by the noble-gas or alkali-metal nuclear core. For heavy atoms like ^{129}Xe, the contribution from the magnetic field generated by the noble-gas core is dominant.

2.4 Theory of SEOP

Bouchiat et al. [23] showed that it is possible to transfer angular momentum to a nucleus (then it was ^{3}He) by spin-exchange, although it was a very slow process.

An extensive theoretical and experimental work on the spin-exchange and spin-relaxation processes in alkali and noble gas systems was mainly carried out the by Princeton group. ^{129}Xe is a heavy atom with large electron cloud. When using ^{129}Xe, additional effects occur in comparison to a small and non-reactive ^{3}He. The basics of ^{129}Xe SEOP was fully described in a series of papersby Happer and co-workers [7, 24] and Wagshul and Chupp [25].

Spin-exchange optical pumping is a two stage process consisting of optical pumping of valence electrons in the alkali-metal vapor and spin transfer to the nuclei. An increased efficiency of the optical pumping process is achieved when buffer gases N_2 and He (isotope ^{4}He) are added to the cell. In this thesis the SEOP of ^{129}Xe is described and rubidium is chosen as the alkali-metal. Therefore, all the symbols that were used in the theoretical considerations for ^{129}Xe and Rbare relevant. Nevertheless, a short discussion about choosing alternative nuclei and alkali-metal atoms are also presented in the following subsections.

Each step of SEOP can be considered separately.

The first process is the optical pumping of alkali-metal atoms by irradiation with circularly polarized light that is tuned tuned to proper transition (the scheme is presented in Section 3.1). It depends on the alkali-metal vapor density which can be controlled by its temperature. Furthermore, a well-established light source (e. g. tuning and providing a full illumination of the laser light in the SEOP cell as described in detail in *Chapter 3*) is a key for a high photon efficiency, which is the main factor in obtaining a high alkali-metal polarization. First the rubidium polarization as a function of position z in the optical cell along the laser propagation direction is calculated:

$$P_{Rb}(z) = \frac{\gamma_{op}(z)}{\gamma_{op}(z) + \Gamma_{SD}}, \tag{2.10}$$

where Γ_{SD} is the spin-destruction rate of alkali-metal polarization and $\gamma_{op}(z)$ is the optical pumping rate, which depends on the alkali-metal absorption cross section $\sigma(\nu)$ and the frequency- and position-dependent laser intensity profile within the cell $\Phi(\nu, z)$ according to:

$$\gamma_{op} = \int \Phi(\nu, z)\sigma(\nu)d\nu \tag{2.11}$$

and

$$\frac{d\Phi(\nu, z)}{dz} = -[Rb] \cdot \Phi(\nu, z)\sigma(\nu) \cdot (1 - P_{Rb}(z)). \tag{2.12}$$

Photons are removed from the propagating light at each step δz, along the optical cell, and $[Rb]$ is the rubidium density.

The spin-destruction rate is attributed to binary collisions with atoms in the SEOP mixture (Eq. 2.13), or the formation and breakup of short-lived Rb-^{129}Xe van der Waals (vdW) molecules (Eq. 2.14):

$$\Gamma_{SD}^{BC} = \sum_i [G_i]\kappa_{SD}^{Rb-i} \tag{2.13}$$

$$\Gamma_{SD}^{vdW} = \left(\frac{66183}{1 + 0.92\frac{[N_2]}{[Xe]} + 0.31\frac{[He]}{[Xe]}}\right)\left(\frac{T}{423}\right)^{-2.5} \tag{2.14}$$

κ^{Rb-i} is the Rb spin-destruction cross section coefficient for Rb binary collisions with each gas atom present in the optical cell and $[G_i]$ is an atomic density of a given gas atom (expressed in cm^{-3}). The numerical values of the coefficients are reported in the Table 2.1. The second expression (Eq.2.14) was discussed in [26] and applies to systems where large quantities of buffer gases are used. While the κ_{SD}^{Rb-i} coefficients are pressure and field independent, the spin-destruction component due to van der Waals collisions depends on the gas ratio in the SEOP mixture. The above destruction rates contribute to the total spin-destruction rate: $\Gamma_{SD} = \Gamma_{SD}^{BC} + \Gamma_{SD}^{vdW}$.

The Rb spin-destruction rate coefficient type	$[cm^3 s^{-1}]$	Reference.
κ_{SD}^{Rb-Rb}	4.2×10^{-13}	[27]
κ_{SD}^{Rb-He}	$1.0 \times \mathrm{T}^{4.26} \times 10^{-29}$	[27]
$\kappa_{SD}^{Rb-N_2}$	$1.3 \times \mathrm{T}^{3} \times 10^{-25}$	[28]
κ_{SD}^{Rb-Xe}	$6.3 \times (T - 273.15)^{1.17} \times 10^{-17}$	[29]

Table 2.1: The Rb spin-destruction rate coefficients for binary collisions. T is the absolute temperature.

The second step in the SEOP process is the transfer of spin polarization from the alkali-metal electrons to the ^{129}Xe nuclei via Rb-^{129}Xe hyperfine interaction (the third term in the Hamiltonian given in Equation 2.9). The spin-exchange time in ^{129}Xe is of the order of tens of seconds and the xenon is able to form long-lived molecules with the alkali-metal.

The nuclear polarization is then given by:

$$P_{Xe}(t) = \langle P_{Rb} \rangle \frac{\gamma_{SE}}{\gamma_{SE} + \Gamma}(1 - e^{-(\gamma_{SE}+\Gamma)t}), \tag{2.15}$$

where $\langle Rb \rangle$ is time- and volume- averaged rubidium polarization, γ_{SE} is the spin-exchange rate and Γ is the spin-destruction rate of the ^{129}Xe nuclear polarization. The latter is dominated by a wall relaxation, but can be also caused by magnetic field gradients [30], oscillating magnetic field noise [31], and collisions with other atoms that are present in the SEOP mixture including ^{129}Xe atoms [32] (see Section 2.6).

The spin-exchange occursin two processes: binary collisions and Rb-^{129}Xe van der Waals molecules creation [33]:

$$\gamma_{SE} = \gamma_{SE}^{BC} + \gamma_{SE}^{vdW}, \tag{2.16}$$

$$\gamma_{SE}^{BC} = \kappa_{SE}^{BC}[Rb] = \kappa_{SE}^{Rb-Xe}[Rb], \tag{2.17}$$

$$\gamma_{SE}^{vdW} = \kappa_{SE}^{vdW}[Rb] = \sum_i \frac{1}{\frac{[G_1]}{\psi_i}}[Rb], \tag{2.18}$$

where κ_{SE}^{BC} is the Rb-^{129}Xe spin-exchange rate coefficient during binary collisions, κ_{SE}^{vdW} the Rb-^{129}Xe spin-exchange rate coefficient for the van der Waals molecule, and [Rb] is the rubidium density. The spin-exchange rate coefficient for Rb-^{129}Xe value reported by [19] equals:

$$\kappa_{SE}^{Rb-Xe} = 2.17 \times 10^{-16} cm^3 s^{-1}. \tag{2.19}$$

The parameter ψ_i is a vdW-specific rate and scales for each gas ratio for a given gas density $[G_i]$: xenon, helium or nitrogen [34].

It should be noted that the spin destruction for ^{129}Xe is enormously high due to its large electronic cloud. In the presence of spinless buffer gases, the electronic spin relaxation rate can be long, but the collisions of ^{129}Xe atoms, carrying a nuclear spin, with Rb atoms shorten the relaxation time significantly. This process is mediated by the cross relaxation due to fluctuating magnetic field generated by ^{129}Xe nucleus and scales with the ^{129}Xe atom density N_{Xe} and the velocity-averaged spin exchange cross section $\langle\sigma\nu\rangle$. This means that due to the large value of the κ_{SD} parameter of xenon of about 5200×10^{-18} cm^3s^{-1} [21], ^{129}Xe

The Rb spin-exchange rate coefficient type	$[cm^3s^{-1}]$	Reference.
κ_{SE}^{Rb-Rb}	4.2×10^{-13}	[27]
κ_{SE}^{Rb-Xe}	2.7×10^{-16}	[18]
κ_{SE}^{Rb-He}	1.0×10^{-29}	[27]

Table 2.2: The Rb spin-exchange rate coefficients for binary collisions.

Gas atom	Parameter ψ_i [Hz]	Ref.
Xe	5230	[33]
N_2	5700	[37] based on [38]
He	17000	[39] based on [33]

Table 2.3: Values for the parameter ψ_i. The parameter is vdW-specific rate for each gas atom with density $[G_i]$ [34].

2.5 SEOP of ^{3}He

The first nucleus that was successfully hyperpolarized using SEOP was ^{3}He and it has been used in many SEOP experiments. .^{3}He has a small cross section for spin-exchange with alkali metals, so the spin-exchange time is slow, measured in tens of hours. On the other hand, helium, just like xenon, has no nuclear quadrupole moment, thus is characterized by a long spin-lattice relaxation time T_1. Usually it is of the order of tens of hours, but using special precautions can be even longer. This qualifies ^{3}He to be a useful contrast agent for the MRI.

The fundamentals of SEOP of ^{3}He are presented in [24, 27, 40, 41, 42].

^{3}He is hyperpolarized via spin-exchange which occurs during binary collisions only. This simplifies the theoretical model describing the spin-exchange process comparing to ^{129}Xe. However, it takes usually tens of hours to build-up sufficient polarization. Yet, the hyperpolarization of ^{3}He can exceed 70%, while for ^{129}Xe it is no more than 20%.

The fundamental spin-exchange and spin-relaxation mechanisms for K-^{3}He are significantly more favorable as compared to Rb-^{3}He [27]. Unfortunately, the laser system for performing optical pumping in the potassium vapor is less developed than for rubidium and difficult to build. Some improvement was made when a hybrid optical pumping scheme K-Rb was introduced [43]. The standard optical pumping procedure with circularly polarized laser light tuned to 795 nm in the rubidium vapor is performed and then the potassium atoms are polarized by efficient Rb-K spin-exchange collisions.

Until recently, it was believed that if the alkali-atoms polarization reaches unity, the helium polarization should also approach unity. However, an important observation was made [41], that the surface relaxation (*wall relaxation*) is responsible for the polarization losses in ^{3}He. The surface relaxation rate was found to be linearly proportional to the alkali-metal density, and it increases faster than the spin-exchange rate. This limits the obtainable helium polarization. Generally speaking, the limitation can be quantied by a phenomenological parameter X (called sometimes *X-factor*) [41]:

$$P_{He} = \langle P_{Rb} \rangle \frac{\kappa_{SE}[Rb]}{\kappa_{SE}[Rb] + \Gamma_{He}}, \tag{2.20}$$

where parameter X is a part of:

$$\Gamma_{He} = \Gamma_0 + X[Rb]\kappa_{SE} \tag{2.21}$$

$\langle P_{Rb} \rangle$ is the volume averaged rubidium polarization and κ_{SE} is the spin-exchange ratio, given in the Table 2.2, $[Rb]$ is the rubidium vapor density and Γ_{He} the total relaxation rate for He. Γ_0 is considered as a sum of relaxation rates besides the wall realxation. The X parameter was widely studied by NIST and Winsonsin groups and was found to be 0.2 or greater and the value fluctuated from cell to cell. As well as for ^{129}Xe, the SEOP of ^{3}He requires a high polarization of alkali atoms. This is also achieved by using a high power laser light, tuned to the alkali-atom pumping transition.

2.6 Relaxation mechanisms in polarized ^{129}Xe

For a given spin-exchange rate γ_{SE}, which depends on the pumping laser efficiency, the final polarization P_{Xe} is ultimately limited by the spin–lattice relaxation time T_1. It affects both the polarization process and the available storage time of the polarized sample. Hence, in order to optimize the overall efficiency,it is crucial to understand the physical mechanisms that are responsible for relaxation. In recent years, a number of extensive studies concerning the relaxation processes that occur in ^{129}Xe were carried out [44, 45, 46, 47].

In this chapter a brief introduction to the spin-lattice relaxation mechanisms will be presented and the most important conclusions about their origin will be discussed. The total spin-lattice relaxation rate can be defined as a sum of relaxation rates that originate from various mechanisms:

$$\frac{1}{T_1} = \Gamma = \Gamma_p + \Gamma_t + \Gamma_g + \Gamma_w + \Gamma_{O2}. \tag{2.22}$$

The symbols are defined in Table 2.6. The relaxation processes can be divided into two types: *intrinsic* and *extrinsic*.

The intrinsic relaxation is due to fluctuations of the magnetic field dependent caused by spin-rotation and chemical-shift-anisotropy (CSA) interactions [45]. They occur due to the formation of persistent or transient Xe_2 van der Waals dimers. The persistent dimers are created during three-body collisions and they last until the collision with another atom occurs. During that time the relaxation process represented by Γ_p takes place. The persistent dimers are present at relatively low pressure [46]. , As it was predicted theoretically, the experiment showed that for a fixed gas compositions (^{129}Xe with N_2, He and Ar), the relaxation rate due van der Waals dimers is independent of the total gas density [47],although it still depends on the components ratio. It was calculated that concentration of persistent dimers is equal to 0.5% for 1 amagat[1] of xenon [45]. The transient dimers result from binary collisions and their contribution to relaxation rate is negligible in the standard, low pressure SEOP regime. The relaxation due to transient dimers is equal to $1/\Gamma_t = 56/[\mathrm{Xe}]$ [32], and for low xenon contents (up to 2% in mixture as in our case) it can be neglected.

The extrinsic relaxation processes originate from magnetic field gradients (Γ_g), and collisions with paramagnetic impurities in the SEOP cell(including oxygen (Γ_{O2})), or with the glass walls (Γ_w).

The contributions from intrinsic relaxation processes can be kept low for ^{129}Xe densities below 0.1 amagat [46]. In order to reduce the extrinsic relaxation, it is important to produce a highly homogeneous external magnetic field and use clean cells with low content of paramagnetic impurities. In our case, the SEOP cell was cleaned and then evacuated to about 10^{-7} mbar before each run. The wall relaxation mechanisms in the case of ^{129}Xe have not been studied extensively so far, which is in contrast to ^{3}He, where both . coated and uncoated cells were investigated [48, 49, 50]. Some experiments suggests that the dominant relaxation mechanism is the Fermi-contact interaction between the xenon nuclear spin and the valence electron at the glass surface [46].

In xenon SEOP setup, some coatings of the wall containers are used. The silane and siloxane based surface coatings can lengthen the hyperpolarized ^{129}Xe storage time by inhibiting the gas diffusion to the glass surface where it interacts with paramagnetic impurities

[1] 1 amagat corresponds to the number of ideal gas molecules per unit volume at 1 atm (= 101.325 kPa) and 0°C (= 273.15 K) [51]. The density of an ideal gas at STP is 1 amagat = 2.69×10^{19} cm^{-3} [40]

Type	Origin	Contribution	Ref.
Γ_p	long-lived van der Waals dimers (persistent dimers)	$\frac{1}{4.59h}[1+(3.65\times10^{-3})B_0^2](1+r\frac{[B]}{[Xe]})^{-1}$	[47]
Γ_t	spin-rotation relaxation in short-lived dimers (transient dimers)	$\frac{[Xe]}{56.1h}$	[52]
Γ_g	diffusive motion in magnetic field gradients	$D_{Xe}(\frac{\nabla B_\perp}{B_0})^2$	[53]
Γ_w	wall relaxation	$\sim\frac{S}{V}$	
Γ_{O2}	interaction with paramagnetic oxygen	$0.388\frac{p_{O2}[bar]}{1.013}\frac{273[K]}{T}$	[54]

Table 2.4: Definitions of the intrinsic and extrinsic relaxation mechanisms with its origin and the contribution to the total relaxation rate.

[55]. The wall relaxation is also suppressed at high magnetic field [46] and strongly depends on the surface-to-volume ratio of the cell.

A different approach was chosen in the Repetto et al. work [56], where no coatings were used.For experimentally evaluated values: $T_1^t \approx 370$ h, $T_1^p \approx 4.5$ h (in pure Xe), $T_1^{O2} \approx 1000$ h (low oxygen partial pressure : 10^{-6} bar), $T_1^g \leq 500$ h, the total relaxation time was about 18 h.

It is clear from the above discussion that the formation of xenon dimers and the wall relaxation are the main factors limiting the achievable T_1. Therefore the first assumption in the design of the SEOP polarizer was to keep a low xenon concentration. This condition results in choosing a large SEOP cell, which produces a sufficient amount of HP gas during $1 - 2$ batches.

As far as the long-term storage of HP xenon is concerned, the best method is to freeze it at liquid nitrogen temperature, which will be described in the next subsection.

Relaxation of frozen hyperpolarized ^{129}Xe

There are two purposes of cryogenic accumulation of hyperpolarized ^{129}Xe.First of all, at liquid nitrogen temperature the buffer gases can be completely removed from the hyperpolarized ^{129}Xe. The second reason is to minimize the relaxation processes. It was measured that at 77 K (liquid nitrogen temperature) the spin-lattice relaxation time is about 2.5 h [57] and at 4.2 K (liquid helium temperature) it can reach 60 h [58]. The method and apparatus for the cryogenic accumulation of HP ^{129}Xe was patented by Cates et al. [59], and this work led to developing new ways ofcontinuous and long-term storage of HP ^{129}Xein the frozen form.

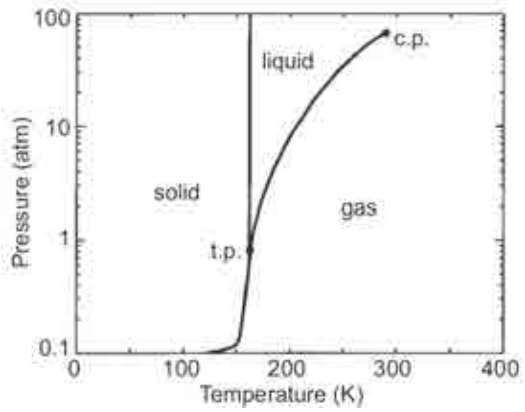

Figure 2.3: Xenon phase diagram [60]. Xenon liquefies at 166 K and freezes at 161 K at standard atmospheric pressure.

The theoretical explanations of relaxation processes in solid ^{129}Xe given in [57, 61, 62] were confirmed experimentally. However, this problem is still not fully understood. It is assumed that the nuclear spin-flip Raman scattering of lattice phonons is the source of relaxation [57]. At low temperature the ^{129}Xe can be also depolarized by ^{131}Xe that is present in the solid sample (abundance of 21.18 %). Such depolarization originates from the cross relaxation between the two isotopes [61], which is mediated by the nuclear dipole-

dipole interaction [62]. The cross-relaxation was confirmed by observing the polarization transfer to ^{131}Xe [61]. The relaxation of ^{131}Xe is very fast since it is also caused by the Raman scattering of phonons but mediated by much stronger he quadrupolar interaction [63]. This leads to the one observation that relaxation in xenon crystal depends on ^{131}Xe appearance, which mainly means that ^{131}Xe atoms behaves as a defects in face-centered cubic ^{129}Xe crystals [64] and producing large electric field gradient leading to quadrupole splitting. In other words, the quality of the xenon crystal and its vulnerability to relaxation depends on physical conditions during the process of condensation from gas to solid [58].

In the generally accepted model describing the relaxation processes in solid xenon the temperature is divided into three ranges, in which different mechanisms dominate [62] where. Below 50 K, the dipole-dipole interaction between ^{129}Xe and ^{131}Xe is responsible for relaxation:

$$V_{dd} = \frac{\mu_\alpha \mu_\beta}{I_\alpha I_\beta r_{\alpha\beta}^3}\Big(\mathbf{I}_\alpha \cdot \mathbf{I}_\beta - 3\frac{(\mathbf{I}_\alpha \cdot \mathbf{r}_{\alpha\beta})(\mathbf{r}_{\alpha\beta} \cdot \mathbf{I}_\beta)}{r_{\alpha\beta}^2}\Big), \tag{2.23}$$

where $\mathbf{I}_\alpha$, $\mathbf{I}_\beta$ are the nuclear spins of two xenon atoms and $\mathbf{r}_{\alpha\beta}$ is distance between them.

Between 50 K and 120 K, the spin-rotation interaction dominates and isdescribed by the following equation [62]:

$$V_{sr} = c_K(r_{\alpha\beta})\mathbf{I}_\alpha \cdot \mathbf{N}_{\alpha\beta}, \tag{2.24}$$

where $\mathbf{N}_{\alpha\beta}$ is the relative angular momentum of the pair of xenon atoms and c_K is the spin-rotation coupling coefficient which decreases exponentially with distance ($r_{\alpha\beta}$).

Above 120 K relaxation is again governed by the V_{dd} interaction, but the expected relaxation time is lower, which is considered to be due to vacancy diffusion [65], both in natural and enriched xenon.

The relaxation time in the frozen ^{129}Xe increases with magnetic field. The longest T_1 of more than 3 hours was reported at 4.2 K and fields above 1 T [62]. It means that large amounts of hyperpolarized ^{129}Xe can be stored in such conditions for a couple of hours.

The most critical moment of the cryogenic freezing procedure is the phase transition. The relaxation mechanism for liquid xenon is believed to be well approximated by Equation 2.24 [32, 66, 67]. Comprehensive measurements in the liquid and solid state show that the relaxation times at the melting point temperature (161 K) are 60 s for 0.2 T and 5 min for 0.4 T [62].

In order to use the HP xenon gas it must be thawed. G. D. Cates et al. reported that the polarization loss during recovery can be of the order of 1 – 2 % [68]. During storage the magnetic field can be kept at lower values $\sim$ 0.2 – 0.7 T (Fig. **??**), while unfreezing should be carried out at the elevated magnetic field to avoid the polarization loss, which can otherwise occur within minutes/seconds. . Consequently,the time spent near phase transition must be minimized. For this reason, a special configuration of the cryogenic unit was proposed by I. C. Ruset et al. [26], which is now universally used in most SEOP setups. The HP gas flows inside a spiral accumulation cell which is located inside the cryogenic dewar. The dewar is filled with liquid nitrogen, but its level is controlled in order to minimize the temperature gradients inside the frozen ^{129}Xe (melted xenon does not mix with xenon snow). This method causes the gas to freeze uniformly, creating a thin surface layer and reducing relaxation. The system allows also to quickly remove liquid nitrogen when the gas is thawed.

3

Characterization of atoms participating in SEOP

3.1 Alkali-metals

Among the alkali metals, potassium, rubidium and cesium are most interesting for the SEOP technique.

The application of K in ^{129}Xe SEOP experiments was reported in [69]. Extensive studies on Rb-^{129}Xe spin exchange at the atmospheric pressure were conducted by Cates et al. [33], and some new results for a similar pressure range for K-^{129}Xe and Cs-^{129}Xe were obtained by Shao et al. [70]. The experimental results show that the ratio of spin-exchange (favorable process) to spin-rotation (unwanted process) varies considerably among the alkali-metal atoms.

Rubidium is a quite popular alkali metal for optical pumping experiments, due to high density of its vapor in the temperature range of 100 - 200^{o}C (Fig.3.1), and the good separation of D_1 and D_2 lines. The fact that relatively inexpensive, high-quality, high-power laser sources are available, also favors Rb.

There are two stable isotopes in natural rubidium: ^{85}Rb and ^{87}Rb, and their properties are describes in Table 3.1. The D_1 and D_2 lines correspond to the transition to the first excited state $5P_{1/2}$ and $5P_{3/2}$ of ^{85}Rb, respectively (see Fig.3.2).

Isotope	^{85}Rb	^{87}Rb
Abundance	72.2 %	27.8 %
Nuclear spin	5/2	3/2

Table 3.1: Natural rubidium isotopes

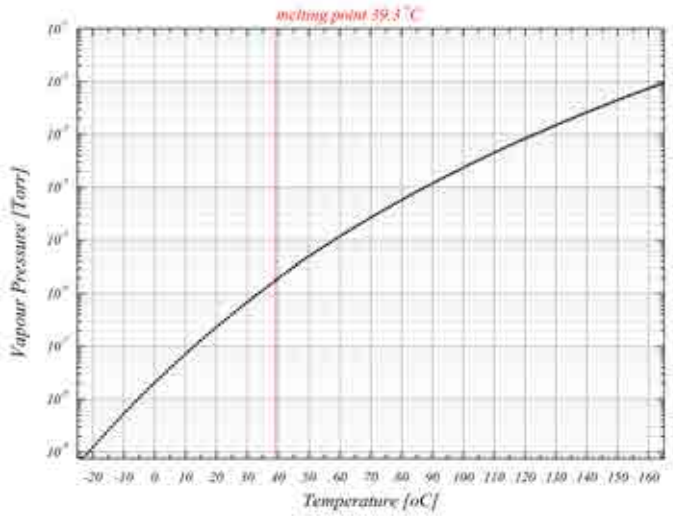

Figure 3.1: Vapor pressure of Rb calculated in [71, 72]. The vertical line indicates the melting point of 39.3^{o}C. The SEOP is performed at temperatures ranging from 70° – 180°, depending on the total pressure in the cell.

The valence electrons in the rubidium vapor are polarized by optical pumping. A simplified scheme of OP is presented on Figure 3.3. The laser light is tuned to to the 794.7 nm wavelength, corresponding to the $5^2S_{1/2} \rightarrow 5^2P_{1/2}$ transition, . The $^2S_{1/2}$ and $^2P_{1/2}$ are the ground and the first excited states, respectively. In the presence of magnetic field these states are split into two sublevels described by the magnetic quantum number $m_J = \pm 1/2$. The angular momentum from the right circularly polarized light $\sigma+$ is transferred from photons to rubidium valence electrons. For $\sigma+$ photons have a spin magnetic moment $\mathrm{m}_J = +1$ and are absorbed by rubidium atoms according to the $\Delta\mathrm{m} = +1$ selection rule. During one optical pumping cycle the $^2P_{1/2}, m_J = +1/2$ state is populated and subsequently it decays back to the ground state. The decay processes obey the magnetic quantum number selection rule $\Delta m_J = 0, \pm 1$ (with the emission of photon with π and $\sigma\pm$ polarization, respectively). After a number of cycles the atoms are deposited in the $^2S_{1/2}, m_J = +1/2$ state, thus producing a net orientation of the Rb electron magnetic moment in the ground state.

In order to achieve a high spin polarization, the build-up process must be faster than the ground state electron spin lattice relaxation. An extensive theoretical study of electronic relaxation during optical pumping in rubidium atoms is presented in [73].

All Rb relaxation processes that do not contribute to the Rb^{129}-Xe spin-exchange, are referred to *the spin destruction* (SD) and are characterized by the κ_{SD}^{Rb-i} parameters (their values are presented in Tab. 2.1). The following processes are described below: Rb-Rb collisions, Rb collisions with buffer gases or with the walls of the container.

Rb-Rb collisions conserve the total angular momentum of colliding alkali atoms, but redistribute it among the ground-state sublevels. The collisional Hamiltonian has the following form [24]: $V_{ex} = J\mathbf{S}_i\mathbf{S}_j$, where the $J = J(R)$ coupling coefficient is of electrostatic origin.

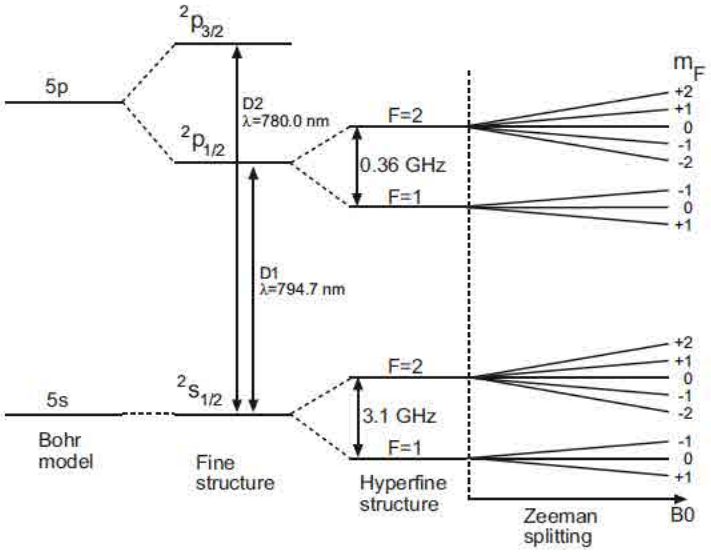

Figure 3.2: ^{85}Rb atomic structure in an external magnetic field. The two rubidium D_1 and D_2 lines are indicated.

Rb collisions with buffer gases occur during a short time which is typical for binary collisions and cause the relaxation of electronic polarization. The spin destruction parameters for the Rb-buffer gases processes were calculated elsewhere, see Table 2.1.

Wall relaxation is pressure independent but depends on the cell geometry (surface to volume ratio) and its surface properties (paramagnetic impurities). This type of relaxation can be minimized in a high field regime or by using glass with smaller para- or ferromagnetic centers content and covering the cell walls with special coatings [55].

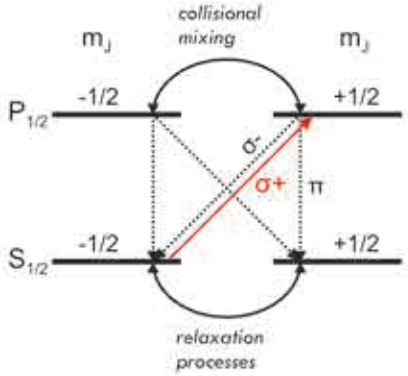

Figure 3.3: Simplified rubidium optical pumping scheme (the Rb nuclear spin is neglected) for the laser light of positive helicity tuned to D_1 ($^2S_{1/2} \rightarrow {}^2P_{1/2}$ transition). The collisional mixing of the atomic sublevels is described in Section 3.3.

3.2 Xenon

As it is summarized in Table 3.2, xenon has two stable isotopes possessing non-zero spin: ^{129}Xe and ^{131}Xe, both with sufficient natural abundance.

Isotope	^{129}Xe	^{131}Xe
Abundance [%]	26.44	21.18
Nuclear spin	1/2	3/2
Giromagnetic ratio $[\gamma_n/(2\pi)$ MHz $T^{-1}]$	11.777	3.496

Table 3.2: Properties of natural stable xenon isotopes.

Large xenon electron cloud makes ^{129}Xe a good marker for NMR studies due to its outstanding sensitivity to surroundings. It has been shown that the largest chemical shift in xenon compounds reaches 7500 ppm (Fig. 3.4) [74]. Since xenon NMR spectroscopy in not the main topic of this thesis, only a few examples of xenon as a contrast agent will be given. The first group of materials that were tested with ^{129}Xe were porous materials, e.g. Na-Y zeolites [4, 75] and mesoporous silica gels [76]. A possibility to study diffusion in cavities and surface properties in materials by the ^{129}Xe NMR spectroscopy has provided a great tool for chemistry and biology.

A real breakthrough for medicine was an idea of lung imaging with hyperpolarized ^{129}Xe, which was co-invented by A. Mitchel [77]. The ^{129}Xe properties allow to measure the amount of gasous ^{129}Xe or ^{129}Xe dissolved in a tissue or blood quantitatively [11]. There is relatively large separation of peaks of different amplitudes in the HP ^{129}Xe NMR spectrum of lungs. This allows to test such physiological parameters as perfusion, alveolar surface area, septal thickness, interphase diffusion kinetics, and blood kinetic exchange rates, and notice their changes caused by the evolving pulmonary disease.

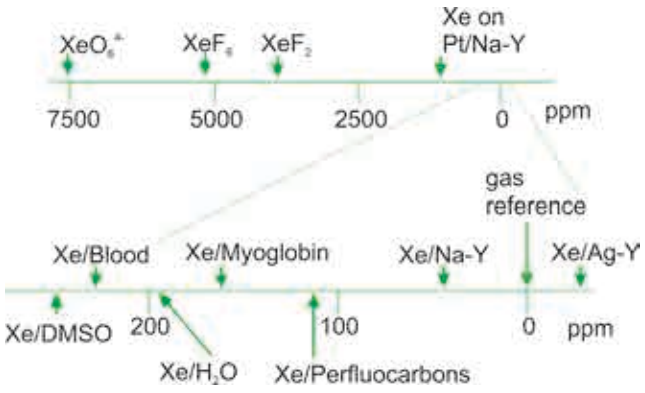

Figure 3.4: Xenon chemical shift scheme adapted from [74].

In contrast to ^{129}Xe, the ^{131}Xe isotope has not been studied extensively. It was first observed by the NMR technique in 1954 [78]. The ^{131}Xe has nuclear spin 3/2, so its nuclear electric quadrupole moment interacts with electric field gradients. This dominant interaction

is responsible for both broadening of NMR spectral lines [79], and substantially shorter than 1 s relaxation time T_1. The NMR spectrum is a triplet with different broadening for main and satellite peaks. The nuclear polarization in thermal equilibrium for spin $I > 1/2$ nuclei is equal to:

$$P = \frac{|\gamma|\hbar B_0}{3k_B T}(I+1). \tag{3.1}$$

For ^{131}Xe at 9.4 T and 300 K it is 4.41×10^{-6} [79]. The enhancement factor that can be achieved by SEOP is on the order of 5000. The final ^{131}Xe polarization strongly depends on the xenon total density (as the rubidium polarization is xenon density dependent), but is mainly limited by the short nuclear relaxation of ^{131}Xe. In consequence the SEOP method for ^{131}Xe is much less efficient than for ^{129}Xe, and is not used in any NMR applications involving hyperpolarized markers.

3.3 Buffer gases

Due to relatively narrow absorption line only about 1% of the laser light is absorbed by the alkali-metal vapor [39], producing its low polarization. A higher polarization can be achieved by adding buffer gases. Compared to helium, xenon gas is not convenient as the pressure broadening medium, because it depolarizes the optically pumped alkali-metal. Two buffer gases are commonly used: helium (isotope ^{4}He) and nitrogen (N_2). Fukutomi et al. [80] studied the application of foreign gases to the optical pumping mixture at the total pressure of 1 bar. They observed that the polarization increases with the decreasing amount of Xe gas. The composition of Xe, N_2 and ^{4}He must be optimized to balance the spin polarization of the alkali-metal atoms during optical pumping with their depolarization caused by collisions with the buffer gas atoms. Apart from reducing the Rb vapor diffusion towards the walls, there is a number of reasons why buffer gases are crucial for making the SEOP process efficient:

Pressure line broadening. The interaction between the Rb electronic cloud and the buffer gas atoms distorts the Rb atomic sub-levels. The resulting shift of the atomic energy level depends on the intermolecular distance between interacting atoms. The observed line broadening and the line shift increase with pressure, because the atomic distance becomes smaller. The broadenedD_1 line of the alkali vapor results in more efficient absorption of the laser light. Operating at lower pressures – 1 bar or less, though, impose using laser with linewidth narrowed.

Radiation trapping. It takes place in an optically thick alkali vapor. Normally, the alkali electron would relax back to its ground state by emitting a randomly polarized photon, which can scatter several times in the vapor [7, 81].This process would reduce the pumping rate. Therefore the N_2 gas is introduced into the SEOP mixture in order to quench the excited atoms during collisions with them, causing them to relax to the ground state non-radiatively. The N_2 is known to be efficient in dispersing the energy associated with the vibrational and rotational modes of the molecule and has a large quenching cross section, of the order of 50 Å [7]. The amount of nitrogen that is necessary to minimize the radiation trapping differs in various SEOP setups.

Collisional mixing. Collisions of Rb atoms with ^{4}He and N_2 results in *collisional mixing* of atomic sublevels, which leads to the redistribution of the excited state electrons among

their Zeeman sublevels. The transition probabilities, characterized by the Clebsh-Gordon coeffcients, are following: 1/3 for $5^2P_{1/2}$, $m_J = +1/2 \rightarrow 5^2S_{1/2}$, $m_J = +1/2$ transition (the same azimuthal quantum numbers) and 2/3 for $5^2P_{1/2}$, $m_J = +1/2 \rightarrow 5^2S_{1/2}$, $m_J = -1/2$ transition (different azimuthal quantum numbers). The collisional mixing equalizes the spin populations of the excited states, causing the transition probabilities to be also equal: 1/2. This contributes significantly to the spin-exchange process and increases the optical pumping efficiency. Statistically, three photons are needed in average to pump one atom into the final polarized state, but in the presence of collisional mixing two photons aresufficient. The ground states are also susceptible to such collisional mixing, but with a smaller probability. The mixing of ground state levels contributes to the spin-destruction rate.

The third body. Both N_2 and ^{129}Xe take part in the process of the van der Waals molecule formation, being responsible for the energy conservation during the collision.

Comment

Taking into consideration all physical processes affecting the SEOP that were described in the previous sections, the main idea of the SEOP polarizer to be constructed was developed. The decisions were made concerning the choice of alkali metal, the corresponding laser source, the noble gas, and many other technical parameters. The SEOP polarizer was designed to work at the atmospheric pressure with a low content of the ^{129}Xe gas in the SEOP mixture contained in a large SEOP cell (about 6 L inner volume). This is unique comparing to majority of other SEOP designs, which use high-pressure and small-volume cells. To our knowledge, there is only one similar polarizer developed by the Hershman group [26].

4

The polarizer

Schematically, the polarizer consists of the following components: (a) the system of coils producing a homogeneous magnetic field, which is parallel to the direction of the laser light, with the strength of a few tens of Gauss, (b) a glass cell (the SEOP cell) with the alkali-metal droplet connected to (c) the gas distribution system, which controls the gas compostion inside the SEOP cell, and (d) the outlet directing the polarized gas to the accumulation system, (e) the laser system and (f) the NMR detection system. Each component of the presented ^{129}Xe SEOP polarizer was carefully designed and built from the scratch.

4.1 Construction and general remarks

The general aim of the design was to build a simple and mobile ^{129}Xe SEOP polarizer. Aluminum profiles (30 × 30 mm, *Rexroth Bosch Group*) form a frame (1750 × 650 × 650 mm), which supports two aluminum plates. The first plate is situated at the top and is connected with the second plate located at the bottom with four brass roads (⌀1 cm) and two profiles. The first plate was drilled in order to provide holes for mounting the optical components. This plate will be called the optical table. In addition, a big hole at the center of the optical table was cut for the laser beam and became handy for the pumping cell installation. The bottom plate prevents the rods from bending and is a support for an aluminum container. This plate has also a round hole cut in order to provide a window for the laser tests (rubidium absorption and laser power loss after passing the SEOP cell as described in Section 5.1). Two aluminum profileswere mounted below the optical table and used as a track for a special plexiglas frame (see Section 4.2). Additional aluminum profiles were added transversely between the main profiles on four sides, in order to prevent the main frame from twisting. All materials are nonmagnetic – only aluminum or brass were used. Since most small brass screws and nuts were not available commercially due to their unique shapes, they were manufactured by the technical workshop.

4.2 Homogeneity of the magnetic field

A homogeneous magnetic field within the volume of the SEOP cell is required. The value of magnetic field was chosen to be 21 G – a value below the range shown to decouple molecular spin exchange (following the paper [82]). Eight rectangular copper coils generating the field were mounted on four brass rods inside the aluminum frame They can be moved along z-axis and located in the required position with about 1 mm precision. The coils are connected in series (6 external + 2 internal) and powered separately by two current sources (PSM-6003, *GW Instek*), so it was important to calculate the ratio between the two currents to achieve the best homogeneity.

The simulation of magnetic field distribution was based on the Biot-Savart equation for a rectangular current loop [83] with dimensions $a \times a$, $a = 430$ mm and different numbers of turns: 80, 92, 102, 116 (for pairs going from the center to the end). We set the z – axis and the x – y plane to be parallel and perpendicular to the magnetic field, respectively. The final value of the magnetic field induction is a sum of fields generated by all loops. This value was simulated initially using Matlab.

(a) (b)

Figure 4.1: Movable plexiglas frame for the fluxgate magnetometer positioning (a). Four four brass rods inside the aluminum frame supporting coils (b).

The eight coils were first arranged to optimize the field homogeneity on the central axis (0, 0, z). The main challenge was in positioning the coil with maximum precision, as the simulation showed that even 1 mm shift in one coil position causes a dramatic change of the magnetic field homogeneity. The final coil arrangement was set with the help of a three-axis fluxgate magnetometer (M03 Three-Axis Fluxgate Magnetometer, *Barrlington*). Three components of magnetic field $\vec{B}$ (B_x, B_y, B_z) were mapped with the resolution of 0.001 Gauss. The fluxgate was mounted on a moving frame, which could move up and down inside the coils parallelly to the z-axis, sliding between the two aluminum profiles (Fig. 4.1a).

The moving frame consists of two plexiglas plates connected by eight brass pins, so that their relative position is fixed. Each plate has 20 holes for positioning the magnetometer in the x – y plane. Each hole has 25 mm diameter and the distance between their centers is 35 mm. The map of the maximum values of magnetic field inhomogeneity throughout the

SEOP cell volume isshown on Figure 4.2. The coordinates of the fluxgate magnetometer are given on the x and y axes, while the numbers represent the largest inhomogeneity that measured measured across 80 cm in the z direction. The shape of the contour lines at the bottom of the graph suggests some asymmetry in the magnetic field, which can be caused by the presence of wires which attach coils to power suppliers, or by the measurement setup itself (the magnetometer readout was sensitive to a small displacement inside the holes).

The position of coils and the currents were established after several iterations. The magnetic field inhomogeneities inside the coils and inside the SEOP cell were found to be 0.15 and 0.05 Gauss, respectively, for the main field equal to 10 Gauss. To produce the field of 21 Gauss, the corresponding currents for internal and external coils were equal to 2.79 and 3.16 A. The experimental values of magnetic field along the z axis together with simulated values are presented on Figure 4.3. Since the magnetometer can operate at the range of 0 – 10 Gauss, the results are given for lower magnetic field of order of 7 Gauss.

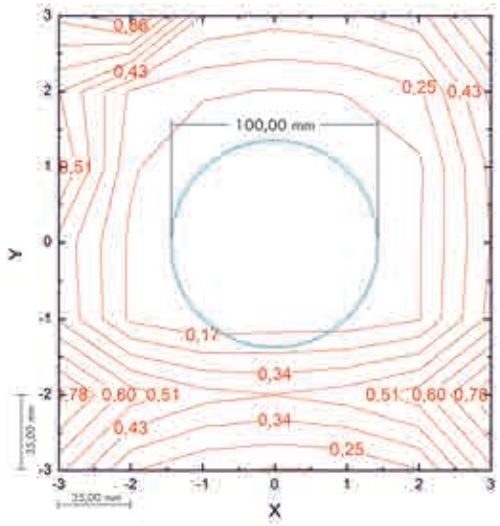

Figure 4.2: The map of magnetic field inhomogeneity near the SEOP cell: the coordinates of the fluxgate magnetometer on the x – y plane are given on x and y axes, while the values (in red) represent the maximum inhomogeneity measured along 80 cm in the z – direction, expressed in Gauss. The circle indicates the SEOP cell location inside the coils.

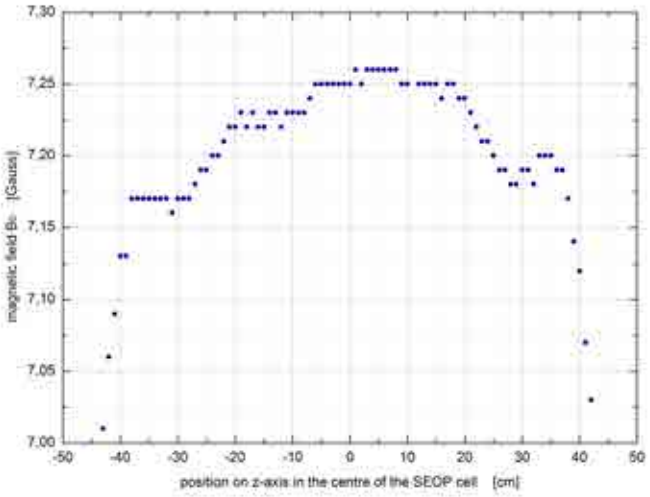

Figure 4.3: Magnetic field B_0 measurement for magnetic field of order of 7 Gauss (matching magnetometer working regime).

4.3 Rubidium

A 5 gram rubidium ampoule (99.75%, argon sealed in the breakseal ampoule, *STEM*) was connected with a metal-glass connector (Stainless Steel to 7740 Pyrex Tube Adapter, 1/4", *Swagelok*) in order to fit the stainless steel tubing system. A small glass inset with a magnetic pin inside was sealed to the ampoule in order to be able to break the safety glass ending with the pin. After fixing the rubidium ampoule in place, it was evacuated, about 1 atmosphere of nitrogen was added and then the metal piece was heated up to 45^oC, so that it melted. This process was necessary in order to remove the argon layer.

Initially, we tried to transfer the rubidium vapor through the heated stainless steel pipes (*Swagelok*) to the SEOP cell. Despite locating the ampoule in a hot oil bath (up to 140 – 160°C), the filling of the SEOP cell with 5 grams of rubidium was unsuccessful. The diameter of the pipes was too small and the rubidium vapor had a tendency to condense on their inner walls in the first place. Therefore the initial setup was modified to shorten the distance between the ampoule and the SEOP cell, which led to a significant improvement of the rubidium transfer.

The SEOP cell was first carefully cleaned with phosphoric acid and acetone.

In the improved setup (Fig. **??**), the ampoule was connected to the metal-glass connector with the 2-component epoxy adhesive glue and no valve was used . As it is shown on Figure 4.8, the only remaining valves were *M1* (the main valve for shutting off the gases), *P3* (the pump valve) and *F1* (the blind exit e.g. for a phantom) , and the second ampoule was located behind the *K1* valve on the T-connector (Swagelok). Additionally, in order to prevent rubidium from going in the direction of *K1* valve, a pipein front of the T-connector has a *U-shaped* form. After evacuating the whole system with the turbo molecular pump (TMP) (TPS-compact, *Varian*) to below 10^{-7} mbar, the glass protection was broken and the ampoule was heated manually with the air blower. The glass protection was broken using a home-made coil that was wired around the ampoule and powered by the auto-transformer (AC current, 50 Hz), which made the metallic pin move up and down and break the glass.

Figure 4.4: Pictures of rubidium ampoules: inside the aluminum container (a) and after the rearrangement in the final position (b).

Figure 4.5: The metallic rubidium inside the SEOP cell viewed from the optical window at the top of the cell.

Afterwards the coil was removed. This procedure allowed all metallic rubidium to reach the SEOP cell when it was warmed.

In Figure 4.5 the metallic rubidium is present inside the SEOP cell as viewed from the optical window at the top of the cell (a), and from the bottom through the glass window of the aluminum chamber (b), respectively.

4.4 Gas distribution

A xenon gas enriched with the ^{129}Xe isotope (> 91 %) isotope was used in experiments. The SEOP of ^{129}Xe requires rubidium vapor and buffer gases - ^{4}He and N_2, which are distributed from the inlet system presented in Figure 4.6. The supply is provided from the three bottles:

1. ^{129}Xe, enriched (> 91 %): 0.5 l, 77 bar, 99.9999% purity, *Spectra Gases*
2. ^{4}He: 99.9999%, purity *Linde*
3. N_2: 99.9999%, purity *Linde*

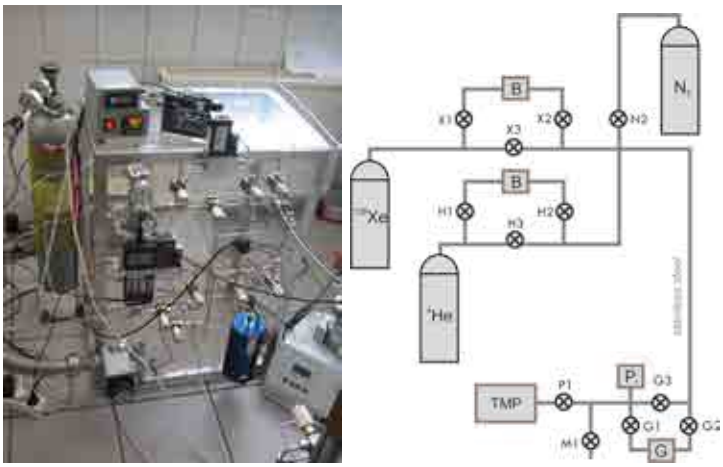

(a) (b)

Figure 4.6: ^{129}Xe polarizer inlet system picture (a) and scheme (b). B - flow meter (Brooks), P - pressure transducers, G - getter filter, TMP - turbo molecular pump, *X1*, *X2*, *X3* - ^{129}Xe gas distribution valves, *H1*, *H2*, *H3* - ^{3}He gas distribution valves, *N2* - N_2 gas distribution valve, *G1*, *G2*, *G3* - getter inlet and outlet valves, *P1* - turbo molecular pomp valve, *M1* - main valve.

Nitrogen is distributed manually through the reductor and the valve (*Swagelok*). All valves are certified to be helium leak-tight. Xenon and helium supplies are additionally equipped with the flow controllers (*Brooks*) for the precise gas volume selection, however this pathway can be omitted, depending on the valves position. All tubes (*Swagelok*) were cut, bended and connected with the valves and other inlet system components with the tube fittings (*Swagelok*). The obtained gas mixture is filtered with two filters: 5 μm (*Swagelok*) and the getter filter (P52QC50R2, *Saes Getters*). The pressure inside this system is measured by the pressure transducer (S Model Transducer, *Swagelok*) equipped with the properly calibrated voltmeter. The inlet system is evacuated using the turbo-molecular pump (TPS-compact, *Varian*). After several hours of heating, the vacuum reached 9.6×10^{-7} mbar on the pump gauge. The inlet system is connected to the polarizer by a stainless steel tubing, so the gas mixture goes directly to the SEOP cell via the *M1* valve (the labels of all valves are shown on Figures 4.6b, 4.8).

4.5 The SEOP cell with heating and cooling system

The SEOP cell is located in the center of the polarizer, surrounded by the set of coils and mounted inside the aluminum container. The cell is supported by a Teflon ring from the bottom and attached by an aluminum clip to the polarizer frame at the top. The cell is a glass (Pyrex) cylinder 80 cm long with the outer and inner diameters of 10 cm and 9.5 cm, respectively. The optical window for the laser beam has a diameter of about 9 cm. The cell has two outlets - five cm long glass tubes terminated by the KF 16 flanges, so that they can be easily connected to other parts of the polarizer with the glass or stainless steel flanges through the glass-to-metal chain clamps (*Evac*).

During the SEOP process the cell must be kept at a high temperature of up to 160°C. The heating system consists of an aluminum chamber filled with 25 liters of silicone oil (silicone fluid linear, AK 350, Wacker®), which is thermally isolated by glass wool and additional aluminum cover. Four blocks of wool are attached to the chamber with needles. The oil temperature can be controlled from room temperature up to 200^{o}C with a bifilar pair of heaters and the temperature regulator (PID 500-1-0-00, *Java Automatic*), which is additionally monitored by the PID Temperature Controller with the PT100 probe. It takes less than 2 hours to reach 160°C. At the elevated temperature the metallic piece of rubidium becomes a thick vapor. The bifilar arrangement of the heater avoids the generation of magnetic field inhomogeneity.

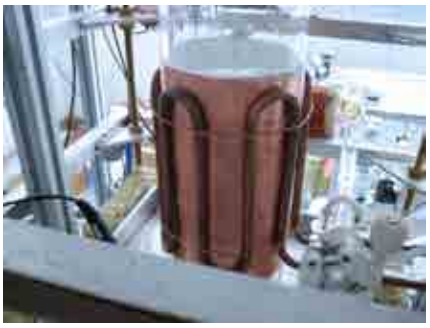

Figure 4.7: The rubidium removal system: the cooling medium is a bended copper pipe which clamps a copper sheet around the SEOP cell.

Rubidium must be removed from the gas mixture at the output and this is achieved by a cooling band attached to the cell at about 2/3 of its height. The cooling band is a bended copper pipe which clamps a copper sheet around the cell (Fig. 4.7). Additionally, some thermal paste was added between the pipe and the copper sheet to improve the thermal contact. During the cooling process the pipe is filled with circulating water and rubidium atoms condense in the cold region. The experiment showed that there is no macroscopic amount of rubidium above the cooling band. Otherwise rubidium could be seen at the top of the cell and would have to be removed manually with the air blower or with heating bands warmed up to 120°C and left for a couple of hours. During the cleaning process the bottom of the SEOP cell must be maintained at the room temperature.

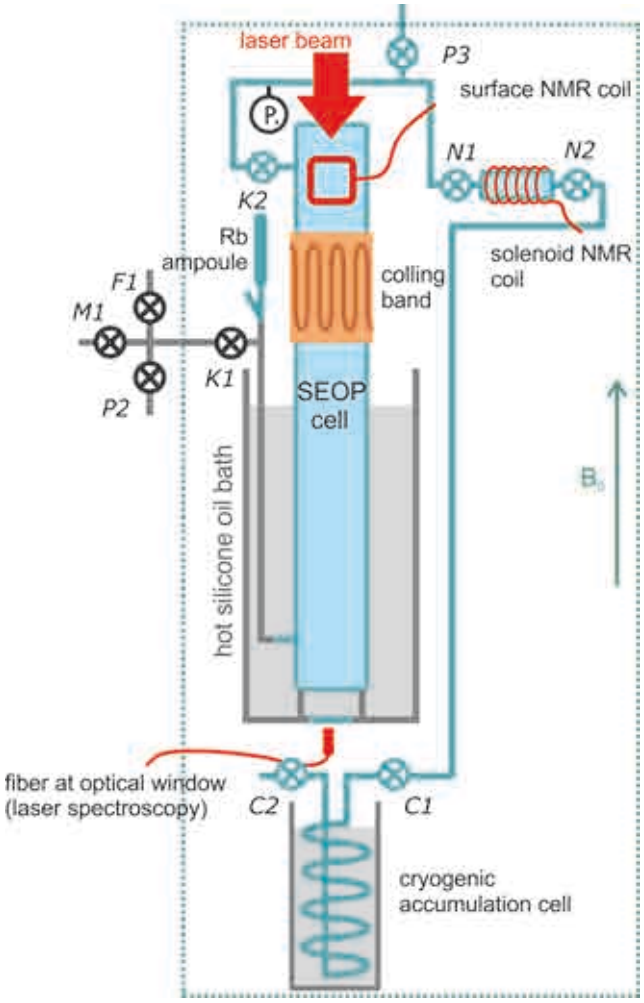

Figure 4.8: A complete scheme of the ^{129}Xe polarizer: The SEOP cell with hot and cold regions and the cryogenic system areshown. The gas inlet system is not presented here in detail (see Figure 4.6). *M1* - main valve, *K1*, *K2* - SEOP cell inlet and outlet valves, *N1*, *N2* - the NMR test cell inlet and outlet valves (NMR coil was built but not tested during the experiment), *C1*, *C2* - the cryogenic accumulation cell inlet and outlet valves, *P2*, *P3* - valves for turbo molecular pumps, P - pressure meter. The cryogenic accumulation cell is located under the polarizer in its magnetic field. The solenoid NMR coil and cryogenic accumulation cell were bulit, but not tested.

4.6 Gas outlet

The gas outlet presented on Figure 4.8 starts with the *K2* valve, from which the polarized gas is transported by a Pyrex glass tube to the *C1* valve, which is in front of the cryogenic accumulation cell. This part was manufactured by local glassblower. An additional exit (*P3* valve) was prepared for connecting a turbo-molecular pump (*Pfeiffer*) for cleaning purposes.

The pressure inside the gas outlet (including the SEOP cell) is measured by a membrane pressure gauge (*Honeywell*) attached to a small glass tube. The pressure gauge is read by a custom made calibrated microcontroller system.

The overall view of the polarizer is presented on Figure 4.9. Four copper sheets cover the aluminum frame in order to eliminate any light reflections and provide some electromagnetic shielding at the same time.

Figure 4.9: Overall view of the xenon polarizer. Four copper sheets s mounted on aluminum profiles form a Faraday cage (one wall was removed for closer look inside). The optical setup can be seen at the top, also enclosed during operation.

4.7 Laser and optics

The first step of the SEOP process is optical pumping. Therefore a laser source providing the circularly polarized light is the prerequisite component of the polarizer. In order to make the SEOP process efficient, two conditions must bemet: high power laser and full illumination (without dark regions) of the SEOP cell.

The first condition can be fulfilled by using commercially available laser diode arrays (LDA), which are commonly used for SEOP experiments, for their high power, compactness, and low cost. LDA produces tens to hundreds of Watts of continuous wave power by integrating many individual laser diode emitters into a single array. Due to some differences in individual laser diodes, the spectrum of the whole array cannot be well characterized by a Gaussian profile [84]. Nevertheless, it has a typical linewidth of 2 nm FWHM. . The important design criteria of LDA are the number of emitters, their width and spacing. The best beam quality and brightness is obtained by using a small number of closely spaced emitters. Still, the main weakness of conventional LDAs is the broad 2 - 3 nm non-uniform line shape of the emitted light, compared to the relatively narrow 0.1 nm alkali metal absorption bands, resulting in a significant inefficiency of the laser power absorption.

The problem of spectral mismatch causing low laser power absorption by alkali metals can be resolved by increasing the pressure in the optical pumping cell, which leads to broadening of the Lorentzian-shaped atomic absorption lines. However, this method cannot be applied to continuous flow, large volume xenon polarizers, which operate at the atmospheric or even lower pressure. Therefore two new techniques of increasing the laser power density at the required wavelength have been proposed recently: the application of an external cavity [84, 85], and the use of volume holographic gratings (VHG) [86, 87, 88].

Chann proposed to narrow the frequency range of the LDA stack by collimating the light from each emitter [84]. Then the light is reflected off a diffraction grating at a uniform angle and returned to the emitter with high efficiency. Channs setup produces 14 Watts of output from 20 Watts input power with the linewidth of 60 GHz.

Unfortunately, this narrowing method becomes complicated due to so called *smile* effect, which is a small curvature of the linear arrangement in the LDA. *Smile* causes a number of technical difficulties such as inequality of the central wavelengths coming from all emitters, different incident angles or astigmatism of the optical apparatus, and the alignment errors [89]. The *smile* compensation is essential for a good LDA performance and it can be done by the introduction of an additional plane mirror, which makes the spectral distribution among emitters uniform [89].

An alternate way is to use Volume Holographic Gratings (VHG), also known as Volume Bragg Gratings (VBGs), which was reported to narrow the laser line with efficiency exceeding 90% [90]. VHG is made of photosensitive glass bulk slabs [91] which contain Bragg planes with varying indices of refraction [92]. Such components are manufactured by holographic techniques and are characterized by a high optical damage threshold. VHG operates as an external feedback, which feeds a narrow portion of the laser emission spectrum (with the wavelength characterized by gratings) back into the laser cavity [87].

Two different laser system were used for our SEOP experiments . The first is a home-made laser system based on a high power laser diode equipped with VBG, while the second is a commercial two-diode array laser (Scientific DUO FAP System, FWHM = 2 nm laser spectrum, maximum power of 60 W, *Coherent*). The first one will be described in this section, while the second was used at the beginning of experiments just after polarizer assembly and was eventually replaced. A short description of this initial setup is presented

in *Appendix A*.

A high power laser diode narrowed and stabilized to 794.7 ± 0.6 nm (M1B-794.7[0.6]-35C-VBG, *DiLas*) is driven by a CW laser diode driver (CW, 60 Watts, LDD-60-4, *Ekspla*). A home-made cooling unit consists of two Peltier cooling modules matching the diode geometry and possessing the recommended heatsink capacity of > 70 Watts per bar. All electronics parts are enclosed in a metal box (Fig. 4.10b), while the diode with accompanying optics is mounted on the radiator directly on the optical table (Fig. 4.10a). The schematic diagram of electronics is presented on Figure 4.11[1].

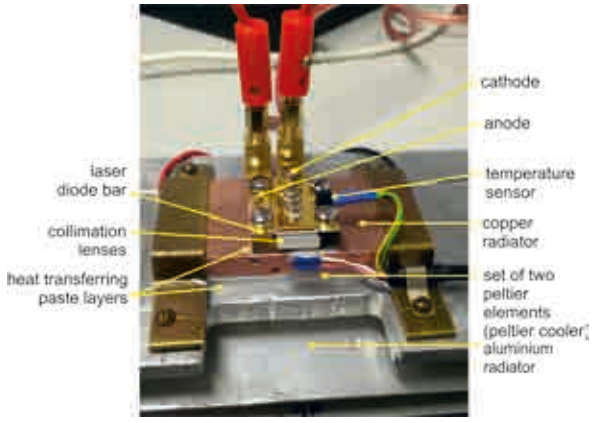

(a)

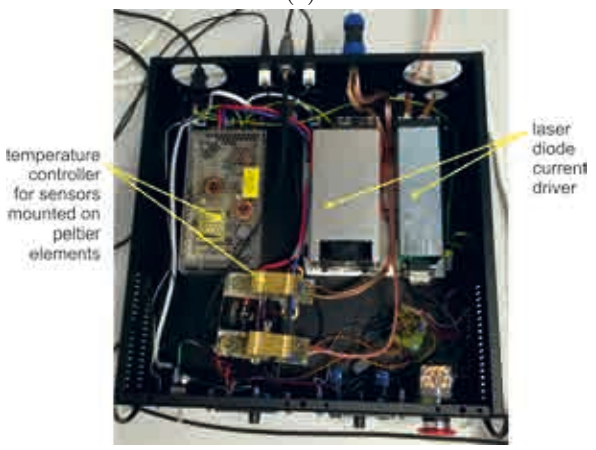

(b)

Figure 4.10: High-power laser diode mounted on radiators (a) and its current and temperature controllers are enclosed in a metal box (b).

[1] The electronics design and assembly was done by Janusz Kuzma, Atomics Optics Depatment; The schematic diagram was provided by Janusz Kuzma

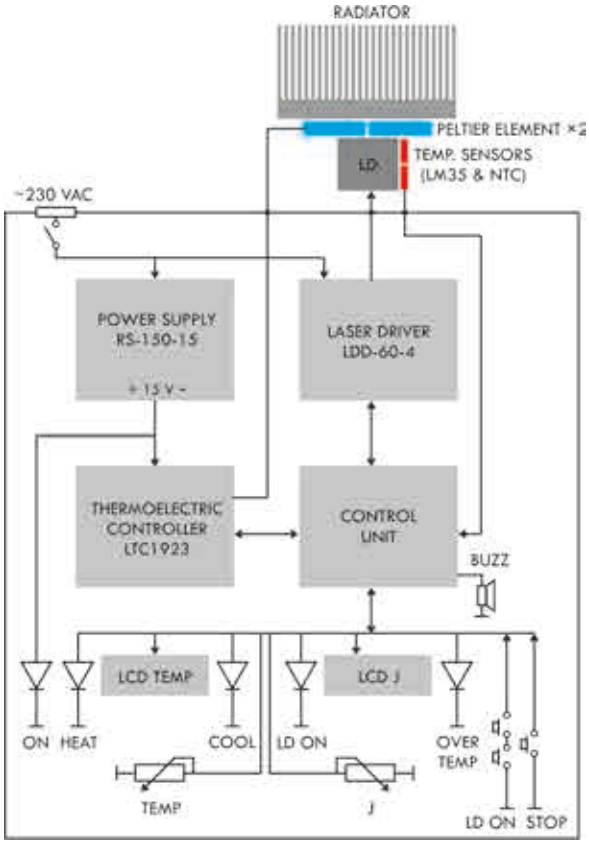

Figure 4.11: The scheme of high power laser diode with CW laser diode driver and cooling unit used in the ^{129}Xe polarizer.

An accurate design of the optical setup is required to provide a uniform illumination over the entire volume of the SEOP cell. It is quite a hard task if a large SEOP cell is used, making the optical arrangement complicated. A full illumination prevents the depolarization from unpolarized Rb atoms, and a proper light alignment (parallel to magnetic field) reduces the skew light effect [93]. In the case of using the fiber, the beam is expanded with a set of circular lens. When the diode bar is chosen, an additional cylindrical lens must be used to reshape the beam from linear to circular profile. The optical arrangement is described below.

The original output beam from the laser diode is highly divergent, astigmatic, and has anelliptical profile. For this reason, a collimating optics consisting of cylindrical lens (*Dilas*) must be mounted in front of the diode output. The aperture width after the collimating lens is about 9 mm and now the beam spot is elongated, which is undesirable for most applications. In order to match the beam profile with the optical window of the SEOP cell, another set of optical components was applied. The scheme of the experimental setup showing the laser beam configuration is presented in Figure 4.12. Two telescopes for the beam collimation and circularization were used, both made of a set of two lenses: ocular and object-lens. The first telescope uses two cylindrical lenses, L_1 (Plano-Concave Cylindrical

Lens, f = -25 mm, BK7, 19 × 25 mm, *Eksma Optics*) and L_2 (Plano-Convex Cylindrical Lens, f = 500 mm, BK7, 50 × 50 mm, *Eksma Optics*). Next the beam is directed to the polarizing beam splitter (PBS) and because diode laser light is linearly polarized (parallel), after a half-wave plate (Quartz Multi Order quarter waveplate, retardation l/2 at 795 nm, coated at 795 nm, diameter 75 mm, *Eksma Optics*) the linear polarization direction is rotated and the beam goes perpendicular (only s – polarized beam leaves PBS). The linearly polarized beam is circularly polarized by a quarter wave plate (Quartz Multi Order quarter wave plate, retardation l/4 at 795 nm, coated at 795 nm, diameter 75 mm, *Eksma Optics*). Two mirrors (BK7, SF $\lambda/10$ at 633 nm, coated $HR > 99.5\%$ at 795 nm for 45^o, *Eksma Optics*) direct the beam into the SEOP cell, but before that the second telescope (lenses L_3 and L_4) expands the beam profile. Calculated distance between the lens L_3 (Biconcave Lens, BK7, f = -200, *Eksma Optics*) and L_4 (Biconvex Lens, BK7, f = 500 mm, *Eksma Optics*) is 470 mm.

Again, all optical components are enclosed in a protective box. Apart from the ventilation module that was used in the previous set-up, an additional ventilation sleeve was mounted to the aluminum radiator. This provides an extra air wash to the complicated radiator structure and keeps this component cooler during many hours of operation.

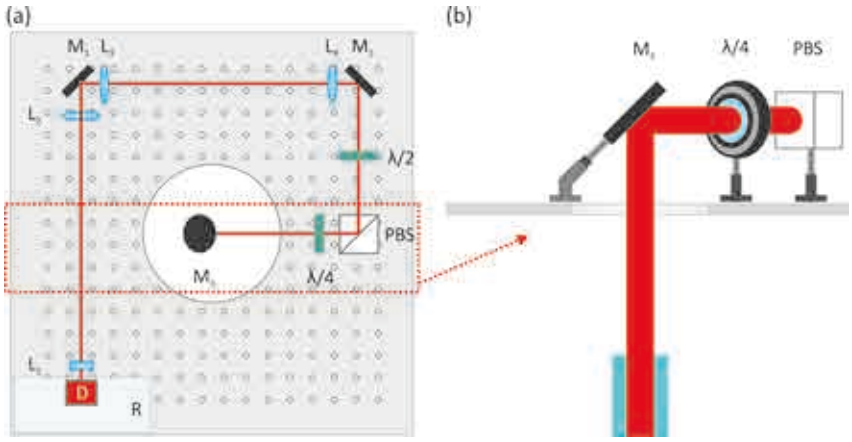

Figure 4.12: Scheme of the optical system designed for the high-power laser diode. Figure shows the arrangement on the optical table (a) and the beam path to the SEOP cell (b). D – diode, R - radiator, L_1, L_2 – cylindrical lens (the first telescope), L_3, L_4 – spherical lens (the second telescope), PBS - polarizing beam splitter, M_1 – dielectric mirror located after the first telescope, M_2 – dielectric mirror located after the second telescope and directing the laser light into the polarizing optics, M_3 – dielectric mirror mounted at the 45^o angle with respect to the optical table and directing the circularly polarized laser light into the SEOP cell, $\lambda/4$ – quarter-wave plate, $\lambda/2$ – half -wave plate.

Figure 4.13: The optical table with laser diode and optics for the beam alingment.

4.8 Low Frequency NMR Spectrometer

The Low Frequency NMR Spectrometer (Aurora, *Magritek*), designed to work in the $0 \div 100$ kHz frequency range, was used for monitor the NMR signal from the polarized ^{129}Xe. The Aurora includes a built-in low frequency transmiter and receiver, so that no additional equipment is required except for the NMR coil. The spectrometer is connected to a PC via the USB interface and a easy to use software *Prospa* controls data acquisition and processing.

A tuned RF coil must be designed for NMR transmitting and receiving.. A short description of the NMR coil implementation will be given below. The resonant frequency of the RF coil is determined by:

$$f = \frac{1}{2\pi\sqrt{LC}}, \tag{4.1}$$

where L is inductance of the coil and C capacitance, which is connected in series to form a resonant circuit.. For better performance two separate coils should be used for transmitting and receiving. The transmitting coil should produce a uniform, magnetic field B_1, which is perpendicular to the main static field and used to excite the nuclear spins. Therefore it is usually a large Helmholtz coil. The receiving coil is perpendicular to both the main and the B_1 fields, in order to minimize the coupling during transmission. Together with the tuning capacitors, the transmitting and receiving coils form a serial and parallel resonant circuit, respectively, to match the output impedance of the transmitter and the input impedance of the receiver. The energy losses in the resonant circuit can be represented by the equivalent resistance R, which includes the resistance of the coil and RF losses. The quality factor Q is defined as: [94]:

$$Q = \frac{L\omega_L}{R}, \tag{4.2}$$

where ω_L is the operating frequency. Q determines the sensitivity of the receiving coil and the ringing time of the transmitting coil following the RF pulse.

The Aurora spectrometer operates with a single transmitting-receiving coil. The spectrometer has a built-in duplexer, which switches the RF coil between the transmitting

and receiving modes automatically. A parallel tuning capacitance can be set by the software.Therefore a small saddle coil 6 × 6 cm made of 80 turns of copper wire was made. The RF coil parameters are presented in Table 4.1. For tuning to the resonance frequency (24700 Hz) an external capacitor connected in parallel was used and the internal capacitance in the Aurora system was set to zero.

RF coil			
R [Ω]	9.1	Q	22.5
L [mH]	1.3	f [Hz]	24700
C [nF]	31	N	80

Table 4.1: The transmitting-receiving RF coil characteristic. Q – quality factor at resonance frequency, N – number of turns, C – capacitor connected parallel to the coil.

4.9 Preparation of cryogenic accumulation unit for HP xenon

As it was explained in Section 2.6, the cryogenic accumulation is one of the ways to storage the HP ^{129}Xe at minimum polarization losses. The second job of cryogenics is to separate the HP xenon from the buffer gases and rubidium. Most of the polarization survives the phase transition (when proper physical conditions are satisfied), so large quantities of HP gas can be stored for transport. It is also a convenient way to gain time for preparing an experiment involving HP xenon (MR imaging, spectroscopy). The experimental values of longitudinal relaxation time are of the order of days at 4.2 K and 1000 G [61]. The main steps in preparing the cryogenic accumulation is to quickly and completely freeze and re-freeze the HP ^{129}Xe.The time of both steps must be minimized because at temperatures close to the xenon melting point (161 K), the relaxation rate increases due to vacancy diffusion in the solid. This would result in polarization losses in the freeze-and-thaw cycle and exclude the feasibility of xenon MR experiments.

The second method which is based on the accumulation of the HP xenon in a gaseous state is less complicated. It was developed in order to simplify the polarizer design [95]. Rubidium filters are required in this approach, as rubidium contamination is hazardous (only less than 5 ng amounts are accepted in medical applications). A proper cool-down of the SEOP cell and a rapid transfer of the gas into the Tedlar bag must be provided and optimized, taking into account the relaxation in the gas phase [95]. A successful experiment resolving these problems was reported in [56].

The method of storing and delivering HP xenon depends on particular applications. In our case it was to be used in a medical facility, which is located at a long distance from the lab. Therefore it was decided to build the cryogenic accumulation unit, although it is more complex to construct and handle.

Two accumulation units were built, each equipped with a Pyrex glass spiral cell with inlet (*C1*) and outlet (*C2*) valves (see. Fig. 4.8) located inside two cryogenic dewars (5L, CX500, *Taylor-Wharton*).

The magnetic field is generated by a solenoid made of copper wire wound on a PCV tube. The wire is fiberglass coated. After winding 245 turns, an additional layer of glue was applied to fix the wires in place.

A special mounting made of Teflon (PTFE) was designed to match the dewar neck (216 mm diameter) in a way, that it hangs on the neck as a lid. The lid has a lower part – a frame designed for two Helmholtz-like coils. The RF Coil consists of two rectangular coils (23 cm × 7.5 cm) in parallel, each made of 80 turns of copper wire in the cotton cover. The Helmholtz-like refers to the fact that their distance is not equal to their radius. The coil was tuned with capacitors and connected to a male BNC.

The presented unit was designed and built, but it was not tested yet. The procedures of transporting the HP xenon to the cryogenic glass cell, storing and recovering will be carried out in next months.

(a) (b)

Figure 4.14: The accumulation unit: during test with liquid nitrogen (a) and its spiral glass cell (b).

Final note about the polarizer assembly

During the time when the polarizer was in the process of assembling and testing, the whole laboratory was moved to another facility. In the new location the polarizer was put inside a Faraday cage (Fig. 4.15). The polarizer, the gas distribution system and two turbomolecular pumps were placed inside the cage, while the gas bottles were kept outside the cage and connected via the cage wall. The NMR electronics and the new laser diode temperature and current control units were also located outside the cage and connected via tubes in the cage walls.

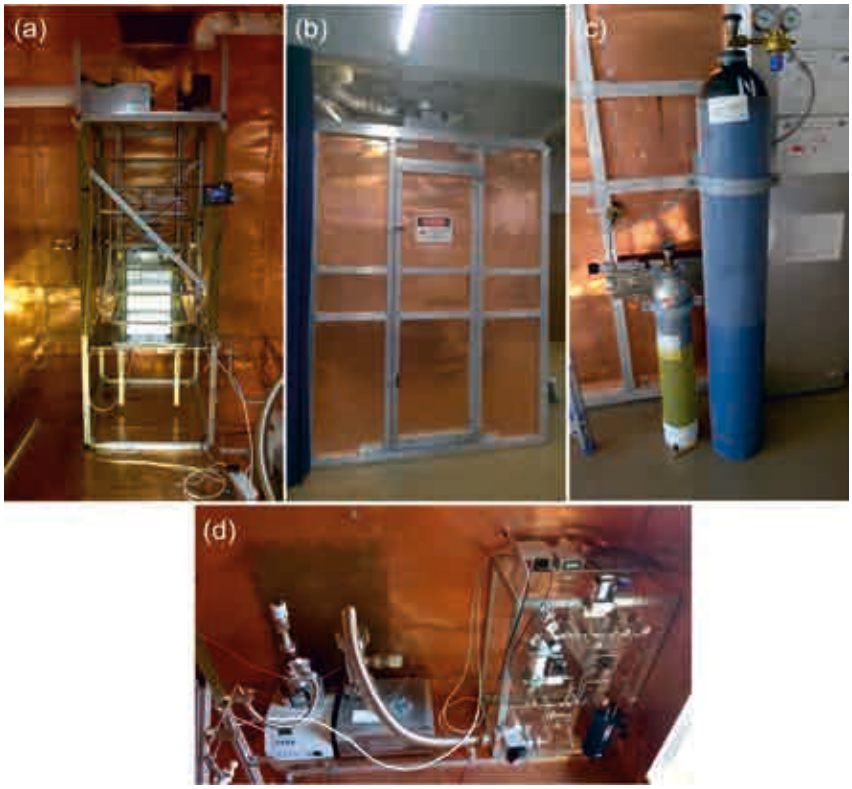

Figure 4.15: The experimental setup: the ^{129}Xe SEOP polarizer (a) is located inside the Faraday cage (b) with the gas distribution system and turbomolecular pumps (d). Two of three gas bottles (^{4}He and N_2) are located outside the Faraday cage (c).

5

The experimental results

5.1 Optimization of the laser system

There are three critical issues in the laser system design for the SEOP experiment: obtaining sufficient output power of the order of tens of Watts, full illumination of the optical pumping cell, and narrowing the laser spectral width to match the D_1 line profile of rubidium. . The laser source current and temperature control is characterized in this section. After mounting the diode laser on a cooling radiator, first tests were performed in order to evaluate: (a) output power versus current, (b) axial and horizontal divergence of the beam, and (c) wavelength tuning by the temperature change.

The laser power was measured for two temperatures of the diode bars: 20.0°C and 23.0°C, using the power meter (Medium Power Thermal Sensor – 400 mW to 300 W, *Ophir*). The results are shown on Figure 5.1.

The next step was to check the radiator performance. A small optical temperature sensor (BM859CFa, *Brymen*) was attached to the radiator to measure its temperature during the laser operation. Its output was connected to the USB port of the computer. When the current increased from zero to the maximum value of 40 A for a given diode temperature (eg. 20.0°C), the radiator temperature rose from 22.2°C to 28.0°C. When the laser operated at the maximum current for a longer time, the radiator temperature reached about 30.0 – 31.0°C. For this reason, an additional cooling was necessaryby the ambient air, which was delivered through the pipes. The diode temperature was then stabilized and operated at the desired 25.0°C for many hours without overheating.

The evaluation of the beam divergence was required to properly design the optical beam-shaping system. The laser diode (D) was mounted on the optical table with screen (S) and CCD camera (CCD) (Fig. 5.2a). The screen is made of the semi-transparent paper with the millimeter scale, so that the increase of the beam diameter as a function of the screen diode distance could be observed by the camera. The distance between the screen and camera was kept fixed, and the distance between the diode and screen (d) changed from 10 to 140 cm. The measurement was made for the current above the threshold current of the diode (10 A), when all bars are switched on uniformly. The horizontal and vertical divergences were measured to be 1° and 0.1°, respectively.

The last step was a proper wavelength tuning for the rubidium optical pumping. For a fixed current of 40A, the temperature of the diode was varied. A simple setup (shown on Fig 5.2b) consisted of the power meter (PM), which was located on the laser beam axis, and a collimator, placed at an angle. Part of the laser light reflected from PM was collected by the collimator and analyzed by a spectrometer (HR 4000, *Ocean Optics*). The results presented in Figure 5.3, show that the 794.7 nm wavelength which corresponds to the D_1 line of rubidium can be obtained by setting 25°C and 40 A. The temperature was eventually corrected to 25.5°C, when the same measurement was performed in the SEOP cell with the rubidium vapor present.

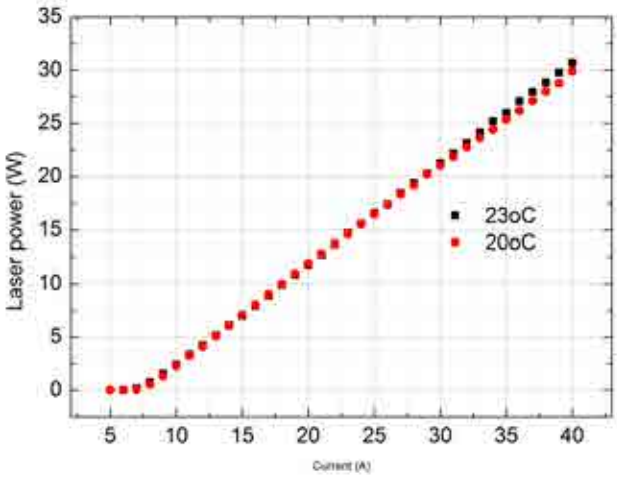

Figure 5.1: The diode laser (*Dilas*) power as a function of current measured for two diode bars temperatures 20.0°C and 23.0°C .

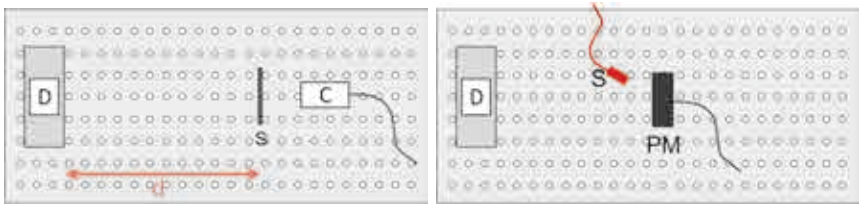

(a) (b)

Figure 5.2: Optical setup for diode laser tests of beam divergence (a) and wavelenght with temperature tuning (b). D – diode mounted on radiator, PM – power meter, S – screen, d – distance between diode and screen, C – collimator.

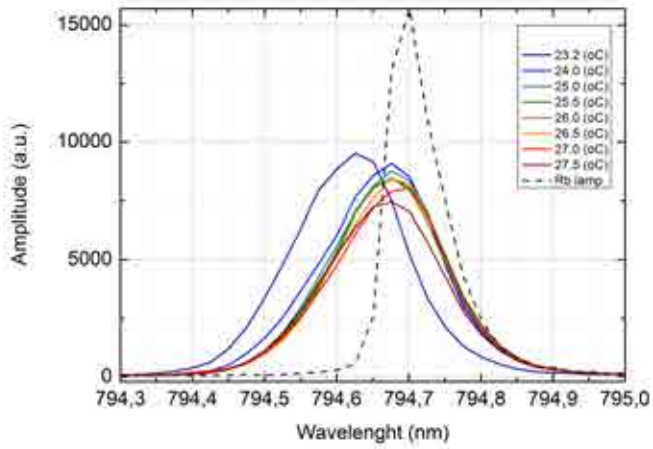

(a)

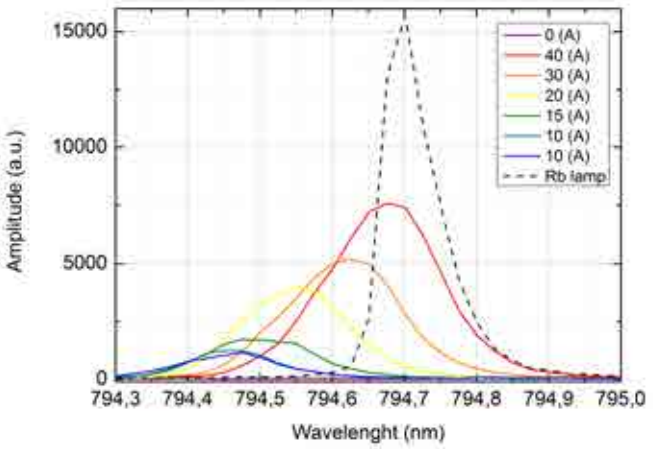

(b)

Figure 5.3: The laser diode (*Dilas*) wavelength tuning for a fixed current of 40 A (a) and a fixed temperature of 28°C (b). The OP transition at 794.7 nm corresponds to ∼25°C and 40 A.

The eventually chosen laser source is characterized by a narrow output spectrum, achieving better matching to the Rb D_1 line. In Figure 5.4 the difference in the laser spectral widths is presented. The laser diode (*Dilas*) with the spectrum narrowed to 0.2 nm (red) and the laser diode array (*Coherent*) with the broad spectrum of 2.0 nm (green) were operating at their maximum powerof 30 W (and 25.5°C) and 60 W, respectively and their spectra were measured by a spectrometer (HR 4000, *Ocean Optics*). The old (*Coherent*) laser system is described in *Appendix A*.

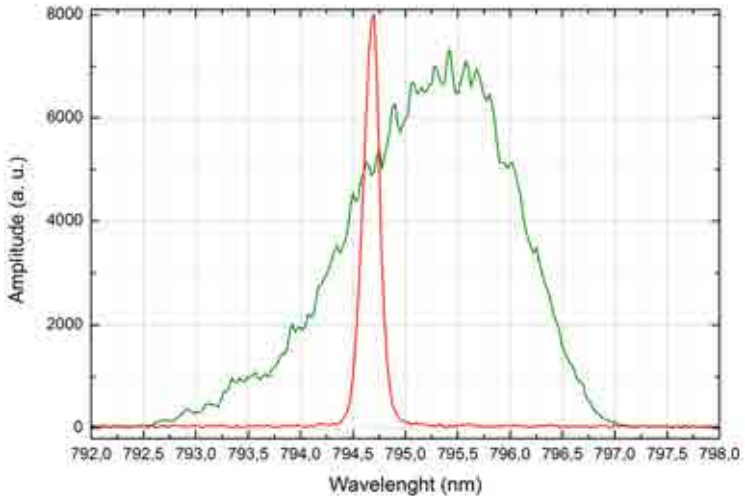

Figure 5.4: Comparison of output spectra of the laser diode (*Dilas*) with the spectrum narrowed to 0.2 nm (red), and the laser diode array (*Coherent*) with the broad spectrum of 2.0 nm (green), both operating at their maximum power of 30 W and 60 W, respectively.

5.2 Rubidium absorption in SEOP cell

Rubidium reference cell

An initial test was performed using a rubidium reference cell with known rubidium density of $9.69 \cdot 10^9$ cm^{-3} at 23°C. The laser equipped with the temperature controller (TED 200C, *Thorlabs*) and the laser diode current controller (LCD 205 C, *Thorlabs*) was tuned to 780 nm (D_2 Rb line). The laser beam was split with a nod. About 4% of laser intensity passed the rubidium reference cell and measured by the PD1 photodiode (Fig. 5.5a). The second part of the beam, of about 92% of laser intensity, was collimated, directed to the SEOP cell by the fiber, and measured by the PD2 photodiode.

Two rubidium spectra measured after the rubidium reference cell and after the SEOP cell were compared at the beginning of each experiment to make sure there is a rubidium vapor in the latter (Fig. 5.5b). For natural rubidium, the D_2 spectrum consists of four peaks corresponding to F=1 and F=2 for ^{87}Rb and F=2 and F=3 for ^{85}Rb, when no magnetic field is present.

This setup was used to check whether the rubidium vapor reached the SEOP cell when the first rubidium ampoule was disposed.

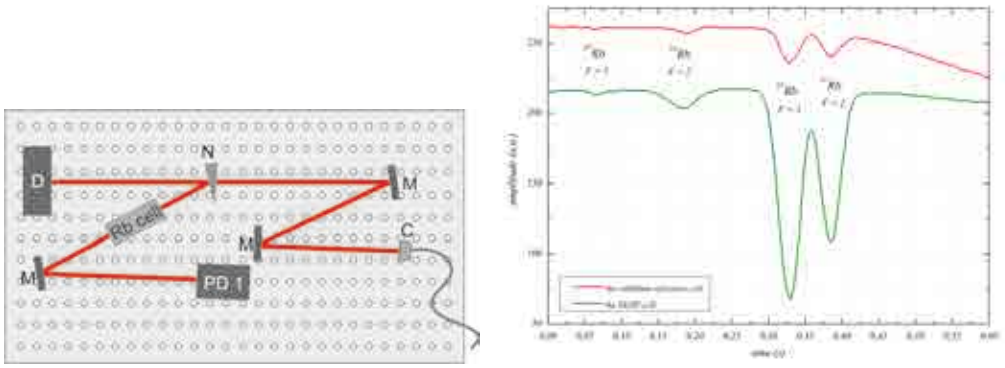

(a) (b)

Figure 5.5: The scheme of optical table with rubidium reference cell (a), where: D – 780 nm laser diode, N – nod, M – mirror, PD1 – photodiode, C – collimator and fiber for beam going to the SEOP cel; D_2 unsaturated absorption spectrum of both rubidium isotopes (^{85}Rb and ^{87}Rb) in the reference cell (red) and in the SEOP cell (green) (b).

Absorption profiles in the SEOP cell

The xenon and buffer gases were added to the SEOP cell during the experiment and the laser light absorption was measured by the HR 4000 spectrometer (*Ocean Optics*). The temperature and pressure were increased and the gas ratio modified in order to find the optimum set of physical parameters, which leads to the highest NMR signal from HP ^{129}Xe in this specific SEOP polarizer. Computational modeling predicts even higher laser light absorption when the laser characterized by a narrow line is used [39]. By comparing the present experiment with the previous results that are presented in the *Appendix A*, this prediction was confirmed.

After rubidium was introduced to the SEOP cell, gases were added always in the same order, first ^{129}Xe, then N_2 and finally ^{4}He up to 1 bar at 160°C). Simultaneously, the absorption profiles of the light passing through the SEOP cell and reflecting from the surface of the power meter were measured with the spectrometer. When the temperature increased from room temperature to 160°C, the rubidium vapor was getting more dense, thus more laser light was absorbed and less light was captured after the SEOP cell. In order to avoid the saturation of the spectrometer, two filters were used at the beginning of this procedure, which were removed afterwards, when the rubidium vapor was getting dense.

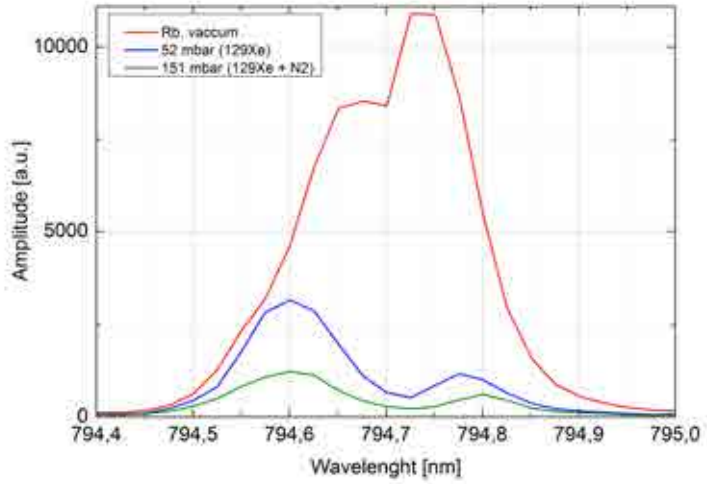

Figure 5.6: Rubidium absorption profiles for rubidium vapor (vaccum) at 80°C (red), after adding 52 mbar of ^{129}Xe (blue) and 151 mbar of N_2 and ^{129}Xe (green).

The first result is shown on Figure 5.6. As it can be clearly seen, adding just 52 mbar of ^{129}Xe to the rubidium vapor increases the absorption significantly. The experiment was repeated for various gas ratios and the changes in the absorption profiles were observed at the temperature varied from ∼80 to 160°C (Fig. 5.7a and 5.7b). The amplitudes of the profiles are getting smaller with growing temperature, which means that the absorption of the laser light in the vapor increases. Near maximum temperature of 160° the profile disappears almost completely, which is an experimental confirmation that the 0.2 nm laser light spectrum matches the rubidium D_1 line of ∼0.1 nm. In contrary, when the previous laser of 2 nm linewidth was used, only a small fraction of the laser light was absorbed, as it is presented in *Appendix A*. In order to compare the lasers of wide and narrow spectra, it is useful to introduce the coefficient of laser power per unit linewidth, in Watt/nm. Such comparison is shown in Table 5.1. The laser of narrow spectrum supplies five times more Watts per nm, improving the optical pumping efficiency, when only 65% of power of the wide line laser (*Coherent*) is used.

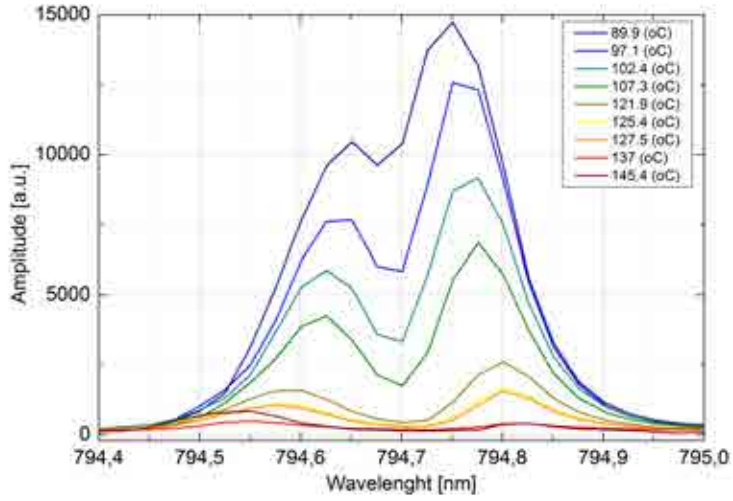

(a)

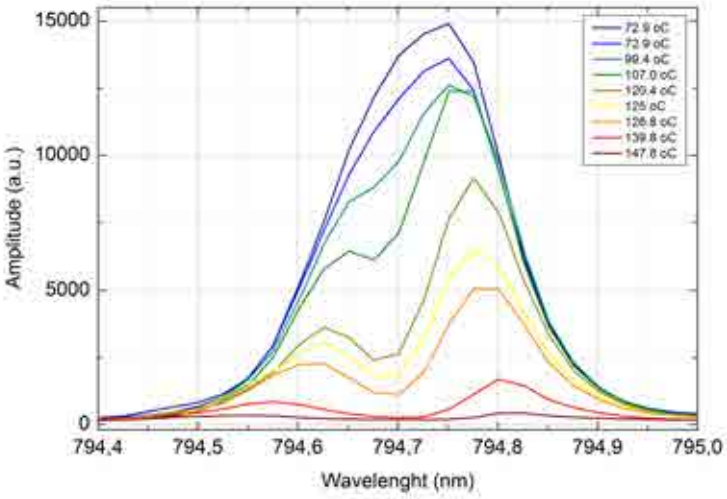

(b)

Figure 5.7: Variation in the absorption profiles for two extremal $^{129}Xe : N_2 : {}^3He$ gas ratios used for SEOP: 5 : 10 : 85 % (a) and 2 : 10 : 88 % (b). With growing temperature the maximum of the profile is getting smaller , indicating the increasing absorption of the laser light by the Rb vapor in the SEOP cell

Temperature in the SEOP cell

The Beers absorption law can be used to calculate the absorbance for a given dimension of the SEOP cell and known rubidium density. The density was calculated from Equation 5.1

Laser type [nm]	Maximum power [Watt]	Power measured* [Watt]	Coefficient [Watt/nm]
0.2	30	16	150
2.0	60	46	30

Table 5.1: Comparison of power per unit linewidth for the two lasers used. *refers to the laser power measured at the optical window of the SEOP cell.

SEOP Mix no.	^{129}Xe	N_2	^{4}He
1	5	10	85
2	2	10	88
3	2	20	78
4	2	30	68

Table 5.2: Various gas mixture ratios used for SEOP expressed in %.

[97] for a given temperature (see also Fig. 3.1):

$$[Rb] = \frac{10^{10.55(4132/T)}}{k_B T} \times 10^{-7} cm^{-3} \tag{5.1}$$

where k_B is the Boltzmann constant and T temperature in K. It is believed that at temperatures close to the oil temperature of 120 – 140°C the rubidium densities are around $2.01 - 6.2 \cdot 10^{13}$ cm^{-3}. However, the density distribution is rather inhomogeneous due to non-uniform rubidium evaporation and gas mixing, which was confirmed in numerous experiments exhibiting the anomalous regions of reduced Rb polarization [96].

5.3 The NMR signal from gasous polarized ^{129}Xe in the SEOP cell

The dependence of the ^{129}Xe polarization efficiency on parameters such as: gas composition, pressure, cell temperature is monitored in situ via low-field NMR. In contrast to ^{3}He, there is no optical method to assist NMR technique (see details in *Appendix B*). The problem with any novel ^{129}Xe polarizer design is that it does not comes with manual, and confirmation of its proper operation comes from probing nuclear signal of HP gas. The last step is nuclear signal from HP ^{129}Xe calibration with reference water sample, which allow to fully parameterize polarizer performance.

Tuning to resonance frequency

In the simplest NMR experiment, the population of nuclei will be subjected to excitation pulse (magnetic field B_1), applied at the Larmor frequency:

$$f = \frac{\gamma}{2\pi} B_0, \tag{5.2}$$

where γ is the gyromagnetic ratio, equal to 11.777 MHz per T for ^{129}Xe, and B_0 the static magnetic field. The SEOP experiment is performed at 21 G (0.0021 T) yielding f = 24.7 kHz.

After the RF excitation pulse, a resonance (NMR) signal at the same frequency is received. This signal S is directly proportional to the polarization P according to:

$$S \propto \gamma^2 N P, \tag{5.3}$$

where N is the number of excited nuclear spins.

RF pulse calibration

The maximum NMR signal is generated by the 90° RF excitation pulse, which rotates the magnetization to the transversal plane. It is necessary to properly adjust its length and amplitude, taking into account the effects of temperature, pressure, and the gas content ratio in the SEOP cell.

The Aurora low-field spectrometer software allows to specify the following parameters:

- RF pulse – B_1 *pulse duration [ms]*, *transmit level [V]*,
- receiver characteristics– *receive gain*, *acquisition delay [ms]*,
- sequence timing – *repetition time [s]*.

Other parameters determine the spectral bandwidth and the number of data points acquired.

Initial settings of NMR parameters were made using the MEOP experiment with ^{3}He, simultaneously with the optical method of measuring nuclear polarization. Details of the MEOP as well as the optical method are provided in *Appendix B*.

Since a similar optical method for ^{129}Xe is unknown, the RF pulse calibration was done during the SEOP experiment. A mixture of ^{129}Xe, N_2 and ^{4}He at the total pressure of 1013 mbar was illuminated with the laser beam (*Coherent* laser, maximum power 46 W at the optical window), in the presence of static magnetic field. For a fixed resonance frequency of 25102 Hz, the NMR signal as a function of the RF pulse length and amplitude was measured. The highest signal was observed for the B_1 pulse duration of 2 ms and 3 V amplitude (see Fig. 5.8). The ringing time of the RF coil was found to be about 400 μs.

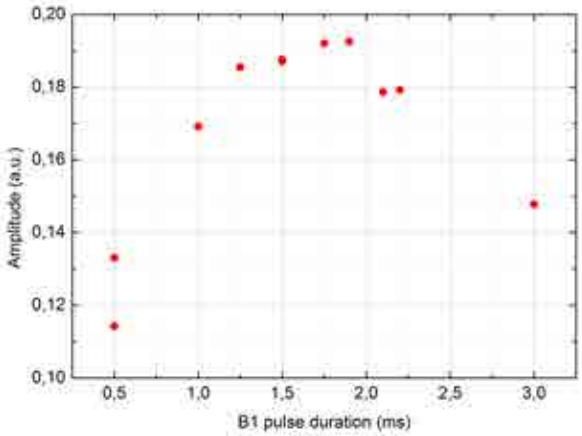

Figure 5.8: Determination of the 90° RF pulse length for the RF coil interfaced to the Aurora spectrometer. Data points were fitted to the sinus function.

Polarization calibration

The absolute polarization of HP ^{129}Xe can be calculated by comparing the NMR signals from xenon and the thermally polarized water sample, using the following equation 5.4:

$$P_{Xe} = \frac{S_{Xe} P_H N_H \gamma_H sin(\alpha_H) f(\nu_H) e^{-\frac{t_{dH}}{T_{2H}}}}{S_H N_{Xe} \beta_{Xe} \gamma_{Xe} sin(\alpha_{Xe}) f(\nu_{Xe}) e^{-\frac{t_{dXe}}{T_{2Xe}}}}, \tag{5.4}$$

where S_{Xe} and S_H are the NMR signals for HP ^{129}Xe and ^{1}H, respectively. N is the number of corresponding nuclei, $\beta_{^{129}Xe}$ the xenon isotopicabundance, γ the corresponding gyromagnetic ratios, α the flip angles. To simplify the calculations (and omit the RF coil retuning), the same resonance frequency was used in both measurements by reducing the magnetic field to 0.59 mT in the case of ^{1}H. The 90° RF pulse lengths were equal to 2.1 ms and 0.55 ms for xenon and protons, respectively. The exponential factors take into account the transverse relaxation effects that reduce the NMR signal due to the delays t_d between the end of the RF pulse and the start of data acquisition. The number of ^{129}Xe nuclei was calculated from the ideal gas equation, whereas N_H is equal to:

$$N_H = \frac{2\rho_{H_2O} V N_A}{18}, \tag{5.5}$$

where ρ_{H_2O} is the water density, V the sample volume, and N_A the Avogadro constant.

P_H is the nuclear polarization of water in thermal equilibrium:

$$P_H = \frac{h\gamma_H B_0}{2k_B T} \tag{5.6}$$

At room temperature, 298 K, in 0.59 mT magnetic field, for the proton gyromagnetic ratio of 42.63 MHz/T, the proton polarization was calculated to be $2.02 \cdot 10^{-9}$. Such a small value is not a problem to measure for a high density water sample. The number of ^{129}Xe atoms to be inserted into Equation 5.4 was calculated from:

$$N_{Xe} = \frac{p_{Xe} V}{k_B T_{Xe}}, \tag{5.7}$$

where p_{Xe} is the partial pressure of ^{129}Xe, V the volume, and T_{Xe} the gas mixture temperature. An enriched ^{129}Xe was used in the experiment, so $\beta_{^{129}Xe}$ equals 0.91.

The $f(\nu)$ is a Lorentzian function describing the frequency response of the RF coil. Since the NMR signals for both HP ^{129}Xe and thermally polarized ^{1}H were measured by the same coil at the same frequency, these factors in Equation 5.4cancel. T_2 are the spin-spin relaxation times, which were calculated from the FWHM linewidths of the corresponding NMR spectra. These are in fact the effective transverse relaxation times T_2^*, which take into account the magnetic field inhomogeneity effects. The delay times t_d were in the range of 3 – 4 ms.

The ^{1}H NMR signal was obtained from thermally polarized water sample located inside the same solenoid, which will be used in the cryogenic storage system. To match the resonance frequency to that for ^{129}Xe, the current was set to 0.917 A, which corresponded to 0.59 mT field. The weak signal was accumulated, using the repetition time of 6s, letting the longitudinal magnetization fully recover between the consecutive scans. The acquisition delay was equal to 6 ms, to avoid the ringing effects. Typical HP ^{129}Xe and ^{1}H NMR spectra acquired on the Aurora spectrometer, after 1 and 8000 scans, respectively, are shown on Figure 5.9. For the same gas mixture and RF pulse parameters, the NMR signal was about 1.5 times stronger when the new (*Dilas* laser of 0.2 nm linewidth was used, as compared to the old configuration with the *Coherent* laser (2 nm linewidth, 45 Watt). This result was further improved by a careful choice of operating temperature and the partial pressures of gases.

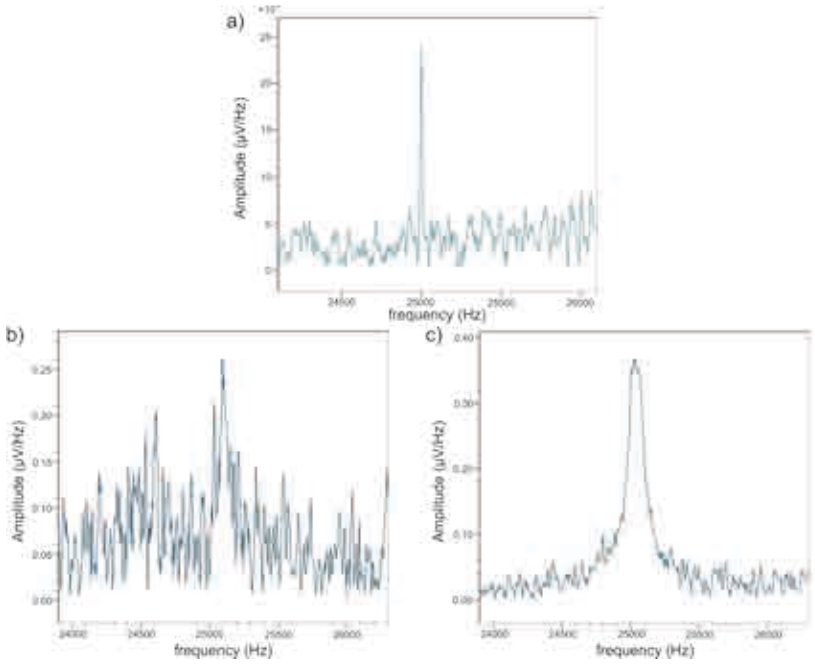

Figure 5.9: ^{129}Xe polarization calibration: (a) reference water NMR spectrum at 0.59 mT after 8000 averages (90° pulselength 0.55 ms, 3 V amplitude) and b) HP ^{129}Xe NMR spectrum from the SEOP cell containing 2% ^{129}Xe, 20% N_2 and 78% ^{4}He, acquired at 2.1 mT (a single scan, 90° pulse length 2 ms, 3 V amplitude) and (c) HP ^{129}Xe NMR spectrum for the same gas mixture and RF pulse parameters, but using the (*Dilas*laser diode.

5.4 Spin-exchange and spin-destruction calculations

Designing a SEOP polarizer is a complex task which requires some trade-offs to be made in many factors that affect the spin-exchange γ_{SE} and spin-destruction Γ_{SD} rates. Theoretical calculations of these parameters will be compared with their experimental values.. In the described polarizer a large $\sim$ 6 L SEOP cell was filled with the mixture of ^{129}Xe, N_2 and ^{4}He at different gas ratios up to 1 bar of total pressure and at temperatures ranging from 100 to 150°C. Calculations were done with Equations 2.17, 2.18, 2.13 and 2.14 (defined in Section 2.4). The binary term γ_{SE}^{BC} in Equation 2.17 is gas independent and the value for spin-exchange binary cross section equals $\kappa_{SE}^{BC} = 2.17 \times 10^{-16}$ cm^3/s [19], while the van der Waals contribution must be calculated for a given gas ratio using Equation 2.18. The density of rubidium was determined from the Kilian formula [97]. The gas densities as well as the spin-exchange and spin-destruction rates calculated for this experimental setup are shown in Table 5.3. The theoretical calculation suggested that spin-exchange is more efficient for lower xenon density (here 2%) and the optimal temperature for the chosen xenon density does not depend on the N_2:^{4}He ratio.

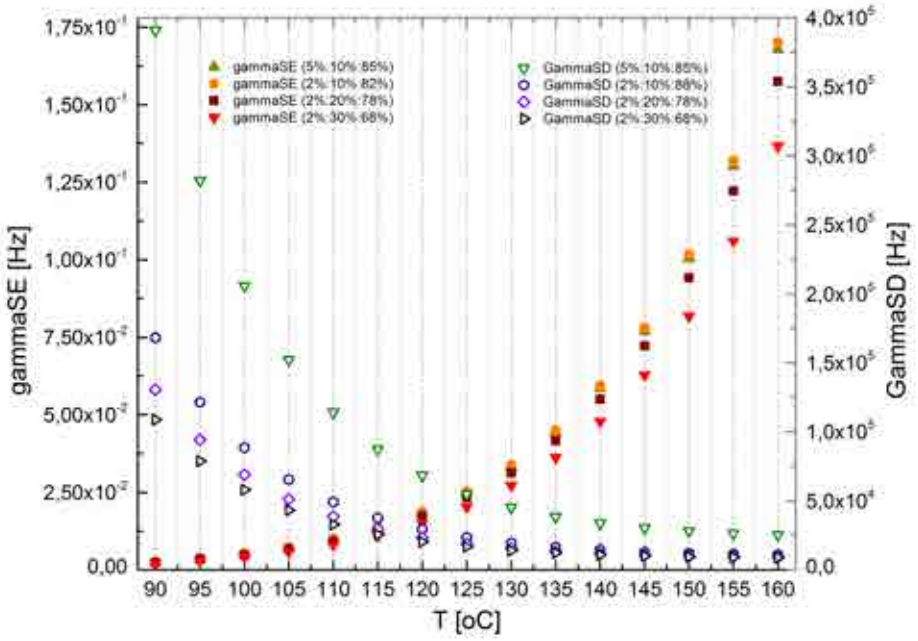

Figure 5.10: Theoretical calculation of spin-exchange γ_{SE} and spin-destruction Γ_{SD} rates as a function of temperature, for different gas densities used in the SEOP mixture at the total pressure of 1 bar .

Gas ratio ^{129}Xe : N_2 : ^{3}He [%]	Temp [°C]	Gas densities of ^{129}Xe, N_2, ^{4}He [cm^{-3}]	γ_{SE} [s^{-1}]	Γ_{SD} [s^{-1}]
5 : 10 : 85	150	8.90×10^{17}, 3.40×10^{18}, 1.48×10^{19}	1.23×10^{-1}	3.06×10^{4}
5 : 10 : 85	140	9.12×10^{17}, 3.48×10^{18}, 1.51×10^{19}	7.17×10^{-2}	3.01×10^{4}
5 : 10 : 85	130	9.35×10^{17}, 3.40×10^{14}, 1.55×10^{19}	4.07×10^{-2}	2.97×10^{4}
5 : 10 : 85	120	9.58×10^{17}, 3.66×10^{14}, 1.59×10^{19}	2.24×10^{-2}	2.93×10^{4}
5 : 10 : 85	110	9.83×10^{17}, 3.75×10^{14}, 1.63×10^{19}	1.20×10^{-2}	2.90×10^{4}
2 : 10 : 88	150	3.77×10^{17}, 4.20×10^{14}, 1.48×10^{19}	1.33×10^{-1}	1.34×10^{4}
2 : 10 : 88	140	3.86×10^{17}, 4.31×10^{14}, 1.52×10^{19}	7.76×10^{-2}	1.32×10^{4}
2 : 10 : 88	130	3.95×10^{17}, 4.41×10^{14}, 1.56×10^{19}	4.40×10^{-2}	1.31×10^{4}
2 : 10 : 88	120	4.05×10^{17}, 4.52×10^{14}, 1.60×10^{19}	2.43×10^{-2}	1.30×10^{4}
2 : 10 : 88	110	4.16×10^{17}, 4.64×10^{14}, 1.64×10^{19}	1.30×10^{-2}	1.29×10^{4}
2 : 20 : 78	150	3.22×10^{17}, 6.86×10^{14}, 1.34×10^{19}	1.46×10^{-1}	1.20×10^{4}
2 : 20 : 78	140	3.30×10^{17}, 7.03×10^{14}, 1.37×10^{19}	8.50×10^{-2}	1.18×10^{4}
2 : 20 : 78	130	3.38×10^{17}, 7.20×10^{14}, 1.40×10^{19}	4.82×10^{-2}	1.17×10^{4}
2 : 20 : 78	120	3.47×10^{17}, 7.39×10^{14}, 1.44×10^{19}	2.66×10^{-2}	1.17×10^{4}
2 : 20 : 78	110	3.56×10^{17}, 7.58×10^{14}, 1.47×10^{19}	1.42×10^{-2}	1.16×10^{4}
2 : 30 : 68	150	3.56×10^{17}, 1.03×10^{15}, 1.20×10^{19}	1.58×10^{-1}	1.37×10^{4}
2 : 30 : 68	140	3.65×10^{17}, 1.05×10^{15}, 1.23×10^{19}	9.19×10^{-2}	1.36×10^{4}
2 : 30 : 68	130	3.74×10^{17}, 1.08×10^{15}, 1.26×10^{19}	5.21×10^{-2}	1.36×10^{4}
2 : 30 : 68	120	3.84×10^{17}, 1.11×10^{15}, 1.29×10^{19}	2.87×10^{-2}	1.35×10^{4}
2 : 30 : 68	110	3.93×10^{17}, 1.14×10^{15}, 1.32×10^{19}	1.53×10^{-2}	1.35×10^{4}

Table 5.3: Theoretical calculation of spin-exchange γ_{SE} and spin-destruction Γ_{SD} rates for different gas densities used in SEOP mixture at 1 standard atmosphere pressure. Values are calculated with the ideal gas equation of state for xenon and helium and the van der Waals equation is an equation of state for nitrogen.

5.5 The results of ^{129}Xe polarization in the SEOP cell

The application of the new laser characterized by a narrow output spectrum led to higher efficiency of the SEOP process, hence to the stronger NMR signal measured. This allowed for more accurate determination of physical parameters and better optimization of the experimental setup. A simplified scheme of location of sensors that were used for the gas pressure, NMR signal, absorption, and oil temperature measurements is shown on Figure 5.11.

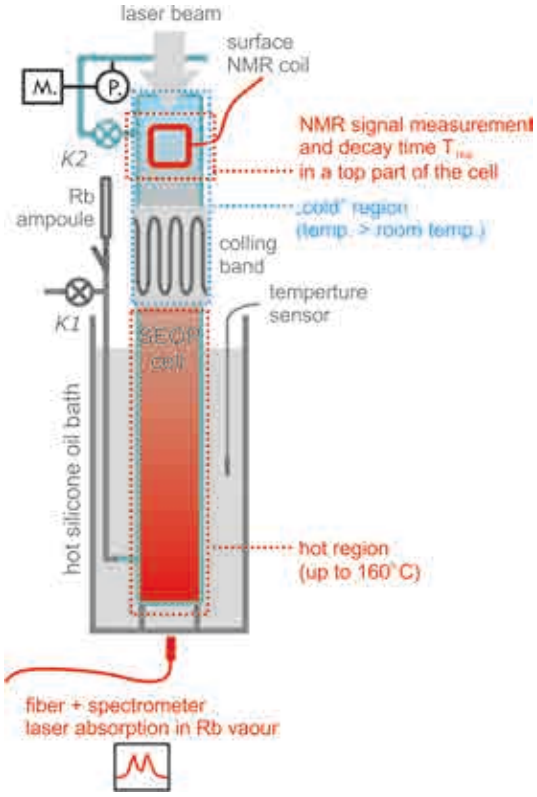

Figure 5.11: Simplified diagram of location of sensors used for measurement of gas pressure (P – membrane pressure gauge, M – microcontroller), NMR signal (NMR coil connected to the Aurora spectrometer), absorption (*Ocean Optics*) and oil temperature (Optical temperature sensor). NMR signal and T_{1top} measurements are performed in the top part of the SEOP cell, above the room temperature.

NMR signal dependence on the SEOP cell temperature for different gas ratios

The SEOP cell optimal temperature (established by the silicone oil temperature) depends on the gas mixture ratio. The oil was heated from 85 to 165°C and the NMR signal was measured by the low frequency *Aurora* spectrometer. The total pressure inside the SEOP cell was maintained at around 1 bar. The results presented on Figure 5.12 show that the highest NMR signal is obtained at about 140°C for 20 mbars of xenon. For higher content of xenon ($\sim$ 5% in the mixture) the optimal temperature decreases to about 135°C. Adding xenon up to 20 mbar moves optimal temperature to values of about 140°C. Varying the partial pressure of nitrogen does not change this temperature for a given content of xenon in SEOP cell, but changes the value of polarization. The measurement was done in the presence of laser light (FWHM 0.2 nm, 795 nm, 30 W) and points were collected when polarization reached equilibrium (for a given oil temp.)

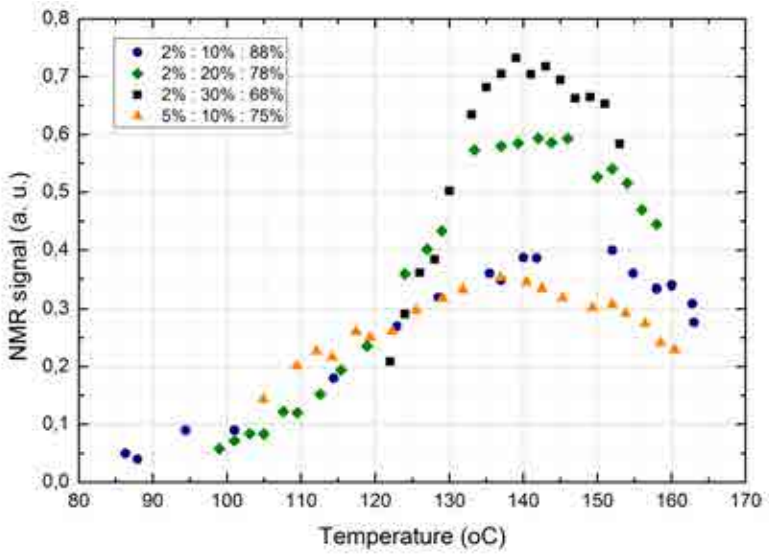

Figure 5.12: ^{129}Xe NMR signal amplitude as a function of the SEOP cell temperature for different gas mixture ratios of ^{129}Xe : N_2 : ^{4}He = 2 % :10 % : 88 % (blue), 2 % : 20 % : 78 % (green), 2 % : 30 % : 68 % (black) and 5 % :10 % : 85 % (orange). Below 120°C there was no difference in NMR signal for all ratios.

Polarization build-up and T_1 in the SEOP cell

The rubidium polarization reaches steady state after a few seconds, while the xenon polarization process takes much longer and can be monitored. The laser was switched on and the polarization build-up time was measured. When the steady state was achieved, then the laser was switched off and the T_1 decay was monitored. The polarization build-up and $T_{1,top}$ decay curves are presented in Figure 5.13a. The build-up curves were fit to:

$$y(t) = A(1 - e^{-Bt}), \tag{5.8}$$

where $t \equiv t_{build-up}$ is the build-up time and

$$A = \frac{\langle P_{Rb} \rangle \gamma_{SE}}{\gamma_{SE} + \Gamma}, \quad B = \gamma_{SE} + \Gamma. \tag{5.9}$$

The build-up time is shorter than 4 minutes and the plateau was reached in about 15 minutes. After 30 minutes the laser was switched off and the decay time $T_{1,top}$ was measured in the hot SEOP cell (temperature $> 40°$C). The decay curves were fit to the following equation:

$$y(t) = Ae^{-\frac{t}{T}} + y_0, \tag{5.10}$$

where $T \equiv T_{1,top}$ is the decay time in the presence of dense rubidium vapor. The calculated $T_{1,top}$ values for given physical conditions are listed in Table 5.4 and theyare smaller than 4 minutes. Such a short relaxation time is expected due to spin-destruction collisions with non-polarized alkali atoms.

The determined optimal temperature and the NMR signal dependence on the gas content ratio (mostly xenon partial pressure) were reproducible. Similarly, adding nitrogen at fixed xenon partial pressure produced higher NMR signals (see Fig. 5.13b).

Gas ratio ^{129}Xe:N_2:^{3}He [%]	Temp. [°C]	Total pressure [mbar]	$S_{Xe,max}$ [a.u.]	$t_{build-up}$ [min]	T_1 in *hot cell* [min]	P_{Xe} [%]
2 : 10 : 88	155	1013	0.33 ± 0.01	2.00 ± 0.16	1.36 ± 0.23	0.91 ± 0.22
2 : 20 : 78	145	1008	0.42 ± 0.02	2.14 ± 0.16	1.84 ± 0.19	1.13 ± 0.29
2 : 20 : 78	142	1022	0.48 ± 0.01	2.29 ± 0.11	2.31 ± 0.37	1.27 ± 0.29
2 : 20 : 78	140	1006	0.34 ± 0.04	1.29 ± 0.21	1.22 ± 0.41	0.91 ± 0.30
2 : 20 : 78	134	1014	0.35 ± 0.02	2.58 ± 0.21	2.27 ± 0.46	0.92 ± 0.24
2 : 20 : 78	115	970	0.23 ± 0.14	4.08 ± 0.57	3.06 ± 0.38	0.60 ± 0.49
2 : 30 : 68	143	1030	0.55 ± 0.02	2.62 ± 0.18	3.37 ± 0.65	1.45 ± 0.35
2 : 30 : 68	135	1026	0.58 ± 0.02	3.53 ± 0.22	3.16 ± 0.26	1.50 ± 0.37

Table 5.4: Values of maximum NMR signal with corresponding polarization values, signal build-up time $t_{build-up}$ and decay time T_1 in hot SEOP cell, for three gas ratios: 2 : 10 : 88 %, 2 : 20 : 78 % and 2 : 30 : 68 % at different oil oven temperatures.

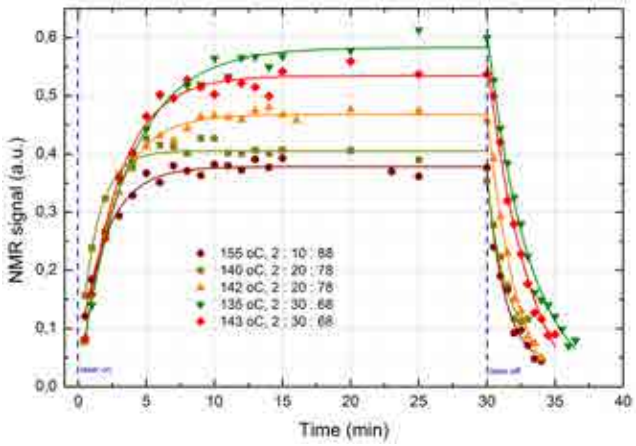

(a)

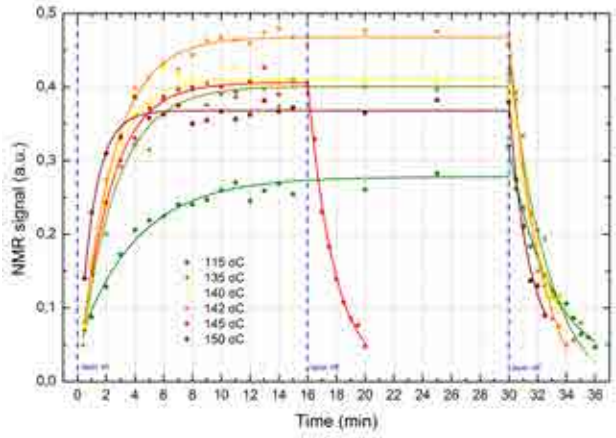

(b)

Figure 5.13: Polarization build-up and decay after switching on and off the laser, respectively for three gas ratios: 2 : 10 : 88 % (dark red), 2 : 20 : 78 % (yellow, orange) and 2 : 30 : 68 % (red, green) at different oil oven temperatures: 135 – 155°C (a) and for gas ratio 2 : 20 : 78 % at different oil oven temperatures: 115 – 150°C (b). Calculated parameters are presented in Table 5.4.

Polarization calculations

Using Equations presented in Section 5.3 one can calculate the absolute polarization of xenon by comparing its NMR signal with the water signal, which is of the order of 3.5×10^{-3}. As it is shown in Table 5.4, the polarization is of the order of 1%, which is rather low comparing to other systems known from literature. However, it is difficult to find a design operating in similar physical conditions (pressure of 1 bar, large SEOP cell and 16 Watt laser power). The polarizer designed by the Hersman group [26] produces polarization that exceeds 64 % by using 1kW of laser power. Therefore increasing the applied laser power would be the first step in improving the efficiency of the present design. Moreover, the cell

illumination should be refined. In the present optical system the laser beam size does not match the size of the optical window, causing about 2/3 of the pumping cell to be *dark*.The collisions between polarized and non-polarized rubidium atoms reduce the efficiency of the SEOP process due to spin destruction effect. of The optimal set of parameters that was obtained up to now refers to the experiment with the closed SEOP cell. It is not necessarily optimal in the continuous flow regime, which is the ultimate goal of the designed polarizer. It is necessary to determine how the xenon polarization depends on the gas flow rate. Such studies are planned in the near future.

5.6 Considerations about rubidium handling

The SEOP process requires an alkali-metal vapor to be used for optical pumping. Following most designs, rubidium was chosen for the designed polarizer, because it is available and easy to handle. However, there is a problem that was reprted in all SEOP polarizers. During operation, the internal surface of the glass cell is gradually covered by rubidium. Since small cells are more susceptible to this effect, they cannot be used for longer than about one month. Our large SEOP cell could operate for several months without replacement, provided the rubidium was handled with special care. First of all, a 5g ampoule of metallic rubidium was inserted in a vertical position, preventing it from pouring out along the cell walls during warming. It was noticed that a rubidium layer formed on the metal-glass connection, reducing the rubidium amount inside the cell to less than 5 g. Then a cooler band was used to remove rubidium from the upper part of the cell. Finally, if there was any rubidium remaining at the top of the cell, one could get rid of it by a simple cleaning process (see Fig. 5.14a).

Occasionally, another problem occurs during the experiment, due to the air leak. In the presence of oxygen the RbO_2 is formed and the cell becomes useless (see Fig. 5.14b). The presence of oxygen in the cell causes a gradual decrease of the NMR signal, making further measurements impossible. In such a case it is necessary to replace the cell and repeat the rubidium filling process, which takes maximum two days.

Such accident happened due to a loose valve that fell out at high temperature. All glass valves are sealed with a high vacuum grease (Apiezon H Grease, *Apiezon M&I Materials Limited*), which remains hard up to 240°C. Before opening or closing the valve an air blower is used to heat it above that temperature making the grease softer, and this way a strong force that could break the glass is avoided. However, the valves that are located in the cryogenic unit operate at low temperature and must be sealed with another grease (high vacuum grease working between -273° and 30°C, Apiezon N Grease, *Apiezon M&I Materials Limited*). One of these valves was not protected by additional fasteners and a part of it fell out when the temperature reached 160°C. This was noticed immediately by the decrease of the NMR signal.

Another set of glass tubes for higher pressure operation is planned to be used in the near future. They have special valves that can sustain more than 2 bars of pressure (10 mm, high performance stopcocks, *Rotaflo*) and do not need any grease.

5.7 Approach to SEOP experiment

There is a large number of adjustable parameters that affect the operation of the SEOP polarizer. A mind map can be constructed which illustrates most relevant physical pro-

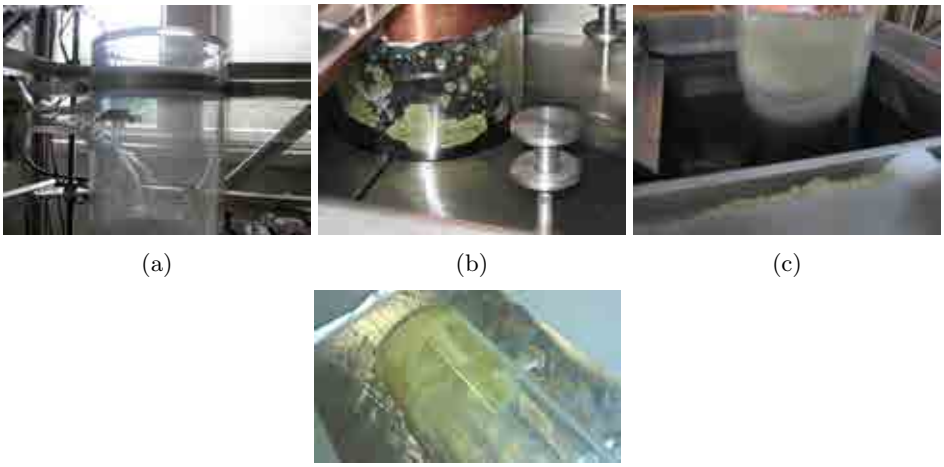

(a) (b) (c)

(d)

Figure 5.14: The rubidium inside the SEOP cell. During operation metallic rubidium covers internal surface of the glass cell (a). A greenish layer of the rubidium oxide can be noticed in (b-d) following the air leakage.

cesses occurring during the SEOP and their relationship (Fig. 5.15). It is clear that a compromise must be made between the level of polarization, amount of HP ^{129}Xe gas, and the production time. The specific application of the designed polarizer is an important factor in choosing the optimum combination of experimental conditions. Since the designed polarizer is intended for medical imaging of human lungs, a large amount of HP ^{129}Xe is required. It is believed that the described SEOP polarizer will satisfy these requirements after some further improvements mentioned in this thesis, which are in the advanced stage of implementation and should increase its throughput.

Figure 5.15: Summary of favorable and unwanted processes during the SEOP experiment for polarizers operating at$\sim$ 1 bar pressure, low ^{129}Xe concentration and large volume SEOP cell.

6

Discussion and further developments

6.1 Results comparision among other SEOP experiments

There are only few ^{129}Xe SEOP polarizers worldwide. Most of them operate at higher pressure of 2 bars or more, using a small volume SEOP cell of $\sim 100 - 500$ cm^3. According to my knowledge, only two designs use a large SEOP cell operating at atmospheric pressure: one in the Hershmans grup [26], and the one presented in this thesis.

The first results reported in literature showed that the maximum ^{129}Xe polarization did not exceed 10 % [98]. It was due to the unfavorable combination of low laser power, broad output spectrum, not uniform light distribution in the cell, and the limited knowledge of relaxation processes at that time. Much higher polarization of 65% reported by [99] was achieved with the 210 W laser characterized by 1.6 nm FWHM linewidth, operating at 4.6 bars for efficient pressure broadening. A significant progress was made when new, high power and narrow output spectrum lasers were developed. Using a diode stack (90 W, 1.5 nm FWHM) it was possible to produce 0.3 l of HP ^{129}Xe having 64% polarization in one hour [85]. When the laser linewidth was narrowed to 0.3 nm FWHM at 60 W, the polarization increased to 84%.

Polarization [%]	Laser power and FWHM [W], [nm]	Pressure [$mbar$]	Cell [cm^3]	Oven [°C]	Ref.
65	210, 1.6	4600	250	140	Zook et al. [99]
84	60, 0.3	1000			Zhu et al. [85]
10	27, 0.27	1300	75	100	Nikolaou et al.[86]
90	200, 0.27	1300	500		Nikolaou et al.[100]
64	90, 1.5	1300		160	Ruset el al. [26]

Table 6.1: Values of ^{129}Xe polarization achieved in different SEOP experiments.

Nikolaou et al. [86] used volume holographic grating to narrow the laser linewidth to 0.27 nm, which led to 10 % polarization at 27 W. Applying the 200 W laser in the same setup

increased the polarization to 90% [100]. The principal parameters and obtained results in some ^{129}Xe SEOP polarizers are summarized in Table 6.1.

An interesting observation was made that a small detuning from the D_1 rubidium line resulted in higher polarization, and this effect was density dependent [101]. However, this occurs at the cost of some reduction of laser power, detuned from its nominal frequency. This effect is also observed in our laser diode.

In our polarizer 16 W of laser power is used, as measured on the optical window of the SEOP cell. It will be increased in the near future, improving the spin-exchange efficiency to some extent [102]. Some modifications of the beam design and the cell shape are also planned for better cell illumination, which will increase the spin-exchange regardless of the laser power.

6.2 Discussion

The application of HP ^{129}Xe gas in medical human lung imaging and materials science was the motivation for designing and constructing the ^{129}Xe SEOP polarizer. Operating at about 1 bar and low ^{129}Xe concentration of 2 – 5% it produced about 0.12 – 0.30 liters of gas polarized to about 1 % in less than 5 minutes. Further developments of the ^{129}Xe SEOP polarizer will be directed towards achieving higher xenon polarization. The major limiting factor in the present design is the laser light absorption in rubidium vapor. It can be increased in two ways: by improving the laser performance or by elevating the pressure. In our case narrowing the linewidth of high power laser was combined with maintaining low total pressure in the SEOP cell. During the SEOP process, the creation of van der Waals molecules is essential for efficient polarization transfer from rubidium to ^{129}Xe. This requires low or normal pressure [22]. Faster spin-exchange and slower relaxation rates can be obtained at low pressure. Impressive volume polarization levels were reported at 1.3 low pressure [26], which is a promising observation. Although the absorption efficiency can be improved by adding buffer gases, the total pressure in the cell is then increased, which the opposite to our initial goal. A new set of glass components with the stopcock valves that is designed for higher pressure operation is already prepared for implementation. When the previous laser with the 2.0 nm linewidth was replaced by the new one with the linewidth narrowed to 0.2 nm, the polarization level increased by the order of magnitude. Further improvement will be made by using a new SEOP cell, with a smaller optical window that matches the laser beam diameter. An increase of the laser power is also planned.

Although the application of large volume SEOP cell was successfully tested by Hersman et al. [26], it is not a standard solution in the SEOP polarizers. Usually a small cylindrical cell of about 2 liters volume is used [100], in which an elevated pressure of 2 bars or more is maintained. Our motivation to use a larger cell was to produce sufficient amount of HP ^{129}Xe in one cycle, which is important for medical applications. There are several advantages of using a large volume SEOP cell. First of all, an increased volume of rubidium vapor absorbing the laser light improves the optical pumping efficiency. Furthermore, a longer residence time of ^{129}Xe in the longer cell makes the spin-exchange more efficient and allows the polarization to saturate. Finally, a large cell has smaller volume-to-surface ratio, reducing the wall relaxation.

Low pressure SEOP polarizers use long cells to increase the total laser light absorption. It adds another complication to the proper operation, because the SEOP cell needs to be uniformly filled with rubidium vapor at satisfying level. This was successfully resolved in our setup. Some problems may occur due to an inhomogeneous temperature distribution

along the cell caused by the laser absorption, and due to back reflection of the laser light from the alkali metal layer. A careful optical setup is necessary to make sure that the laser beam illuminates the whole volume and provides an adequate optical penetration of the SEOP cell even at higher temperatures. On the other hand, small SEOP cells need to be periodically replaced, because rubidium quickly covers their internal surfaces.

Generally speaking, a considerable progress has been made in recent years both in understanding the physical processes taking place during the SEOP process, and in improving its performance. However, several important problems remain to be solved.

One of the problems is low ^{129}Xe concentration, which needs to be maintained in the SEOP cell. Otherwise non-spin conserving Rb-^{129}Xe collisions would reduce the achievable rubidium electron spin polarization. Moreover, xenon dimers appearing at higher xenon densities would contribute to nuclear relaxation [47]. The spin-rotation interaction occurring in the short-lived ^{129}Xe-^{129}Xe complex species is believed to be the responsible relaxation mechanism in gaseous ^{129}Xe [52]. In this regard, a new effect has been recently discovered by Whiting et al. [88], namely an anomalous ^{129}Xe polarization dependence on the xenon partial pressure in the SEOP cell. The polarization was unusually low at small xenon partial pressure, achieved maximum at 400 mbar, and stayed surprisingly high up to 1300 mbar. The origin of this effect is not fully understood yet, and additional experiments and simulations are in progress [88].

Up to now, the operation of the SEOP polarizer in the batch mode was discussed, in which a closed SEOP cell is periodically filled with the fresh gas mixture. After completing the polarization process, the gas mixture is cooled to remove buffer gases and rubidium vapor and put in the cryogenic storage cell. The operation of the SEOP polarizer in the continuous flow regime is much more demanding and requires a careful adjustment of all critical parameters. Some polarization is lost in such setup. Therefore it is important to monitor the flow constantly during on-line medical trials, using NMR. Since a fresh xenon is continuously flowing through the RF coil, the flipping angle of the exciting RF pulse can be longer than the usual 10°, boosting the NMR signal.The consecutive cooling and storing of hyperpolarized xenon is done in the same way as in the batch mode.

For successful implementation of experiments with HP ^{129}Xe, the extraction of xenon from the polarizer, storage, and delivery should be carried out at the minimum loss of polarization. The cryogenic storage system dedicated for both batch and continuous flow modes of operation was prepared. The frozen xenon placed in the dewar filled with liquid nitrogen is located inside the solenoid, producing the magnetic field of about 200 Gauss, to reduce the relaxation effects during the phase changes. The whole unit can be transported to hospital using a portable power supply for maintaining the magnetic field. After thawing a gas portion into a special bag (*Tedlar Bag®, Sigma Aldrich*), it can be inhaled by the patient.

The medical facility in the John Paul II hospital in Cracow is already prepared to perform human lung imaging using hyperpolarized noble gases. The 1.5 T Siemens Sonata Magnetic Resonance medical scanner is equipped with two additional RF coils (GE HDxt 1.5 T MR system, *Rapid Biomedical*) that are tuned to ^{3}He and ^{129}Xe resonance frequencies. The first successful pre-clinical tests were performed with hyperpolarized ^{3}He gas [103]. More details are given in the *Appendix B*.

6.3 Further developments

Last but not least, one of the final steps of each HP gas usage can be an experiment performed in low magnetic fields. Not only low cost and no need for maintaining superconducting magnets simplify experiments, but also the benefits of low-field MR imaging are potentially numerous [104, 105, 106, 107].

A home-build low-field (of only 0.088 T magnetic field) scanner was constructed years ago in Faculty of Physic (Jagiellonian University) with co-operation with Faculty of Physics and Nuclear Technology (University of Mining and Metallurgy in Cracow) within PHIL project[1].

The scanner consists of Nd-Fe-B magnet (two pole plates) assembled in a special frame so that all repulsive and pulling forces between elements in the magnet structure were controlled. The homogeneity in working area was about 100 ppm, and then 50 ppm after implementation of passive shimming [108]. The detailed description of the low-field scanner, its initial adaptation, shimming procedure and test of series of fast MRI sequences for the purpose of animal lungs imaging and tests of current limitations of the system in terms of achievable SNR and resolution are presented in [109] and in listed PhD Theses [110, 111, 112]. The RF coils are driven by power amplifier (*Dressler*) via a matching circuit and a passive duplexer. A low noise preamplifier (AU-1583, *MITEQ*) is used for amplify the signal induced in the RF coil.

Tuning the scanner to ^{129}Xe frequency[2] is a mandatory step for imaging. The console was equipped with a home-built frequency converter, which makes it possible to perform the MR experiments at either ^{1}H, ^{3}He and ^{129}Xe. The procedure of frequency tuning of this low-field scanner is presented in [112].The RF coil is a transmitting-receiving coil built within project presented here [113]. It is a combination of short solenoid with pairs of circular coil at the ends of the coil. Set of tuning and matching capacitors are located after the coil in an aluminum box (*matching-tuning box*), which can be easily removed and replaced with different set of capacitors (Non-magnetic Trimmer Capacitors, *Voltronicscorp*). This a handy way to change between ^{1}H, ^{3}He and ^{129}Xe frequencies. Two other modules, which were replaced are a *mixer* and *RF unit*. The mixer mixes (sum and substract) ^{3}He frequency (2.84 MHz) with values settled with generator (6.57 MHz for ^{1}H and 3.87 MHz for ^{129}Xe). Next, values are filtered into 3.73 MHz and 1.03 MHz for ^{1}H and ^{129}Xe, respectively.

[1] The European PHIL project – Polarized Helium to Image the Lung – a European consortium to study emphysema and other lung diseases with HP ^{3}He, see report on: *http://arxiv.org/pdf/physics/0501127.pdf*

[2] A great role of Dr Zbigniew Olejniczak responsible for calculations and implementation new electronics for tuning to ^{129}Xe resonance frequency

7

Perspectives

Starting from the first HP ^{3}He MR image of human lungs [114], most of medical studies was performed using this contrast agent. The heterogeneous distribution of ventilation in asthma [115], chronic obstructive pulmonary disease [116], and cystic fibrosis [117] were investigated. The introduction of HP ^{129}Xe opens new possibilities in MRI of human lungs, apart from anatomic, ventilation, and perfusion studies. The alveolar surface area, septal thickness and vascular transit times can be measured. The Apparent Diffusion Coefficient (ADC) maps can be also obtained.

Initial tests to evaluate the safety and tolerance of inhaling HP ^{129}Xe were made [15]. Although xenon has strong anesthetic properties, no side effects were observed during the imaging protocols. Healthy subjects as well as patients with mild or moderate COPD tolerated a portion of HP ^{129}Xe quite well. First ADC maps using ^{129}Xe were also measured [118]. Depending on the stage of disease, the air trapping and hyperinflation in airways can modify the ADC maps to different extent, and can be quantitatively measured by counting the number of defects per slice. Sequences using diffusion-weighted techniques can determine some microstructural changes in the emphysematous lung [119]. For example, COPD can be represented by severe types of abnormalities such as emphysema, bronchitis, and bronchiectasis and their nonspecific manner is problematic in terms of distinguishing those types. This causes substantial overlap in diagnosis.

Proton MR diagnostic imaging of human lungs was always challenging, due to low proton density [120]. Other diagnostic methods either use ionizing radiation (CT, PET, SPECT), or provide very limited information (spirometry). According to preliminary results, HP ^{129}Xe MRI will provide new and quantitative information about gas delivery, exchange, and transport in human lungs. The method shows considerable potential of extending our knowledge of lung diseases and improving their diagnosis. Moreover, the method is sensitive enough to detect the lung cancer in a very early stage of development.

HyperCEST is a new technique involving HP ^{129}Xe that was developed by the Alex Pines group [121]. By encapsulating HP ^{129}Xe in *cryptophane* [122], it makes possible to detect the tissue biomarkers that are of special interest in biological systems. CEST is the NMR chemical shift saturation transfer technique, which increases the signal from the regions where this *NMR biosensor*is located. This allows to detect the target molecules

in a non-invasive way. Recently it was reported that encapsulated HP ^{129}Xe can detect nanomoles of interesting analytes [123] characterized by 65 ppm chemical shift, depending on the type of cryptophane (comparing to 190-230 ppm in solutions) [124].

The implementation of any MRI or NMR study with hyperpolarized ^{129}Xe requires an access to the HP gas source. It is believed that the growing demand will stimulate further progress in the SEOP polarizers design, improving their performance and providing large amounts of hyperpolarized gas for various applications.

The SEOP polarizer presented in this work is an initial step towards a large-scale production of HP ^{129}Xe for medical studies, but also can be used for material studies.

8

Appendix A – Design and characterization of old diode laser system with optical setup

8.1 Design

A two diode laser array (Scientific DUO FAP System, *Coherent*) of 60 W maximum power was initially used in the SEOP polarizer. Each diode operating at 30 A had its own current and temperature control unit and was characterized by 2 nm spectral width. The laser outputs were coupled to optical fibers and combined by the collimator.

Two different optical arrangements were tested, but only the second one (Fig. 8.1) was eventually used for the reason that will be explained later. Two non-polarized beams from the fiber bundle go into the collimator and then enter the beam expander, consisting of 100 mm dispersing and 500 mm focusing lenses, separated by 400 mm. The reason for using such a homemade beam expander was to reduce the power dissipation in the polarizing optics which would be caused by two closely separated ($(2 \times 800\ \mu m)$ laser beams. A dielectric mirror (M_1)(BK7, SF $\lambda/10$ at 633 nm, coated $HR > 99.5\%$ at 795 nm for 45^o, *Eksma Optics*) reflected the expanded beams to keep it within the optical table of limited size.

Two expanded (50 mm each) and partially overlapping beams are then divided by the polarizing beam splitting cube (PBS, BK7, *Eksma Optics*). The reflected linearly s-polarized[1] beams pass a multi order quarter-wave plate ($\lambda/4$, BK7, quartz, retardation $\lambda/4$ at 795 nm, *Eksma Optics*) that produces the circular polarization and are directed into the SEOP cell by three mirrors M_2, M_3, and M_4.

The transmitted p-polarized[2] beams pass the half-wave plate, which rotates their linear polarization to the same orientation as that of the reflected ones. Then they enter the second PBS which improve their linear p-polarization, are converted to circularly polarized beams by the second quarter-wave plate, and directed into the SEOP cell by two mirrors M_5, and M_6.

[1] *s-polarization* refers to the polarization plane perpendicular to the polarization axis of the PBS
[2] *p-polarization* refers to the polarization plane parallel to the polarization axis of the PBS

Consequently, four, almost overlapping laser beams are directed down by two additional mirrors towards the optical window of the SEOP cell and cross at about its center. Since the optical window is not covered by the antireflection coating, some power loss occurs. All together, the effective laser power of 46 W is measured at the optical window of the SEOP cell due to power losses in the optical setup. The details of laser power measurements and tuning are given in the next Section 5.1.

For safety reasons, the laser is enclosed in a large custom made box made of non-magnetic material, which is shown in Figure 4.9. The internal surfaces of the walls are painted with black graphite spray. The laser power was measured with the (*Ophir*) power meter. Initially, the measurements were carried out with the (*collimator 1*), which belonged to the Scientific DUO FAP System, but was incompatible with two laser beams. An excessive power loss occurred due to small separation of laser beams. Therefore the *collimator 2* (High Power, 808nm, 50W, Gold-FAP-Laser-Diode-Collimator-Lens-SMA-Optic, *Coherent*) designed for two bundle fiber type was applied. However, although the power measured after the *collimator 2* was slightly higher, another problem occurred, because the two separate beams directed towards the beam expander (*Eskma Optics*) were not properly focused, which caused some power loss. The final arrangement included the the *collimator 1* and the home-made beam expander, which minimized the power loss (Fig. 8.2).

Additionally, a small radiator was applied to the *collimator 1* for heat dissipation.

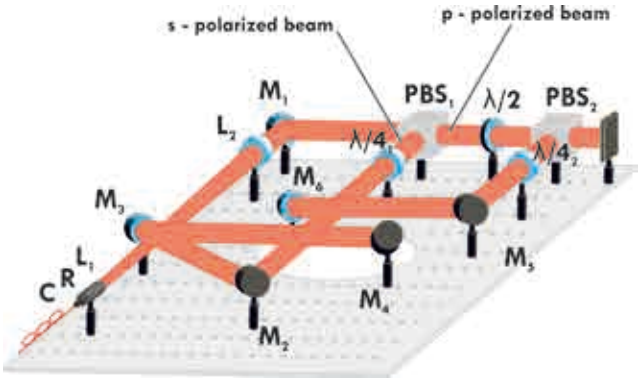

Figure 8.1: Schematic diagram of ^{129}Xe polarizer optical system a home-made beam-expander. PBS - polarizing beam splitter, $M_{1,3,5}$ - dielectric mirrors reflecting laser light mounted perpendicularly to optical table, $M_{4,6}$ - dielectric mirrors directing the laser light into the SEOP cell mounted at the 45^o angle to optical table, $\lambda/4$ - quarter-wave plate, $\lambda/2$ - half-wave plate, L_1 - dispersing lens, L_2 - focusing lens, C - collimator (*collimator 1* or *collimator 2*), R - radiator.

Figure 8.2: Optical system mounted at the top of the ^{129}Xe polarizer. It is enclosed in the box during operation for eye protection.

8.2 Laser power measurements

As it was described in the previous section, some modifications were necessary in the optical system in order to minimize the power losses. A series of measurements of the laser power was made with the (*Ophir*) laser power meter for a single diode (Fig. 8.3 for the *right* diode), at five different arrangements of the laser output:

- 1 - *collimator 1*
- 2 - *collimator 1* with single lens
- 3 - *collimator 1* with the telescope (*Eksma*)
- 4 - *collimator 1* with a home-made beam expander
- 5 - *collimator 2*

The measurement showed that the maximum power of 60 Watts could not be reached at the optical window of the SEOP cell. The highest power of 23.45 W was measured with the collimator only, but such arrangement was not acceptable. The power loss difference between the *collimator 1* and *collimator 2* was about 0.6 W. The addition of a single lens after the *collimator 1* caused some power loss. The home-built beam expander increased the output laser power by about 8 W.

The second condition for laser system design for SEOP (full illumination of the SEOP cell) imposed usage of the first original collimator. The second one designed to work with two bundle fiber type has two outputs for focusing two separate beams, but further arrangement was complicated. The final cell illumination was satisfactory at the expense of lower laser power, but with easier way to arrange optics.

Two separate laser diodes, each 30 Watt, were tuned to the D_1 rubidium line. For clearer view one of them is called *left* and another *right*, corresponding to the appearance of controls at the front panel. Each diode had to be tuned separately by setting its temperature.

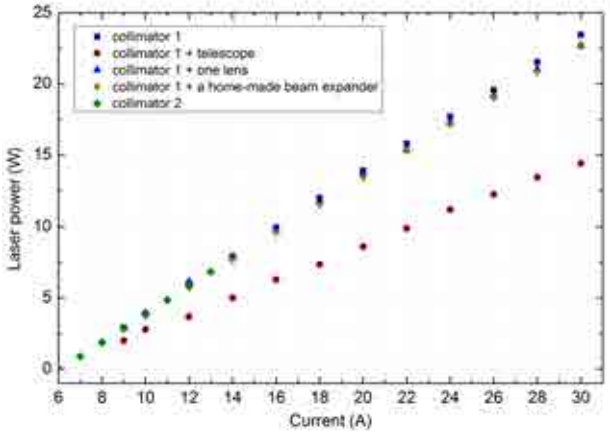

Figure 8.3: Laser power for different combinations of collimator and beam expander. The results are shown for the *right* diode.

Spectral light profiles of the laser in the SEOP cell additionally filled with 100 mbar of nitrogen are presented on Figure 8.4, as a function of the diode temperature . Nitrogen was necessary for pressure broadening of the D_1 rubidium line. The laser beam after passing through the SEOP cell was detected by the fiber equipped with the collimator, and transferred to a slit of the spectrometer (adapted from Carl Zeiss Jena monochromator). Its spectral resolution was better than 0.02 nm and to operate at the infrared range it required a CCD camera. The spectrometer was calibrated by measuring the reference lines D_1 and D_2 from a small rubidium cell with radio frequency discharge.

An absorption dip corresponding to the D_1 rubidium line can be clearly observed at a specific diode temperature (Figure 8.4), which is equal to 22°C and 18°C for the *right* and *left* diode (not shown), respectively.

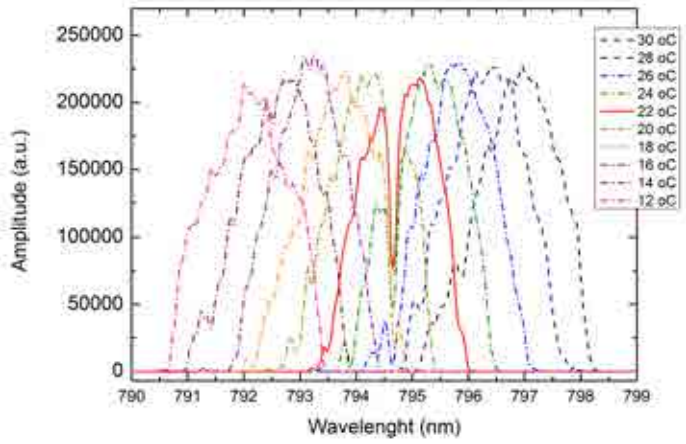

Figure 8.4: Laser diode bar temperature tuning with only *right* diode switched on in the presence of 100 mbar of nitrogen and rubidium vapor at 144°C. Matching diode bar temperature value for D_1 is 22°C for the *right* diode (red line).

8.3 Absorption profiles

After determining the optimum diode temperature, the effect of buffer gases was studied. Only a single, *right* diode was used, at the temperature of 22°C and the current of 30 A, providing the maximum laser power of 22.5 W. The buffer gases were added while the temperature of oil was increased to 150°C.

The absorption profiles are shown on Figure 8.5. They demonstrate the increased absorption of the incident laser light, resulting from the pressure broadening of the Rb D_1 resonance line that is caused by the buffer gases.

This laser system could not be re-designed to narrow its line width, due to the fiber module that was already fixed. Therefore a more efficient laser source was required in a long run. Still, the first successful ^{129}Xe polarization experiments were performed with this setup. The NMR signal measurements and some optimization of the polarizer will be described in the next section.

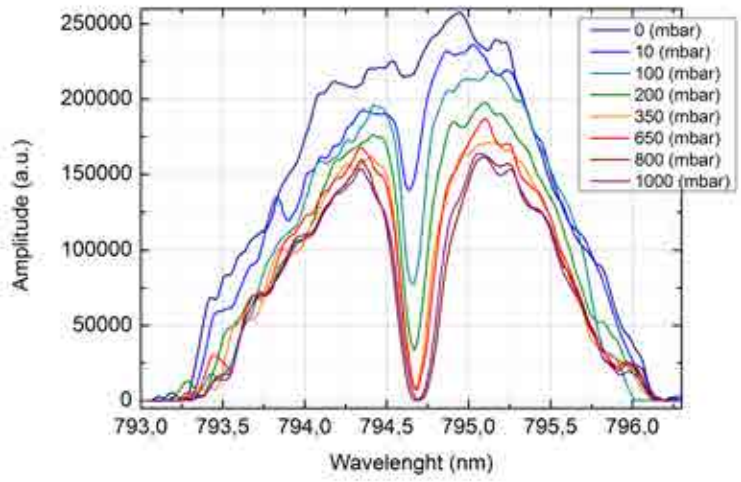

Figure 8.5: Rubidium absorption profiles in the presence of buffer gases: nitrogen and helium (only some profiles were presented for clearer view). After reaching 212 mbar of nitrogen, up to 614 mbar helium was added.

8.4 Polarization of ^{129}Xe in the SEOP achieved with *old* laser

The first NMR signal of polarized ^{129}Xe was measured inside the SEOP cell using a saddle RF coil that was mounted at the top of the SEOP cell, as it was shown on Figure 5.11.

Each experiment started with cleaning the gas distribution system and the SEOP cell with the turbo molecular pump. A vacuum of 10^{-7} mbar and 10^{-5} mbar was usually reached in the stainless steel unit and the glass system, respectively. The gas mixture was prepared manually, starting from ^{129}Xe and then adding N_2 and ^{4}He. These steps were carried out at room temperature. Otherwise the rubidium film would start covering the upper parts of the SEOP cell, especially in vacuum and at the temperature above the rubidium melting point. Before turning on the oil heating, the air ventilation was switched on to protect the optics from the oil vapor.

Then the temperature was increased to the desired value (140°, 150° and 160°), with water circulating in the cooler band. In order to stabilize the magnetic field, the power supplies driving the coils had to be switched on about half an hour before the experiment. The laser was turned on using the parameters determined previously. The illumination was monitored with the laser viewing card (NIR Detector Card, *Thorlabs*) to make sure the optical components did not move.

Polarization measurements in different conditions

The first results obtained with the *Coherent* laser diode and a small RF coil mounted at the top of the SEOP cell are shown in Table 8.1. Different temperatures and gas ratios were used, keeping the the total pressure just above 1 bar. The NMR signal for 5% of ^{129}Xe in the gas mixture was higher than for 2%, but further polarization values showed opposite

trend.

Content [%]			Temperature	Pressure	Build-up time	NMR signal
^{129}Xe	N_2	^4He	[°C]	[mbar]	[min]	[a.u]
2	20	78	140	1084	20.5	0.31
2	20	78	150	1107	9.2	0.29
2	20	78	160	1117	7.1	0.19
5	20	75	140	1077	8.8	0.41
5	20	75	150	1089	1.2	0.32
5	20	75	160	1109	9.7	0.21

Table 8.1: NMR signal measurement in different conditions in the presence of magnetic field $B_0 = 21$ Gauss and 45 Watts laser power. The NMR signal from mixture with higher ^{129}Xe content is stronger, but further calculated polarization is lower.

Content [%]			Temperature	Pressure	NMR signal
^{129}Xe	N_2	^4He	[°C]	[mbar]	[a.u.]
5.7	20	74.3	140	1070	0.40
5.7	20	74.3	160	1058	0.20
5*	20*	75*	140	1077	0.11
5*	20*	75*	160	1109	0.08

Table 8.2: NMR signal measurement in different conditions in the presence of magnetic field $B_0 = 21$ Gauss and 45 Watts laser power for clean and contaminated* cells (NMR signal was at the noise level).

The NMR spectra obtained at different experimental conditions after a single RF pulse are shown on Figure 8.6. A high level noise could be reduced by putting the entire system into Faraday cage. Polarization was calculated against water sample for all measurements (the method described in section 5.3). Consequently, the value of polarization was lower than that obtained with the new laser system and the difference was one order of magnitude lower.

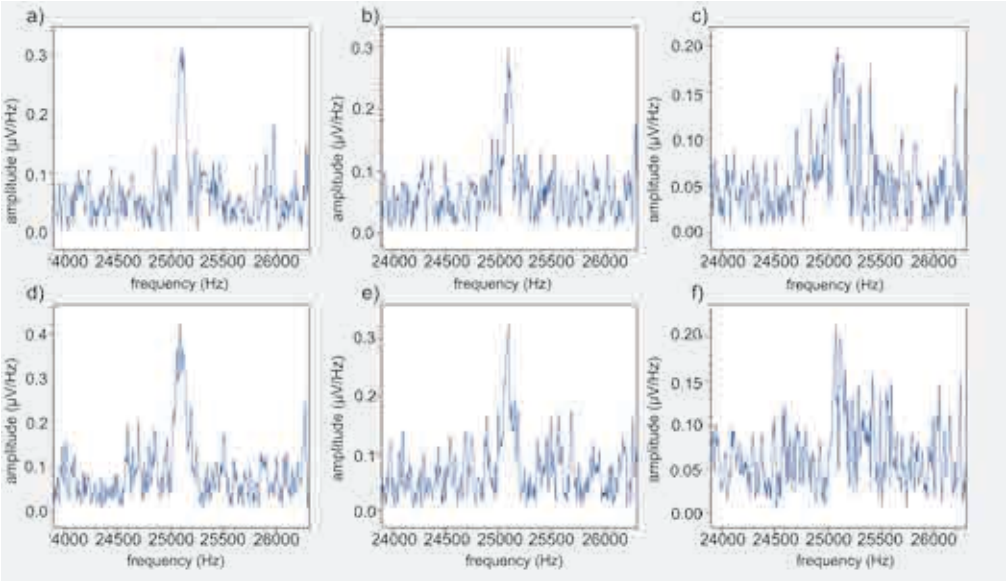

Figure 8.6: The NMR signals from HP ^{129}Xe after a single RF pulse at 2.1 mT measured by the Aurora spectrometer for 2% ^{129}Xe, 20% N_2, 78% ^{4} He (a – c) and 5% ^{129}Xe, 20% N_2, 75% ^{4}He and temperatures 140°C (a, d), 150°C (b, e) and 160°C (c, f). The signals were measured 20 minutes after the laser was turned on. The SEOP cell was filled with rubidium 4 months before.

Polarization build-up

In a closed SEOP cell and assuming a good filling factor of the RF coil, the dynamics of ^{129}Xe polarization can be described by the following phenomenological equation [88]:

$$P_{Xe}(t) = \langle P_{Rb} \rangle \cdot \left(\frac{\gamma_{SE}}{\gamma_{SE} + \Gamma_{SD}} \right) \cdot (1 - e^{-(\gamma_{SE} + \Gamma_{SD})t}), \tag{8.1}$$

where $\langle P_{Rb} \rangle$ refers to rubidium polarization, while the γ_{SE} and Γ_{SD} correspond to spin-exchange and spin-destruction rates, respectively. The results of single pulse NMR measurements monitoring the signal growth after the laser was switched on are shown Figure 8.7, and the build-up times determined by the fitting to single exponentials are given in Table 8.1.

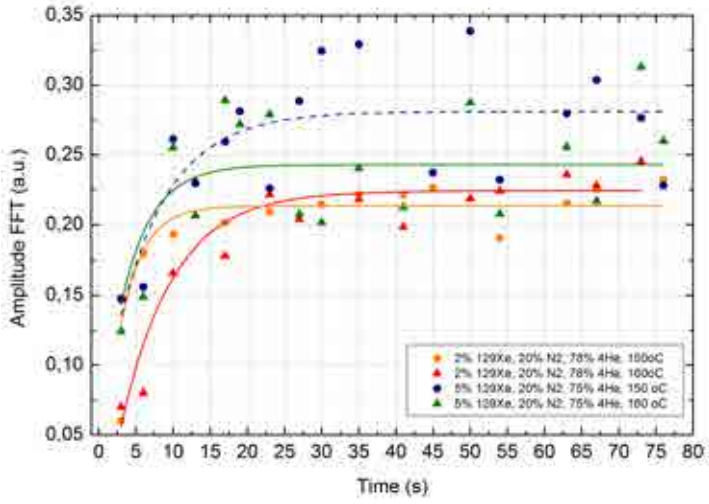

Figure 8.7: ^{129}Xe polarization build-up illustrated by the NMR signal at two different ^{129}Xe contents 2% (orange, red) and 5% (green, blue) and temperatures: 150°C (orange, blue) and 160°C (red, green).

9

Appendix B - Polarizing ^{3}He

Several pre-clinical and clinical studies suggest that compared to HP ^{129}Xe, HP ^{3}He is a superior contrast agent in MR investigations of human lung morphology. ^{3}He is an inert gas which quickly leaves the human body, and its application does not cause any side effects. On the other hand, apart from MRI, HP ^{129}Xe has found much wider application in materials science, chemistry and related disciplines, where its large chemical shift range is exploited in the NMR spectroscopy, as it was discussed in previous chapters.

^{3}He has 2.7 times larger gyromagnetic ratio than ^{129}Xe, which increases the sensitivity of MRI significantly. The main disadvantage of using HP ^{3}He in a routine clinical diagnostics is the shortage of its supply, due to dramatic increase of the demand in recent years [125]. Since the only source of ^{3}He is tritium decay, an efficient recycling of the gas is mandatory [126].

In this chapter, fundamental aspects of polarizing ^{3}He are described and the design of two polarizers and their implementation in MRI studies are presented [103, 128, 127]. My participation in this work started with my MSc, and continued during my PhD studies.

9.1 Theory of MEOP of ^{3}He

The possibility of polarizing ^{3}He by optical pumping has been known since 1963 [129]. Non-equilibrium hyperpolarization in ^{3}He can be obtained via metastability exchange optical pumping. In contrary to SEOP, the MEOP is performed without any other buffer gases and takes place among helium atoms themselves. The MEOP, schematically presented in Figure 9.1, is a three stage process and takes place at low magnetic field, which produces hyperfine splitting and also prevents the optically prepared orientation from fast relaxation.

In the first step, helium atoms are excited with radio frequency discharge. This way the 2^3S *metastable state* (as it is characterized by a long residence time) is populated due to electronic collisions occurring in the plasma. The density of metastable helium atoms is 3 to 5 orders of magnitude lower than the rubidium density in the SEOP experiments [130].

The optical pumping is performed in the second step, when metastable ^{3}He atoms absorb the circularly polarized laser light tuned to the 2^3S – 2^3P transition. The *hyperfine interaction* causes the transfer of electronic polarization to nuclear spins.

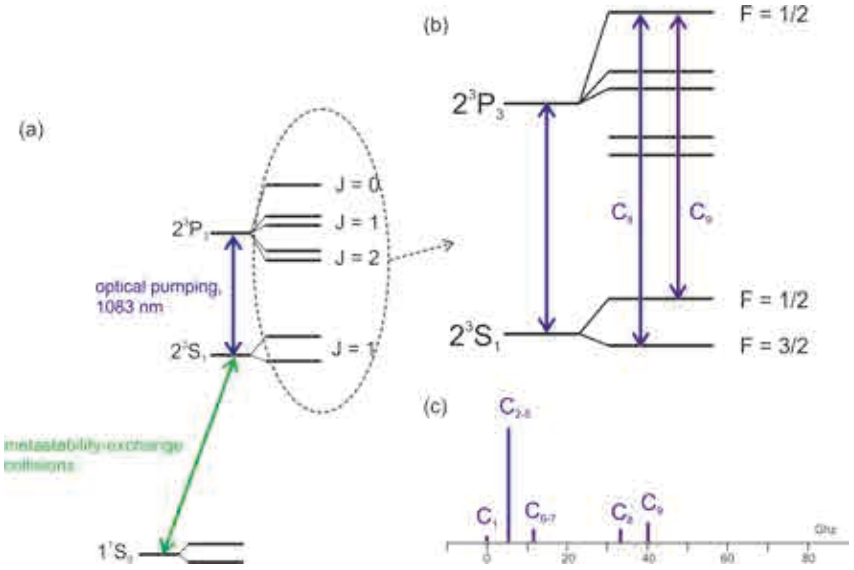

Figure 9.1: Energy levels diagrams for the MEOP process. (a) A weak radio frequency discharge promotes a small fraction of helium atoms into the excited metastable state 2^3S, where the optical pumping occurs by the circularly polarized laser light tuned to 1083 nm. Nuclear polarization is transferred to atoms in the ground state 1^1S_0 by metastability-exchange collisions. (b) Closer view of the $2^3S_1 \rightarrow 2^3P_3$ transitions, with the most efficient C_8 and C_9 pumping lines. (c) Simplified spectrum of ^{3}He at magnetic field below 10 mT with all C_n pumping lines for $n = 1 - 9$.

In the last step the nuclear polarization is transferred from metastable to ground state helium atoms by atomic collisions.

In contrary to SEOP, which is a relatively slow process taking place at atmospheric pressure, the standard MEOP is much faster, but operates at low pressure of about 1 mbar only. An increase of operating pressure causes a dramatic drop of achievable polarization. Therefore a mechanical compression is necessary in practical application, leading to additional relaxation. It has been recently found that performing the MEOP at high magnetic field, of the order of 1 T, it is possible to increase the operating pressure to several hundreds of mbars, without losing too much of polarization [131, 132, 133]. This method is called the MEOP in *non-standard conditions* and can be conveniently implemented in the clinical 1.5 T MRI scanner [127].

Systematic studies of the MEOP process at high magnetic fields (0.45, 0.9, 1.5, and 2 T) and elevated pressures (32 and 64 mbar) were performed [134]. The experimental parameters such as laser power, beam profile, and the shape of the optical pumping cell were optimized. The effect of rf discharge intensity on the plasma-induced nuclear relaxation was also studied, establishing the best conditions for maximum MEOP efficiency.

The structure of 2^3S and 2^3P energy levels is significantly changed at high magnetic field, imposing different conditions for the 1083 nm transition [135]. An elevated pressure modifies also the plasma distribution, which concentrates near the cell walls. In order to maximize the laser light absorption, a modified optical setup using axicons to reshape the

laser beam into a doughnut shape was successfully implemented [136].

A non-destructive measurement of ^{3}He polarization is possible with optical methods [137, 138], which is advantageous when compared to the NMR technique. In the *non-standard conditions* MEOP, a probe beam tuned to $2^3S_1 \rightarrow 2^3P_3$ transition is introduced. By monitoring the populations of two 2^3S sublevels, which do not take part in optical pumping, the absolute nuclear polarization of ^{3}He can be determined.

9.2 Polarizers and lung imaging with HP ^{3}He

^{3}He MEOP can be performed in two types of polarizers, the first operating at *standard conditions* and the second at *non-standard conditions*, which are shown on Figure 9.2.

The first one was built several years before [**?**], but during my PhD studies it was upgraded. The throughput was increased from 0.4 scc/min to 3 scc/min (scc - standard cubic centimeter), which made it possible to perform initial medical tests with HP ^{3}He.

An aluminum frame supports six quadratic coils generating a homogeneous magnetic field of 16.4 Gauss. The apparatus is mounted on the table placed inside. The Pyrex MEOP cell (5 cm diameter, 48 cm length) is located in the center. A new ytterbium-doped 10 W fiber laser (*Keopsys*) produces the beam, which is expanded by the Kepler-like telescope (magnification 7x, *Eksma Optics*). Then the beam passes through the polarizing beam splitter and is circularly polarized by the quarter-wave plate. The laser light propagates along the direction of applied magnetic field and is back reflected by a mirror to increase its absorption. The gas handling system which is connected to the cell, apart from supplying ^{3}He, can also provide ^{4}He for cleaning purposes. The outlet of the cell supplies the polarized helium gas to the peristaltic compressor (patent by P.-J. Nacher [139]), which increases its pressure from initial $\sim$1 mbar to about 200 mbars. Then it is accumulated in the 1.1 L Pyrex storage cell (wall relaxation time of 150 h). The final polarization in this unit was 30 %.

First imaging of the rat lungs were performed on the home-made 0.088 T MR system. The HP ^{3}He was prepared on-site, quickly transported to the scanner, and administered to the anesthetized animal. Since the rat lungs needed a small amount of polarized gas, the procedure resulted in obtaining quite satisfying images [140].

For the MR imaging of human lungs, about 300 ml of HP ^{3}He is required for a single patient, supplemented by N_2 or ^{4}He up to the atmospheric pressure. The polarized gas was prepared in the lab and transported to the clinic in a magnetically shielded transport box [141]. The imaging experiments were performed on the Siemens Sonata 1.5 T medical scanner, located in the John Paul II Hospital in Krakow [128]. The gas was transferred to a Tedlar bag using a smaller version of the peristaltic compressor. Under supervision of medical personnel, a healthy volunteer who was already put inside the scanner breathed the gas and the FLASH imaging sequence was applied. Although some polarization losses occurred during transportation, a satisfactory image was obtained, as shown on Figure 9.3a.

The performance of MRI with HP ^{3}He was dramatically improved, when a high-field polarizer operating in *non-standard conditions* inside the medical scanner was implemented. The polarization losses occurring during gas compression and transportation were eliminated.

The polarizer was mounted on a wooden table that fits inside the RF birdcage coil, which is dedicated for lung imaging using HP ^{3}He. The optical pumping takes place in three cylindrical cells connected in series and equipped with electrodes for producing RF discharge. The electrodes are driven by two home-made power amplifiers. The laser beam

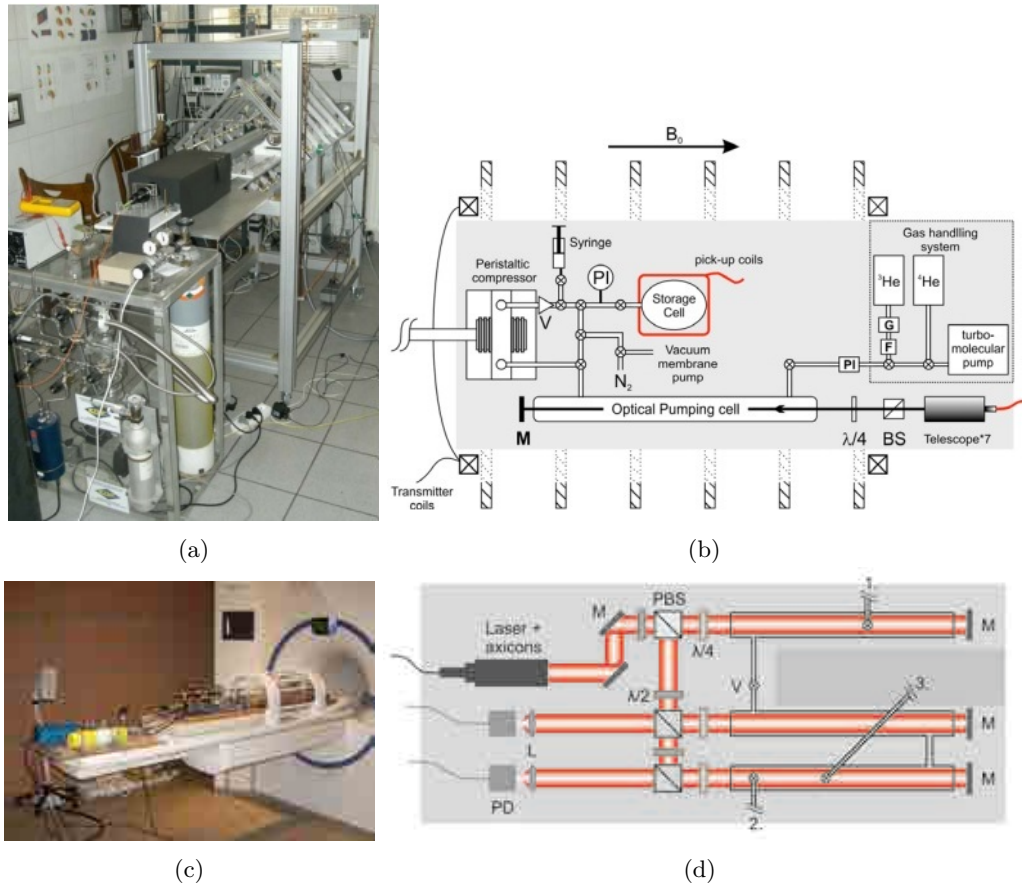

Figure 9.2: The ^{3}He MEOP polarizer operating at *standard conditions* (a) and its simplified scheme (b) (both adapted from [140]), and the ^{3}He MEOP polarizer operating at *non-standard conditions* inside medical scanner (adapted from [140]) (c) and its simplified scheme (d) (adapted from [127]). PI - presure meter, M - mirror, G - getter filter, F - filter, BS - beamsplitter cube, $\gamma/4$ - quarte-wave plate; PBS - polarizing beamsplitter cube, M - mirror, $\gamma/4$ - quarter-wave plate, $\gamma/2$ - half-wave plate, V - valve, 1 - the gas distribution system inlet, 2 - output for cleaning, 3 - inletto the accumulation cell.

(a) (b)

Figure 9.3: Images of healthy volunteer's lungs using a FLASH sequence with the HP ^{3}He obtained in the low-field (a) and high-field (P = 20.8 ± 1 %) (b) polarizers. Parameters: 20 cm slice thickness, 35 cm FOV, 64 × 64 matrix, flip angle: 11°, 16.64 kHz bandwidth, TE = 3.6 ms, TR = 7.5 ms (a); 20 cm slice thickness, 38 cm FOV, 128 × 128 matrix, flip angle: 8.6°, TE = 3.7 ms, TR = 7.9 ms, SNR = 56.3 (b).

is expanded by a Kepler-like telescope and formed into a doughnut shape with the pair of axicons. Then the beam is split into three parallel beams with a set of half-wave plates, mirrors and beam splitters which pass through the three OP cells. Each beam is circularly polarized with quarter-wave plates. The gas exiting the last cell is compressed by small peristaltic compressor driven by a non-magnetic pneumatic engine (*Globe Airmotors BV*), and accumulated in the storage cell. Both the compressor and storage cell are mounted on a separate table, which remains in the magnet after the main polarizer is removed, to make room for the patient. The gas distribution system consisting of ^{3}He and ^{4}He containers and the turbo molecular pump for cleaning are located in a separate room, far away from the scanner. The initial operating parameters of the high field polarizer were taken from the previous systematic studies that were carried out with the *sealed* OP cells. The optimum laser power, operating pressure, and the rf discharge intensity as a function of applied magnetic field were determined. The operating conditions for the continuous flow through the *open* cells had to be modified. The achievable polarization of about 40% was lower, as expected, mainly due to some impurities introduced to the cells by the gas flow. Still, a satisfactory image of the healthy volunteers lungs was obtained, as shown on Figure 9.3b. The same FLASH imaging sequence with slightly different parameters was used. Based on this result, systematic clinical studies with the cooperation of medical staff will be carried out, to prepare routine diagnostic protocols. These will be afterwards expanded to include the MRI technique using HP ^{129}Xe, which was the subject of my PhD studies.

Bibliography

[1] H.-U. Kauczor (Ed.), 2009 Springer-Verlag Berlin Heidelberg, ISBN 978-3-540-34618-0

[2] R. S . Virgincar, Z. I. Cleveland, S. S. Kaushik, M. S. Freeman, J. Nouls, G. P. Cofer, S. Martinez-Jimenez, M. He, M. Kraft, J. Wolber, H. Page McAdams, B. Driehuys, *Quantitative analysis of hyperpolarized ^{129}Xe ventilation imaging in healthy volunteers and subjects with chronic obstructive pulmonary disease*, NMR Biomedical 26, 424–435, 2013

[3] M. Batz, S.Baeßler, W. Heil, E.W. Otten, D. Rudersdorf, J. Schmiedeskamp, Y. Sobolev, M. Wolf, *^{3}He Spin Filter for Neutrons*, Journal of Research of the National Institute of Standards and Technology Volume 110, No. 3, 2005

[4] T. Ito and J. Fraissard, *^{129}Xe NMR study of xenon adsorbed on Y zeolites*, The Journal of Chemical Physics 76, 5225, 1982

[5] A. Kastler, *The optical production and the optical detection of an inequality of population of the levels of spatial quantization of atoms. application to the experiments of Stern and Gerlach and to magnetic resonance*, Journal de Physique et le Radium 11, 255–265, 1950

[6] J. Brossel, A. Kastler, J. Winters, *Optical method of creating an inequality of population between Zeeman sub-levels of atomic ground states*, Journal de Physique et le Radium 13:668–669, 1952

[7] W. Happer, *Optical Pumping*, Review of Modern Physics 44, 169–250, 1972

[8] B. M. Goodson, *Nuclear magnetic resonance of laser-polarized noble gases in molecules, materials, and organisms*, Journal of Magnetic Resonance 155, 157, 2002

[9] J. Wolber, A. Cherubini, A. S. K. Dzik-Jurasz, Martin O. Leach, A. Bifone, *Spin-lattice relaxation of laser-polarized xenon in human blood*, Proceedings of the National Academy of Sciences of the United States of America 96, 3664–3669, 1999

[10] Y. V. Chang, J. D. Quirk, I. C. Ruset, J. J. Atkinson, F. W. Hersman, J. C. Woods, *Quantification of human lung structure and physiology using hyperpolarized ^{129}Xe*, Magnetic Resonance in Medicine 71, 339–344, 2014

[11] A. Bifone, Y.-Q. Song, R. Seydoux, R. E. Taylor, B.M. Goodson, T. Pietraß, T. F. Budinger, G. Navon, A. Pines, Proceedings of the National Academy of Sciences of the United States of America 93, 12932–12936, 1996

[12] N. Abdeen1, A. Cross, G. Cron, S. White, T. Rand, D. Miller, G. Santyr, *Measurement of xenon diffusing capacity in the rat lung by hyperpolarized ^{129}Xe MRI and dynamic spectroscopy in a single breath-hold*, Magnetic Resonance in Medicine 56, 255–264, 2006

[13] B. Driehuys, H. E. Mller, Z. Cleveland, J. Pollaro, L. W. Hedlund, *Pulmonary perfusion and xenon gas exchange in rats: MR imaging with intravenous injection of hyperpolarized ^{129}Xe.*, Radiology 252, No. 2, 386–393, 2009

[14] N. Woodhouse, J. M. Wild, E. J.R. van Beek, N. Hoggard, N. Barker, Ch. J. Taylor, *Assessment of hyperpolarized ^{3}He lung MRI for regional evaluation of interventional therapy: A pilot study in pediatric cystic fibrosis*, Journal of Magnetic Resonance Imaging 30, Issue 5, 981–988, 2009

[15] B. Driehuys, S. Martinez-Jimenez, Z. Cleveland, G. M. Metz, D. M. Beaver, J. C. Nouls, S. S. Kaushik, R. Firszt, C. Willis, K. T. Kelly, J. Wolber, M. Kraft, H. P. McAdams, *Chronic obstructive pulmonary disease: safety and tolerability of hyperpolarized ^{129}Xe MR imaging in healthy volunteers and patients*, Radiology 262, No. 1, 279–289, 2012

[16] M. Kirby , S. Svenningsen , N. Kanhere , A. Owrangi , A. Wheatley , H. O. Coxson , G. E. Santyr , N. A. M. Paterson, D. G. McCormack ,G. Parraga, *Pulmonary ventilation visualized using hyperpolarized helium-3 and xenon-129 magnetic resonance imaging: differences in COPD and relationship to emphysema*, Journal of Applied Physiology Published 114, No. 6, 707–715 , 2013

[17] A. Kastler, *Optical methods for studying Hertzian resonances*, Nobel Lecture, December 12, 1966

[18] Y.-Y. Jau, N. N. Kuzma, W. Happer, *High-field measurement of the ^{129}Xe-Rb spin-exchange rate due to binary collisions*, Physical Review A 66, 052710, 2002

[19] Y. Y. Jau, N. N. Kuzma, W. Happer, *Magnetic decoupling of ^{129}Xe-Rb and ^{129}XXe-Cs binary spin exchange*, Physical Review A A 67, No. 2, 022720, 2003

[20] Ian A. Nelson, *Physics of Practical Spin-Exchange Optical Pumping*, Doctor of Philosophy dissertation, University of Wisconsin-Madison, 2001

[21] M. A. Bouchiat, J. Brossel, L. C. Pottier, *Evidence for Rb-rare-gas molecules from the relaxation of polarized Rb atoms in a rare gas. experimental results*, Journal of Chemical Physics 56, 3703, 1972

[22] W. Happer, E. Miron, S. Schaefer, D. Schreiber, W. A. van Wijngaarden, X. Zeng, *Polarization of the nuclear spins of noble-gas atoms by spin exchange with optically pumped alkali-metal atoms*, Physical Review A 29, No. 6, 3092, 1984

[23] M. A. Bouchiat, T. R. Carver, C. M. Varnum, *Nuclear Polarization in ^{3}He Gas Induced by Optical Pumping and Dipolar Exchange*, Physical Review Letters 5, No. 8, 373–375, 1960

[24] S. Appelt, A. Ben-Amar Baranga, C. J. Erickson, M. V. Romalis, A. R. Young, and W. Happer, *Theory of spin-exchange optical pumping of ^{3}He and ^{129}Xe*, Physical Review A 58, No. 2, 1412, 1998

[25] M. E. Wagshul, T. E. Chupp, *Optical pumping of high-density Rb with a broadband dye laser and GaAlAs diode laser arrays: Application to ^{3}He polarization*, Physical Review A 40, No. 8, 4447, 1989

[26] I. C. Ruset, S. Ketel, F. W. Hersman, *Optical Pumping System Design for Large Production of Hyperpolarized ^{129}Xe*, Physical Review Letters 96, 053002, 2006

[27] A. B. Baranga, S. Appelt, M. V. Romalis, C. J. Erickson, A. R. Young, G. D. Cates, W. Happer, *Polarization of ^{3}He by spin exchange with optically pumped Rb abd K vapors*, Physical Review Letters 80, No. 13, 2801–2804, 1998

[28] W. C. Chen, T. R. Gentile, T. G. Walker, E. Babcock, *Spin Exchange optical Pumping of ^3He with Rb-K mixtures and pure K*, Physical Review A 75, No. 1, 013416, 2007

[29] I. A. Nelson, T. G. Walker, *Rb-Xe spin relaxation in dilute Xe mixtures*, Physical Review A 65, No. 1, 012712, 2002

[30] G. D. Cates, S.R. Schaefer, W. Happer, *Relaxation of spins due to field inhomogeneities in gaseous samples at low magnetic fields and low pressures*, Physical Review A 37, No. 8, 2877, 1988

[31] G. D. Cates, D. J. White, T.-R. Chien, S. R. Schaefer, W. Happer, emphSpin relaxation in gases due to inhomogeneous static and oscillating magnetic fields, Physical Review A 38, No. 10, 5092, 1988

[32] E. R, Hunt and H. Y. Carr, *Nuclear Magnetic Resonance of Xe-129 in Natural Xenon*, Physical Review 130, 2302, 1963

[33] G. D. Cates, R. J. Fitzgerald, A. S. Barton, P. Bogorad, M. Gatzke, N. R. Newbury, and B. Saam, Physical Review 45, no. 7, 4631–4639, 1992

[34] G. Norquay, S. R. Parnell, X. Xu, J. Parra-Robles, and J. M. Wild, *Optimized production of hyperpolarized ^{129}Xe at 2 bars for in vivo lung magnetic resonance imaging*, Journal of Applied Physics 113, 044908, 2013

[35] Boyd M. Goodson, *Hyperpolarizing nuclear spins of noble gases via spin-exchange optical pumping - principles and practice for enhancing NMR and MRI*, presentation during COST Annual Meeting Spin Hyperpolarisation in NMR and MRI Z urich, Switzerland, June 27, 2014

[36] B. Driehuys, G. D. Cates, E. Miron, K. Sauer, D. K. Walter, W. Happer, *High-volume production of laser-polarized ^{129}Xe*, Applied Physics Letters 69, No. 12, 1668–1670, 1996

[37] C. V. Rice, D. Raftery, *Rubidium-Xenon Spin Exchange and Relaxation Rates Measured at High Pressure and High Magnetic Field*, Journal of Chemical Physics 117, No. 12, 5632–5641, 2002

[38] X. Zeng, Z. Wu, T. Call, E. Miron, D. Schreiber, W. Happer, *Experimental determination of the rate constants for spin exchange between optically pumped K, Rb, and Cs atoms and Xe129 nuclei in alkali-metalnoble-gas van der Waals molecules*, Physical Review A 31, No. 1, 260–278, 1985

[39] B. Driehuys, G. D. Cates, E. Miron, K. Sauer, D. K. Walter, W. Happer, *High volume production of laserpolarized ^{129}Xe*, Applied Physics Letters 69, 1668 (1996)

[40] T. Walker, W. Happer, *Spin-exchange optical pumping of noble-gas nuclei*, Reviews of Modern Physics 69, No. 2, 629–642, 1997

[41] E. Babcock, B. Chann, T. G. Walker, W. C. Chen, T. R. Gentile, *Limits to the Polarization for Spin-Exchange Optical Pumping of ^3He*, Physical Review Letters 96, 083003, 2006

[42] Thad G. Walker, *Fundamentals of Spin-Exchange Optical Pumping*, Journal of Physics: Conference Series 294, 012001, 2011

[43] E. Babcock, I. Nelson, S. Kadlecek, B. Driehuys, L. W. Anderson, F. W. Hersman, T. G. Walker, *Hybrid Spin-Exchange Optical Pumping of 3He*, Physical Review Letters 91, No. 12, 123003, 2003

[44] I. A. Nelson and T. G. Walker, *Rb-Xe spin relaxation in dilute Xe mixtures*, Physical Review A 65, 012712, 2001

[45] B. N. Berry-Pusey, B. C. Anger, G. Laicher, and B. Saam, *Nuclear spin relaxation of ^{129}Xe due to persistent xenon dimers*, Physical Review A 74, 063408, 2006

[46] B. C. Anger, G. Schrank, A. Schoeck, K. A. Butler, M. S. Solum, R. J. Pugmire, B. Saam, *Gas-phase spin relaxation of ^{129}Xe*, Physical Review A 78, 043406, 2008

[47] B. Chann, I. A. Nelson, L.W. Anderson, B. Driehuys, T. G. Walker, *^{129}Xe-Xe Molecular Spin Relaxation*, Physical Review Letters 88, No. 11, 113201, 2002

[48] J. Schmiedeskamp, W. Heil, E. W. Otten, R.K. Kremer, A. Simon, J. Zimmer, *Paramagnetic relaxation of spin polarized 3He at bare glass surfaces. Part I*, The European Physical Journal D 38, Issue 3, 427–438, 2006

[49] A. Deninger, W. Heil, E. W. Otten, M. Wolf, R.K.Kremer, A. Simon, *Paramagnetic relaxation of spin polarized 3He at coated glass walls. Part II*, The European Physical Journal D 38, Issue 3, 439–443, 2006

[50] J. Schmiedeskamp, H.-J.Elmers, W.Heil, E.W. Otten, Yu. Sobolev, W. Kilian, H.Rinneberg, T. Sander-Thommes, F.Seifert, J. Zimmer, *Relaxation of spin polarized 3He by magnetized ferromagnetic contaminants. Part III*, The European Physical Journal D 38, Issue 3, 445–454, 2006

[51] J. O. Hirschfelder, C. F. Curtiss, R. B. Bird, *Molecular Theory of Gases and Liquids*, John Wiley and Sons, Inc., 1968

[52] I. L. Moudrakovski, S. R. Breeze, B. Simard, C. I. Ratcliffe, J. A. Ripmeester, T. Seideman, J. S. Tse *Gas-phase nuclear magnetic relaxation in 129Xe revisited*, The Journal of Chemical Physics 114, 2173, 2001

[53] G. D. Cates, S.R. Schaefer, W. Happer, *Relaxation of spins due to field inhomogeneities in gaseous samples at low magnetic fields and low pressures*, Physical Review A 37, No. 8, 1988

[54] C. J. Jameson, A. K. Jameson, J. K. Hwang, *Nuclear spin relaxation by intermolecular magnetic dipole coupling in the gas phase. ^{129}Xe in oxygen*, The Journal of Chemical Physics 89, 4074–4081, 1988

[55] Steven R. Breeze, Stephen Lang, Igor Moudrakovski, Chris I. Ratcliffe, John A. Ripmeester, Benoit Simard, Giles Santyr, *Coatings for optical pumping cells and extending the lifetime of hyperpolarized xenon*, Journal of Applied Physics 86, 4040-4042, 1999

[56] M. Repetto, E. Babcock, P. Blumler, W. Heil, S. Karpuk, K. Tullney, *Systematic T_1 improvement for hyperpolarized 129 xenon*, Journal of Magnetic Resonance 252, 163–169, 2015

[57] R. J. Fitzgerald, M. Gatzke, D. C. Fox, G. D. Cates, W. Happer, *^{129}Xe spin relaxation in frozen xenon*, Physical Review B 59, No. 13, 1999

[58] S. Lang, Igor L. Moudrakovski, Ch. I. Ratcliffe, J. A. Ripmeester, *Increasing the spin-lattice relaxation time of hyperpolarized xenon ice at 4.2 K*, Applied Physics Letters 80, No. 5, 2002

[59] G. D. Cates Jr, B. Driehuys, W. Happer, W. Miron, B. Saam, *Cryogenic Accumulation for spin-poalrized xenon-129*, United States Patent 5809801, 1998

[60] D. R. Lide (editor), *CRC Handbook of Chemistry and Physics*, CRC Press, 1990

[61] M. Gatzke, G.D. Cates, B. Driehuys, D. Fox, W. Happer, B. Saam, *Extraordinarily Slow Nuclear Spin Relaxation in Frozen Laser-Polarized ^{129}Xe*, Physical Review Letters 70, No. 5, 1993

[62] N. N. Kuzma, B. Patton, K. Raman, and W. Happer, *Fast Nuclear Spin Relaxation in Hyperpolarized Solid ^{129}Xe*, Physical Review Letters 88, No. 14, 147602, 2002

[63] W. W. Warren Jr, R. E. Norberg, *Nuclear Quadrupole Relaxation and Chemical Shift of Xe131 in Liquid and Solid Xenon*, Physical Review E 148, No. 1, 402, 1966

[64] N. N. Kuzma, D. Babich, W. Happer, *Anisotropic nuclear spin relaxation in single-crystal xenon*, Physical Review B 65, 134301, 2002

[65] P. R. Granfors, A. T. Macrander, R. O. Simmons, *Crystalline xenon: Lattice parameters, thermal expansion, thermal vacancies, and equation of state*, Physical Review B 24, No. 8, 4753, 1981

[66] H. C. Torrey, *Chemical Shift and Relaxation of Xe^{129} in Xenon Gas*, Physical Reviev 130, 6, 2306, 1963

[67] I. Oppenheim, M. Bloom, H. C. Torrey, *Nuclear Spin Relaxation In Gases And Liquids*, Canadian Journal of Physics. Volume 42, 70, 1964

[68] G. D. Cates, D. R. Benton, M. Gatzke, W. Happer, K. C. Hasson, N. R. Newbury, *Laser Production of Large Nuclear-Spin Polarization in Frozen Xenon*, Physical Review Letters 65, 2591, 1990

[69] T. Chupp, S. Swanson, *Medical imaging with laser polarized noble gases*, Advances In Atomic, Molecular, and Optical Physics 45, 41–101, 2001

[70] Wenjin Shao, Guodong Wang, Emlyn W. Hughes, *Measurement of spin-exchange rate constants between^{129}Xe and alkali metala*, Physical Review A 72, 022713, 2005

[71] Daniel A. Steck, *Rubidium 85 D Line Data*, available online at http://steck.us/alkalidata, revision 2.1.6, 20 September 2013

[72] Daniel A. Steck, *Rubidium 87 D Line Data*, available online at http://steck.us/alkalidata, revision 2.1.4, 23 December 2010

[73] Matthew P. Augustine and Kurt W. Zilm, *Optical pumping magnetic resonance in high magnetic fields: Characterization of nuclear relaxation during pumping*, Journal of Chemical Physics 105, No. 8, 2998–3011, 1996

[74] T. Pietraß, H.C. Gaede, *Optically Polarized Xe-129 In NMR-Spectroscopy*, Advanced Materials 7, Issue 10, 826, 1995

[75] L. C. de MenorVal, D. Raftery, S. - B. Liu, K. Takegoshi, R. Ryoo, A. Pines, *Investigations of Adsorbed Organic Molecules in Na-Y Zeolite by Xenon-129 NMR*, Journal of Chemical Physics 94, 27-31, 1990

[76] V.- V. Telkki, J. Lounila, J. Jokisaari, *Behavior of Acetonitrile Confined to Mesoporous Silica Gels As Studied by 129Xe NMR: A Novel Method for Determining the Pore Sizes*, The Journal of Physical Chemistry, 109, 757-763, 2005

[77] A. Mitchel, G. D. Cates, B. Driehuys, W. Happer, B. Saam, C. S. Springer, A. Wishnia, *Biological magnetic resonance imaging using hyperpolarized ^{129}Xe*, Nature 370, 199, 1994

[78] E. Brun, J. Oeser, H. H. Staub, C. G. Telschow, *The Nuclear Magnetic Moments of Xe129 and Xe131*, Physical Review 93, 904, 1954

[79] K. F. Stupic, Z. I. Cleveland, G. E. Pavlovskaya, T. Meersmann, *Hyperpolarized ^{131}Xe NMR spectroscopy*, Journal of Magnetic Resonance 208, 58–69, 2011

[80] J. Fukutomi, E. Suzuki, T. Shimizu, A. Kimura, and H. Fujiwara, *Analysis of the effect of foregin gases in the production of hyperpolarized ^{129}Xe gas on a simple system working under atmospheric pressure*, Journal of Magnetic Resonance 160, 26–32, 2003

[81] M. A. Rosenberry, J. P. Reyes, D. Tupa, T. J. Gay, *Radiation trapping in rubidium optical pumping at low buffer-gas pressures*, Physical Review A 75, 023401, 2007

[82] N. D. Bhaskar, W. Happer, M. Larsson, X. Zeng, *Slowing Down of Rubidium-Induced Nuclear Spin Relaxation of ^{129}Xe Gas in a Magnetic Field*, Physical Review Letters 50, No. 2, 105 – 108, 1983

[83] N. Tsopelas, N.J. Siakavellas, *Performance of circular and square coils in electromagneticthermal non-destructive inspection*, NDT&E International 40, 12–28, 2007

[84] B. Chann, I. Nelson, and T. G. Walker, *Frequency-narrowed external-cavity diode-laser-array bar*, Optics Letters 25, No. 18, 1352, 2000

[85] H. Zhu, I. C. Ruset, F. W. Hersman, *Spectrally narrowed external-cavity high-power stack of laser diode arrays*, Optics Letters 30, No. 11, 1342–1344, 2005

[86] P. Nikolaou, N. Whiting, N. A. Eschmann, K. E. Chaffee, B. M. Goodson, M. J. Barlow, *Generation of laser-polarized xenon using fiber-coupled laser-diode arrays narrowed with integrated volume holographic gratings*, Journal of Magnetic Resonance 197, 249–254, 2009

[87] N. Whiting, P. Nikolaou, N.A. Eschmann, M.J. Barlow, R. Lammert, J. Ungar , W. Hu, L. Vaissie, B.M. Goodson, *Using frequency-narrowed, tunable laser diode arrays with integrated volume holographic gratings for spin-exchange optical pumping at high resonant fluxes and xenon densities*, Applied Physic B 106, 775–788, 2012

[88] N. Whiting, P. Nikolaou, N. Eschmann, M. Barlow, B.M. Goodson, *Interdependence of in-cell xenon density and temperature during Rb/^{129}Xe spin-exchange optical pumping using VHG-narrowed laser diode arrays*, Journal of Magnetic Resonance 208, 298, 2011

[89] Z. Yang, H. Wang, Y. Li, Q. Lu, W. Hua, X. Xu, J. Chen, *A smile insensitive method for spectral linewidth narrowing on high power laser diode arrays*, Optics Communications 284, Issue 21, 5189–5191, 2011

[90] A. Gourevitch, G. Venus, V. Smirnov, D. A. Hostutler, L. Glebov, *Continuous wave, 30 W laser-diode bar with 10 GHz linewidth for Rb laser pumping*, Optics Letters 33, No. 7, 702–704, 2008

[91] C. Moser, G. Steckman, Photonics Spectra 39 , 82, 2005

[92] B. L. Volodin, S. V. Dolgy, E. D. Melnik, E. Downs, J. Shaw, V. S. Ban, *Wavelength stabilization and spectrum narrowing of high-power multimode laser diodes and arrays by use of volume Bragg gratings*, Optics Letters 29, 1891–1893, 2004

[93] B. Chann, E. Babcock, L. W. Anderson, T. G. Walker, *Skew light propagation in optically thick optical pumping cells*, Physical Review A 66, 033406, 2002

[94] J. Mispelter, M. Lupu, A. Briquet, *NMR Probeheads: For Biophysical and Biomedical Experiments*, Imperial College, ISBN-10: 1860946372, ISBN-13: 978-1860946370, 1st edition, 2006,

[95] P. Nikolaou, A. M. Coffey, M. J. Barlow, M. S. Rosen, B. M. Goodson, E. Y. Chekmenev, *Temperature-Ramped ^{129}Xe Spin-Exchange Optical Pumping*, Analytical Chemistry 86, Vo. 16, 8206 – 8212, 2014

[96] G. Schrank, Z. Ma, A. Schoeck, B. Saam, *Characterization of a low-pressure high-capacity ^{129}Xe flow-through polarizer*, Physical Review A 80, 063424, 2009

[97] T. J. Killian, *Thermionic phenomena caused by vapors of rubidium and potassium*, Physical Review 27, 578, 1926

[98] S.Patz, F. W. Hersman, I. Muradian, M. I. Hrovat, I. C. Ruset, S. Ketel, F.Jacobson, G. P. Topulos, H. Hatabu, J. P. Butler, *Hyperpolarized ^{129}Xe MRI: A Viable Functional Lung Imaging Modality?*, European Journal of Radiology 64, No. 3, 335–344, 2007

[99] A. L. Zook, B. B. Adhyaru, C. R. Bowers, *High capacity production of $< 65\%$ spin polarized xenon-129 for NMR spectroscopy and imaging* , Journal of Magnetic Resonance 159, 175–182, 2002

[100] P. Nikolaou, A. M. Coffey, L. L. Walkup, B. M. Gust, N. Whiting, H. Newton, I. Muradyan, M. Dabaghyan, K. Ranta, G. D. Moroz, M. S. Rosen, S. Patz, M. J. Barlow, E. Y. Chekmenev, B. M. Goodson, *XeNA: An automated open-source 129Xe hyperpolarizer for clinical use*, Magnetic Resonance Imaging 32, 541–550, 2014

[101] S. R. Parnell, M. H. Deppe, J. Parra-Robles, J. M. Wild, *Enhancement of ^{129}Xe polarization by off-resonant spin exchange optical pumping*, Journal of Applied Physics 108, 064908, 2010

[102] M. S. Freeman, K. Emami, B. Driehuys, *Characterizing and modeling the efficiency limits in large-scale production of hyperpolarized ^{129}Xe*, Physical Review A 90, 023406, 2014

[103] G. Collier, T. Pałasz, A. Wojna, B. Gowacz, M. Suchanek, Z. Olejniczak, T. Dohnalik, *A high-field ^{3}He metastability exchange optical pumping polarizer operating in a 1.5 T medical scanner for lung magnetic resonance imaging*, Journal of Applied Physics 113, Issue 20, 204905, 2013

[104] G. P. Wong, C. H. Tseng, V. R. Pomeroy, R. W. Mair, D. P. Hinton, D. Hoffmann, R. E. Stoner, F. W. Hersman, D. G. Cory, R. L. Walsworth, *A system for low field imaging of laser-polarized noble gas*, Journal of Magnetic Resonance 141, 217–227, 1999

[105] S. Patz, I. Muradian, M. I. Hrovat, I. C. Ruset, G. Topulos, S. D. Covrig, E. Frederick, H. Hatabu, F. W. Hersman, J. P. Butler, *Human Pulmonary Imaging and Spectroscopy with Hyperpolarized ^{129}Xe at 0.2T*, Academic Radiology 15, No. 6, 713–727, 2008

[106] J. C. Sharp, D. Yin, R. H. Bernhard, Q. Deng, A. E. Procca, T. L. Tyson, K. Lo., B. Tomanek, *The integration of real and virtual magnetic resonance imaging experiments in a single instrument*, Review of Scientific Instrumentsn 80, Issue 9, 093709, 2009

[107] B. Blasiak, V. Volotovskyy, Ch. Deng, T. Foniok, B. Tomanek, *A comparison of MR imaging of a mouse model of glioma at 0.2 T and 9.4 T*, Journal of Neuroscience Methods 204, 118–123, 2012

[108] F. Roméo, D. I. Hoult, *Magnet field profiling: analysis and correcting coil design*, Magnetic Resonance in Medicine 1, No, 1, 44–65, 1984

[109] K. Suchanek, K. Cieslar, Z. Olejniczak, T. Palasz, M. Suchanek, T. Dohnalik, *Hyperpolarized ^{3}He gas production by metastability exchange optical pumping for magnetic resonance imaging*, Optica Applicata 25, No. 2, 263–276, 2005

[110] M. Suchanek, *Tomograf magnetycznego rezonansu jdrowego do obrazowania z uyciem hiperspolaryzowanego ^{3}He*, PhD Thesis, Jagiellonian University, 2005

[111] K. Suchanek, *Zastosowanie ^{3}He spolaryzowanego metod pompowania optycznego z wymian metastabilnoci do tomografii magnetycznego rezonansu*, PhD Thesis, Jagiellonian University, 2005

[112] K. Cieslar, *Methodology for fast functional magnetic resonance imaging of the lungs using hyperpolarized ^{3}He*, PhD Thesis, Jagiellonian University, 2006

[113] M. W. Garrett, *Axially Symmetric Systems for Generating and Measuring Magnetic Fields*, Journal of Applied Physics 22, 1091, 1951

[114] H. U. Kauczor, D. Hofmann, K. F. Kreitner , H. Nilgens, R. Surkau, W. Weil, A. Potthast, M. V. Knopp, E. W. Otten, M. Thelen, *Normal and abnormal pulmonary ventilation: visualization at hyperpolarized He-3 MR imaging.*, Radiology 201, No. 2, 564–568, 1996

[115] R. Aysola, E. E. de Lange, M. Castro, T. A. Altes, *Demonstration of the Heterogeneous Distribution of Asthma in the Lungs Using CT and Hyperpolarized Helium-3 MRI*, Journal of Magnetic Resonance Imaging 32, 1379–1387, 2010

[116] A. J. Swift, J. M. Wild, S. Fichele, N. Woodhouse, S. Fleming, J. Waterhouse, R. A. Lawson, M. N.J. Paley, E. J.R. Van Beek, [**?**], European Journal of Radiology 54, 352–358, 2005

[117] L. F. Donnelly, J. R. MacFall, H. P. McAdams, J. M. Majura, J. Smith, D. P. Frush, P. Bogonad, H. C. Charles, C. E. Ravin, *Cystic fibrosis: combined hyperpolarized ^{3}He-enhanced and conventional proton MR imaging in the lung–preliminary observations*, Radiology 212, No. 3, 885–889, 1999

[118] S. S. Kaushik, Z. I. Cleveland, G. P. Cofer, G. Metz, D. Beaver, J. Nouls, M. Kraft, W. Auffermann, J. Wolber, H. P. McAdams, B. Driehuys, *Diffusion-Weighted Hyperpolarized ^{129}Xe MRI in Healthy Volunteers and Subjects With Chronic Obstructive Pulmonary Disease*, Magnetic Resonance in Medicine 65, 1155–1165, 2011

[119] B. Saam, D. Yablonskiy V. Kodibagkar J. Leawoods J, D. Gierada, J. Cooper, S. Lefrak, M. Conradi, *MR imaging of diffusion of ^{3}He gas in healthy and diseased lungs*, Magn Reson Med 44: 174-179 (2000)

[120] J. M. Wild, H. Marshall, M. Bock, L. R. Schad, P. M. Jakob, M. Puderbach, F. Molinari, E. J. R. Van Beek, J. Biederer, *MRI of the lung (1/3): method*, Insights Imaging 3, 345– 353, 2012

[121] L. Schr:oder, T. J. Lowery, Ch. Hilty, D. E. Wemmer, A. Pines, *Molecular Imaging Using a Targeted Magnetic Resonance Hyperpolarized Biosensor*, Science 314, No. 5798, 446–449, 2006

[122] M. Luhmer, B. M. Goodson, Y.- Q. Song, D. D. Laws, L. Kaiser, M. C. Cyrier, A. Pines, *Study of Xenon Binding in Cryptophane-A Using Laser-Induced NMR Polarization Enhancement*, The Journal of the American Chemical Society 121, No. 24, 3502-3512, 1998

[123] T. K. Stevens, R. M. Ramirez, A. Pines, *Nanoemulsion Contrast Agents with Sub-picomolar Sensitivity for Xenon NMR*, The Journal of the American Chemical Society 135, No. 26, 9576–9579, 2013

[124] H. A. Fogarty, P. Berthault, T. Brotin, G. Huber, H. Desvaux, J.-P. Dutasta, *A Cryptophane Core Optimized for Xenon Encapsulation*, The Journal of the American Chemical Society 129, 10332–10333, 2007

[125] A. Cho., *Helium-3 Shortage Could Put Freeze On Low-Temperature Research*, Science 326, No. 5954, 778–779, 2009

[126] Z. Salhi, T. Großmann, M. Gueldner, W. Heil, S. Karpuk, E. W. Otten, D. Rudersdorf, R. Surkau, U. Wolf, *Recycling of ^{3}He From Lung Magnetic Resonance Imaging*, Magnetic Resonance in Medicine 67, 1758–1763, 2012

[127] T. Dohnalik, B. Glowacz, Z. Olejniczak, T. Pałasz, M. Suchanek, A. Wojna, *Spectroscopic issues in optical polarization of ^{3}He gas for Magnetic Resonance Imaging of human lungs*, European Physical Journal Special Topics 222, 2103–2118, 2013

[128] G. Collier, M. Suchanek, A. Wojna, K. Cieslar, T. Palasz, B. Glowacz, Z. Olejniczak., T. Dohnalik, *Metastability exchange optical pumping low field polarizer for lung magnetic resonance imaging*, Optica Applicata 42, Issue 1, 223–239, 2012

[129] F. D. Colegrove, L. D. Schearer, and G. K. Walters, *Polarization of ^{3}He Gas by Optical Pumping*, Physical Review 132, 2561, 1963

[130] H.-U. Kauczor, R. Surkau, T. Roberts, *MRI using hyperpolarized noble gases*, European Radiology 8, 820–827, 1998

[131] P.-J. Nacher, E. Courtade, M. Abboud, A. Sinatra, G Tastevin, T. Dohnalik , *Optical pumping of helium-3 at high pressure and magnetic field*, Communication dans un congrs, 2225 – 2236, 2002

[132] E. Courtade, *Pompage optique de l'helium dans des conditions non-standard* , PhD Thesis, Paris, 2001

[133] M. Abboud, A. Sinatra, X. Maitre, G. Tastevin, P.-J. Nacher, *High nuclear polarization of helium-3 at low and high pressure by metastability exchange optical pumping at 1.5 Tesla*, Europhysics letters - EPL, Association europenne de physique, 68, 480, 2004

[134] A. Nikiel, T. Palasz, M. Suchanek, M. Abboud, A. Sinatra, Z. Olejniczak, T. Dohnalik, G. Tastevin, P.-J. Nacher., *Metastability exchange optical pumping ^{3}He at high pressure and high magnetic field for medical application*, European Physical Journal Special Topics 144, 255, 2007

[135] A. Nikiel, *Polaryzacja ^{3}He w warunkach rozprzezenia struktury nadsubtelnej*, PhD Thesis, Jagiellonian University, 2010

[136] T. Dohnalik, A. Nikiel, T. Palasz, M. Suchanek, G. Collier, M. Grenczuk, B. Gowacz, Z. Olejniczak, *Optimization of the pumping laser beam spatial profile in the MEOP experiment performed at elevated ^{3}He pressures*, European Physical Journal Applied Physics 54, 20802, 2011

[137] K. Suchanek, M. Suchanek, A. Nikiel, T. Palasz, M. Abbound, A. Sinatra, P.-J. Nacher, G. Tastevin, *Optical measurement of absolute polarization of ^{3}He gas in a wide range of magnetic field and pressure*, European Physical Journal Special Topics 144, 67, 2007

[138] C. Talbot, M. Batz, P.- J. Nacher, G. Tastevin, *An accurate optical technique for measuring the nuclear polarisation of ^{3}He gas*, Journal of Physics: Conference Series 294, 012008, 2011

[139] P. - J. Nacher, *Peristaltic compressors suitable for relaxation-free compression of polarized gas*, United State patent n°US6655931B2, 2003

[140] G. Collier, *Metastability Exchange Optical Pumping (MEOP) of ^{3}He in situ*, PhD Thesis, Jagiellonian University, 2011

[141] F. Thien, M. Friese, G. Cowin, D. Maillet, D. Wang, G. Galloway, I. Brereton, P. J. Robinson, W. Heil, B. Thompson, *Feasibility of functional magnetic resonance lung imaging in Australia with long distance transport of hyperpolarized helium from Germany*, Respirology 13, 599–602, 2008